

Computer simulations of soft particles in flow

Inaugural-Dissertation

zur

Erlangung des Doktorgrades

der Mathematisch-Naturwissenschaftlichen Fakultät

der Universität zu Köln

vorgelegt von

Dinar Katanov

aus Durtuly, Russland

Jülich

2016

Berichterstatter: **Prof. Dr. Gerhard Gompper**
(Gutachter) **Prof. Dr. Michael Lässig**

Tag der mündlichen Prüfung: 15.04.2016

Abstract

Understanding the dynamics of blood cells is a crucial element to discover biological mechanisms, to develop new efficient drugs, design sophisticated microfluidic devices, for diagnostics. In this work, we focus on the dynamics of red blood cells in microvascular flow.

Microvascular blood flow resistance has a strong impact on cardiovascular function and tissue perfusion. The flow resistance in microcirculation is governed by flow behavior of blood through a complex network of vessels, where the distribution of red blood cells across vessel cross-sections may be significantly distorted at vessel bifurcations and junctions.

We investigate the development of blood flow and its resistance starting from a dispersed configuration of red blood cells in simulations for different hematocrits, flow rates, vessel diameters, and aggregation interactions between red blood cells. Initially dispersed red blood cells migrate toward the vessel center leading to the formation of a cell-free layer near the wall and to a decrease of the flow resistance. The development of cell-free layer appears to be nearly universal when scaled with a characteristic shear rate of the flow, which allows an estimation of the length of a vessel required for full flow development, $l_c \approx 25D$, with vessel diameter D . Thus, the potential effect of red blood cell dispersion at vessel bifurcations and junctions on the flow resistance may be significant in vessels which are shorter or comparable to the length l_c .

The presence of aggregation interactions between red blood cells lead in general to a reduction of blood flow resistance. The development of the cell-free layer thickness looks similar for both cases with and without aggregation interactions. Although, attractive interactions result in a larger cell-free layer plateau values. However, because the aggregation forces are short-ranged at high enough shear rates ($\bar{\gamma} \gtrsim 50 \text{ s}^{-1}$) aggregation of red blood cells does not bring a significant change to the blood flow properties.

Also, we develop a simple theoretical model which is able to describe the converged cell-free-layer thickness with respect to flow rate assuming steady-state flow. The model is based on the balance between a lift force on red blood cells due to cell-wall hydrodynamic interactions and shear-induced effective pressure due to cell-cell interactions in flow. We expect that these results can also be used to better understand the flow behavior of other suspensions of deformable particles such as vesicles, capsules, and cells.

Finally, we investigate segregation phenomena in blood as a two-component suspension under Poiseuille flow, consisting of red blood cells and target cells. The spatial distribution of particles in blood flow is very important. For example, in case of nanoparticle drug delivery, the particles need to come closer to microvessel walls, in order to adhere and bring the drug to a target position within the microvasculature. Here we consider that segregation can be described as a competition between shear-induced diffusion and the lift force that pushes every soft particle in a flow away from the wall. In order to investigate the segregation, on one hand, we have 2D DPD simulations of red blood cells and target cell of different sizes, on the other hand the Fokker-Planck equation for steady state. For the equation we measure force profile, particle distribution and diffusion constant across the channel. We compare simulation results with those from the Fokker-Planck equation and find a very good correspondence between the two approaches. Moreover, we investigate the diffusion behavior of target particles for different hematocrit values and shear rates. Our simulation results indicate that diffusion constant increases with increasing hematocrit and depends linearly on shear rate.

The third part of the study describes development of a simulation model of complex vascular geometries. The development of the model is important to reproduce vascular systems of small pieces of tissues which might be gotten from MRI or microscope images.

The simulation model of the complex vascular systems might be divided into three parts: modeling the geometry, developing in- and outflow boundary conditions, and simulation domain decomposition for an efficient computation.

We have found that for the in- and outflow boundary conditions it is better to use the SDPD fluid than DPD one because of the density fluctuations along the channel of the latter. During the flow in a straight channel, it is difficult to

control the density of the DPD fluid. However, the SDPD fluid has not that shortcoming even in more complex channels with many branches and in- and outflows because the force acting on particles is calculated also depending on the local density of the fluid.

Kurzzusammenfassung

Die Dynamik der Bewegung von Zellen im Blut zu verstehen ist ein wesentlicher Schritt auf dem Weg zu neuen Wirkstoffen, zu einer besseren Diagnostik von Krankheiten und hat Anwendung im Bereich der Mikrofluidik. Das Hauptaugenmerk in dieser Arbeit liegt dabei auf der Dynamik der roten Blutkörperchen in mikrovaskulärem Fluss.

Der mikrovaskuläre Strömungswiderstand hat einen ausgeprägten Einfluss auf die Funktionalität des kardiovaskulären Systems und die Durchblutung des Gewebes. Dieser Strömungswiderstand in der Mikrozirkulation wird durch das Fließverhalten des Blutes durch ein komplexes Adernetzwerk bestimmt. Dabei kann sich die Verteilung roter Blutkörperchen entlang des Querschnitts einer Ader an Gabelungen und Kreuzungen wesentlich ändern.

In dieser Arbeit untersuchen wir die Entwicklung von Blutfluss und des zugehörigen Strömungswiderstands in Simulationen von Dispersionen roter Blutkörperchen in Abhängigkeit von unterschiedlichen Parametern wie Hämatokrit, Flussrate, Aderdurchmesser und Aggregationswechselwirkung zwischen roten Blutkörperchen. Die anfänglich gleichverteilte Dispersion roter Blutkörperchen bewegt sich zum Zentrum der Ader hin, wodurch sich eine Zell-freie Schicht an der Aderwand bildet und der Strömungswiderstand abnimmt. Die Entwicklung dieser Zell-freien Schicht scheint fast universell zu sein, wenn sie mit der charakteristischen Scherrate des Flusses skaliert wird. Dies erlaubt, die für eine vollständige Entwicklung des Flusses notwendige Aderlänge abzuschätzen, zu $l_c \approx 25D$, mit D dem Aderdurchmesser. In Adern, deren Länge in der gleichen Größenordnung wie l_c oder darunter liegt, kann daher der Strömungswiderstand an Gabelungen und Kreuzungen durch Ansammlungen roter Blutkörperchen stark beeinflusst werden.

Üblicherweise führen Aggregationswechselwirkungen zwischen roten Blutkörperchen zu einer Abschwächung des Strömungswiderstands. Die Entstehung der

Zell-freien Schicht ist sowohl mit als auch ohne Verwendung von Aggregationswechselwirkungen ähnlich. Attraktive Wechselwirkungen führen allerdings zu einer Verbreiterung der Zell-freien Schicht. Da die Aggregationswechselwirkungen jedoch kurzreichweitig sind ist der Einfluss auf die Strömungseigenschaften des Bluts bei ausreichend hohen Scherraten ($\bar{\dot{\gamma}} \gtrsim 50 \text{ s}^{-1}$) gering.

Weiterhin wurde im Rahmen dieser Arbeit ein simples theoretisches Modell entwickelt, das sich bei in konvergiertem, konstantem Fluss zur Beschreibung der Schichtdicke der Zell-freien Schicht in Abhängigkeit von der Fließgeschwindigkeit eignet. Dem Modell liegt ein Kräftegleichgewicht zwischen einer durch hydrodynamische Zell-Wand-Wechselwirkungen resultierenden Auftriebskraft auf die roten Blutkörperchen und eines durch den Scherfluss resultierenden effektiven Drucks aufgrund der Zell-Zell-Wechselwirkungen im Fluss zu Grunde. Die hieraus erhaltenen Ergebnisse können auf Suspensionen anderer deformierbarer Partikel wie Vesikeln, Kapseln und Zellen übertragen werden und auch für diese zum besseren Verständnis beitragen.

Abschließend wurden Entmischungsphänomene in Blut, beschrieben als Zwei-Komponenten-Mischung von roten Blutkörperchen und anderen Zellen in Poiseuille-Fluss, untersucht. Die räumliche Verteilung von roten Blutkörperchen ist von besonderem Interesse. So müssen zum Beispiel in der Wirkstoffabgabe von Nanopartikeln die Nanopartikel so nah wie möglich an die Aderwände kommen, um dort anzuhafte und den Wirkstoff abzugeben. Wir nehmen hier an, dass Entmischung beschrieben werden kann als Wettbewerb zwischen Scherfluss-induzierter Diffusion und der Auftriebskraft, die weiche Partikel innerhalb eines Flusses von der Wand wegdrückt. Zur Untersuchung der Entmischungsphänomene wurden sowohl 2D DPD Simulationen von roten Blutkörperchen und Zellen verschiedener Größen durchgeführt als auch die Fokker-Planck-Gleichung zur Beschreibung des *steady state* verwendet. Für letzteren Ansatz wurden die Kräfteverteilung, die Partikelverteilung und die Diffusionskonstante entlang des Kanals gemessen. Die Ergebnisse der beiden Ansätze wurden vergleichend gegenüber gestellt und zeigten weitreichende Übereinstimmungen. Weiterhin untersuchten wir das Diffusionsverhalten von Zellen für verschiedene Hämatokritwerte und Scherraten. Unsere Simulationsergebnisse zeigen, dass die Diffusionskonstante mit steigendem Hämatokritwert ansteigt und linear von der Scherrate abhängt.

Im dritten Teil dieser Arbeit wurde eine Simulationemethode zur Untersuchung komplexer vaskulärer Geometrien entwickelt. Diese Methode findet in der Reproduktion kleiner Gewebereinheiten Anwendung, die aus MRI oder Mikroskopie stammenden Bildern erhalten werden.

Die wesentlichen drei Teile der Methodik sind die folgenden: Geometriemodellierung, Ein- und Ausfluss-Randbedingungen und die *domain decomposition* der Simulationsbox zur effektiven computergestützten Berechnung.

Es stellte sich heraus, dass sich das SDPD-Fluid besser zur Modellierung der Ein- und Ausfluss-Randbedingungen eignet als ein DPD-Fluid, da letzteres zu starke Dichtefluktuation entlang des Kanals zeigt. So ist es schwierig, während des Flusses durch einen geraden Kanal die Dichte des DPD-Fluids zu kontrollieren. Dieses Problem tritt für das SDPD-Fluid weder in dieser noch in komplexeren Geometrien mit mehreren Verzweigungen und Ein- und Ausflüssen auf, da für dieses die auf die Partikel wirkende Kraft in Abhängigkeit von der lokalen Dichte des Fluids berechnet wird.

Contents

List of Figures	xxi
List of Tables	xxv
1. Introduction	1
1.1. Blood	2
1.2. Physical basis	6
1.3. Simulation methods	8
1.4. Blood cells under flow	11
1.4.1. Lift force	13
1.4.2. Attractive interactions	14
1.4.3. Cell-free layer	14
1.5. The Fokker-Planck equation	15
2. Fluid model	17
2.1. Dissipative particle dynamics	17
2.2. Smoothed dissipative particle dynamics	19
2.3. Time evolution	20
2.4. Fluid viscosity	20
2.5. Boundary conditions	21
3. Blood simulation	25
3.1. Cell model	25
3.1.1. 2D RBC model	25
3.1.2. 3D RBC model	26
3.1.3. Membrane surface triangulation	28
3.2. RBC dynamics	30
3.2.1. Particle dynamics in shear flow	30

3.2.2.	RBC dynamics in Poiseuille flow	32
3.3.	Blood flow simulations	33
3.3.1.	RBC interactions	33
3.3.2.	RBC distribution in flow	34
3.3.3.	Cell-free layer	36
3.3.4.	RBC interactions. Morse potential	38
4.	Microvascular blood flow resistance: role of red blood cell migration and dispersion	39
4.1.	Introduction	39
4.2.	Models & Methods	41
4.2.1.	SDPD model	41
4.2.2.	RBC model	42
4.2.3.	RBC aggregation model	42
4.2.4.	Cell-free layer	42
4.2.5.	Simulation setup	43
4.3.	Results	45
4.3.1.	Cell-free layer evolution	45
4.3.2.	Effect viscosity contrast	46
4.3.3.	Effect of RBC aggregation	49
4.3.4.	Theoretical model for CFL	50
4.4.	Discussion	53
4.5.	Summary	57
5.	Segregation mechanism of multicomponent suspension under flow	59
5.1.	Introduction	59
5.2.	Models & Methods	61
5.2.1.	Fokker-Planck equation	61
5.2.2.	Fluid model	62
5.2.3.	Model of blood cells	62
5.3.	Results	62
5.4.	Summary	65
6.	Simulation of complex geometries	69
6.1.	Introduction	69

6.2. Outflow boundary conditions	69
6.3. Inflow boundary conditions	72
6.4. Volumetric driving force	73
6.5. Inflow of RBCs	74
6.6. Summary	75
7. Concluding Summary	77
8. Outlook	83
Appendix A. Single vesicle flow behavior	89
A.1. Keller-Skalak theory	89
Appendix B. Simulation of complex geometries	91
B.1. Domain construction	91
B.2. Domain decomposition	92
Bibliography	95

List of Abbreviations

RBC	Red blood cell
WBC	White blood cell
CFL	Cell-free layer
DPD	Dissipative particle dynamics
SDPD	Dissipative particle dynamics
NSE	Navier-Stokes equation
COM	Center of mass
2D	Two-dimensional
3D	Three-dimensional
BC	Boundary conditions
LJ	Lennard-Jones
MSD	Mean square displacements
MPC	Multi-particle collision dynamics
LB	Lattice-Boltzmann method
TT	Tank-treading motion
TB	Tumbling motion
SW	Swinging motion

List of Symbols

D_{RBC}	RBC diameter
T	Temperature
k_B	Boltzmann constant
\mathbf{v}	Velocity vector
\mathbf{r}	Position vector
p	Pressure
ρ	Density
η	Dynamic viscosity
$\mathbf{F}, \mathbf{f}, f$	Force
Re	Reynolds number
$\dot{\gamma}$	Linear shear rate
$\bar{\dot{\gamma}}$	Average linear shear rate
h_v	Distance from a wall
N_p	Number of point particles
\mathbf{F}_C	Conservative force
\mathbf{F}_R	Random force
\mathbf{F}_D	Dissipative force
r_c	Cut-off radius
a	Conservative force coefficient
\mathbf{e}	Unity position vector
ω^D	Dissipative force weight function
ω^R	Random force weight function
γ	Dissipative force coefficient
σ	Random force coefficient
dt	Simulation timestep
k	Exponent of dissipative weight function
m	Mass
N	Number of particles

W_t	Wiener process
p_0, α, b	Parameters for SDPD equation of state
t	Time
r_w	Near-wall thickness for adaptive shear force
Δh	Distance from wall
C_k	Adaptive force strength
α_r	Relaxation parameter
\bar{V}, \bar{v}	Average velocity
N_v	Number of vertices
N_t	Number of triangles
N_s	Number of springs
l_j, l_0, l_m	Spring lengths (instantaneous, equilibrium, maximum)
k_p	Spring constant
η_m	Membrane viscosity
k_b	Bending constant
θ	Bending angle
U	Potential energy
A, A_0^{tot}	Area of a cell (instantaneous, desired)
A_j, A_0	Area of triangle (instantaneous, desired)
V, V_0^{tot}	Volume of a cell (instantaneous, desired)
k_a, k_d, k_v	Global and local area, volume constraint coefficients
D	Diffusion constant
n	Number density
λ	viscosity contrast
R_0	Effective vesicle radius
L_x, L_y, L_z	Length of simulation box
σ_{LJ}	Lenard-Jones Radius
ϵ	Strength of LJ potential
$\dot{\gamma}^*$	Normalized shear rate
H_t	Hematocrit
δ	Thickness of near-wall region
R	Channel radius
Q	Flow rate
τ	Characteristic time scale

φ	Angle between neighbor bonds
k_s	Spring strength
λ	Viscosity contrast
τ_{RBC}	Characteristic relaxation time of the vesicle
L, l_c	Channel length

List of Figures

1.1. Example of an occlusion caused by sickle-cells	2
1.2. Blood cells images from Scanning electron microscope	3
1.3. Spectrin network of RBC	4
1.4. Example of biocomputing nanoparticle	6
1.5. Laminar flow	8
1.6. Segregation example	12
1.7. Pressure field around a TT vesicle	13
1.8. Reuleaux structure	14
2.1. DPD method	18
2.2. Reverse Poiseuille flow rheometer	21
2.3. Lees-Edwards boundary conditions	23
3.1. 2D RBC model	26
3.2. Low-dimensional RBC model	27
3.3. TT and TB motions of a vesicle	30
3.4. RBC dynamics in flow	31
3.5. RBC parachute shape	32
3.6. RBC zigzag-slipper shape	32
3.7. LJ potential	33
3.8. Blood flow profile	35
3.9. Hematocrit across the channel	35
3.10. CFL measurement in simulations	37
3.11. Morse potential	38
4.1. Simulation snapshots for $D = 40 \mu\text{m}$ and $H_t = 0.3$	44
4.2. Development of the CFL thickness in time after flow has been started for the case of $H_t = 0.3$ and $D = 20 \mu\text{m}$	44

List of Figures

4.3.	Development of the CFL thickness in time after flow has been started for the case of $H_t = 0.45$ and $D = 20 \mu\text{m}$	46
4.4.	Development of the hematocrit profile in time after flow has been started for the case of $H_t = 0.45$, $D = 20 \mu\text{m}$	47
4.5.	Development of the CFL thickness in time after flow has been started for the case of $D = 40 \mu\text{m}$	47
4.6.	$D = 20 \mu\text{m}$ and $H_t = 0.3$: (a) CFL development over time for the simulations with viscosity contrast. (b) hematocrit distribution across the channel for simulations with and without viscosity contrast.	48
4.7.	Comparison of permeable and non-permeable vesicles	49
4.8.	Effect of RBC aggregation on CFL	50
4.9.	CFL thickness for a converged flow for different flow rates and channel diameters	51
4.10.	Final CFL thickness for different flow rates, hematocrits, and channel diameters	53
4.11.	Relative viscosity of blood flow for different H_t values, flow rates, and RBC aggregation	56
5.1.	Examples of different margination behavior	60
5.2.	Snapshot of the simulation setup	63
5.3.	Acting force on target particles and a distribution of the target particles	63
5.4.	Snapshot of the simulation setup for diffusion measurements	64
5.5.	Diffusion constant of target cell	65
5.6.	Diffusion constant depending on shear rate and hematocrit value for target cell	66
5.7.	Theoretical and simulation results	66
6.1.	Simulation snapshot of a model of vascular branching.	70
6.2.	Outflow boundary condition	70
6.3.	Density profile for in- and outflow simulations with volume force.	73
6.4.	Periodic feeding domain	75
8.1.	Example of a branching model	83

8.2. Microfluidic device	84
B.1. Colud of points to create the surface for complex geometries . .	91
B.2. Triangulated surfaces for complex geometry simulation	92
B.3. Simulation setup and its domain decomposition	93

List of Tables

3.1. RBC characteristics in units of the effective RBC diameter . . .	29
4.1. SDPD fluid parameters used in simulations	42

1. Introduction

In 1808 Thomas Young has started his report in Royal Society with the words that mechanical motion inside a living body are governed by the same laws as laws for inanimate bodies, so that blood flow in arteries and venules can be described using certain laws from hydraulics [114]. Although we know Young from the elastic modulus and the wave theory of light, he was not only professor of Physics, but also a medical doctor. Such a diverse activity was very common at those times; however, nowadays science becomes more specialized. Nevertheless, engineers and physicists bring together more and more understanding of various processes in medicine and biology.

Blood is an essential liquid in our body. In diseases like in diabetes, sickle-cell anemia or malaria, blood properties might change. In diabetes, the blood sugar level rises and changes viscosity of the blood. This can cause cardio-vascular diseases, such as stroke [12]. Sickle-cell anemia is a genetic disease where RBCs in deoxygenated state have not a normal biconcave but a sickle shape and become stiffer. When deoxygenated, RBC's hemoglobin forms strands which push the membrane from inside causing an abnormal shape and rigidity. These RBCs can not pass through small arteriols and capillaries, causing occlusions (Fig. 1.1).

Malaria disease is caused by parasitic protozoans from the genus Plasmodium. The parasite is transmitted by mosquitoes. Once inside a body, it is able to attach to a RBC membrane, penetrate inside a cell, and affects its stiffness. The changed properties of infected RBCs lead to their different behavior in blood flow. For example, such RBCs have different motion and can be differently arranged in flow. Since infected cells are stiffer than healthy cells, microfluidic devices are being developed to separate infected cells from healthy ones, for a further analysis.

Hence, a thorough understanding of blood properties and its cells is required.

1. Introduction

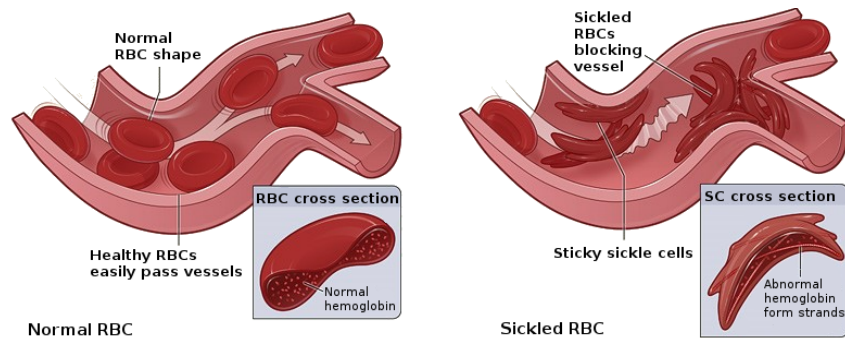


Figure 1.1.: (Left) Figure healthy RBCs can easily pass through microvessels, because of their high deformability. (Right) Sickle-cell (SC) occlusion example shows the typical situation, when stiff RBCs are blocking the microvessel at a branching point. The illustration is taken and modified from National Heart, Lung and Blood Institute, <http://www.nhlbi.nih.gov>.

These processes and changes in blood flow are investigated not only experimentally, but also numerically. Simulations provide an opportunity to model and examine such a system in a faster and cheaper way, bringing new insights in addition to experimental measurement.

1.1. Blood

Blood carries oxygen, nutrients, some proteins, hormones etc. to body cells and takes away metabolic wastes. Heart pumps the blood to keep a pressure difference which makes blood to flow similarly to any building's heating system. Blood is oxygenated in the lungs and travels around the body through aorta, arteries, arterioles, capillaries, venules, veins, returning back to the lungs. The body of an adult has about 5 liters of blood. One circle takes approx. 20 seconds, which means that RBCs come back to the heart three times per minute. This also means that during one day, the heart pumps over 7000 liters!

For most species, the oxygen is carried by RBC's hemoglobin, but there are some animals such as crustaceans and mollusks which use hemocyanin. Hemocyanin sometimes gives the body a blue color, because of the copper in its structure.

In vertebrates, blood consists of plasma and cells suspended in it. Plasma constitutes 55% of blood by volume and has 92% of water. Salts, minerals,

proteins, glucose, blood cells and etc. are suspended in the plasma. RBCs or erythrocytes make the blood red and correspond to a major fraction by volume: up to 45%. White blood cells (WBC) or leukocytes are the immune cells, which protect the body from infections and foreign invaders. WBCs take up to 1% of blood volume. Finally, platelets or thrombocytes help to stop bleeding and play a significant role in a wound healing process. The number ratio of platelets to RBCs is about 1 : 10 to 1 : 20.

RBCs are cells without nucleus and their role is to carry hemoglobin for oxygen transport. Hemoglobin has iron in its structure, which gives RBCs red color. A single erythrocyte has a discoidal biconcave shape, with a diameter between 6 and 10 μm , depending on its age and a thickness of 2 μm (Fig 1.2). RBCs are very deformable, and can go through capillaries with diameters down to 3 μm . RBCs have a very high area to volume ratio, which helps to better take up and release oxygen. Though RBCs carry oxygen, the carbon dioxide is taken away by plasma.

RBCs are produced in the bone marrow and have a life expectancy about 110 days, after which they get destroyed by macrophages. One of the very important properties of blood is RBC volume fraction or hematocrit H_t . H_t varies from 37% to 55% depending on location. Also, hematocrit values are a bit lower for women than those of men.

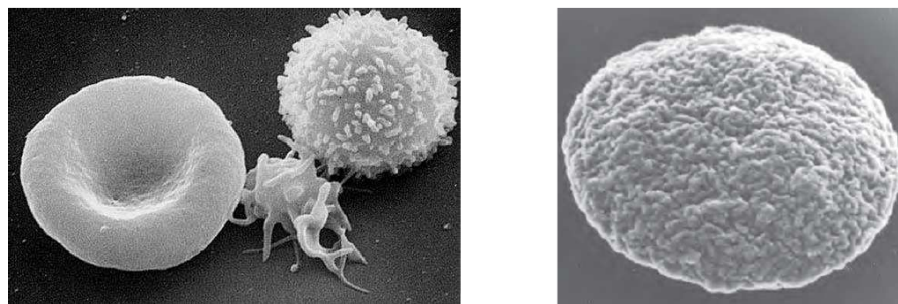


Figure 1.2.: Blood cells images from Scanning electron microscope. From left to right: RBC, activated platelet, WBC, non-activated platelet. The origin of images: (left) The National Cancer Institute at Frederick (NCI-Frederick), (right) Ref. [69].

The membrane of a RBC consists of three layers: glycocalyx on the outside of the cell, a lipid bilayer with many transmembrane proteins, and a cytoskeleton which is located under the lipid bilayer. The cytoskeleton (Fig. 1.3) is a network

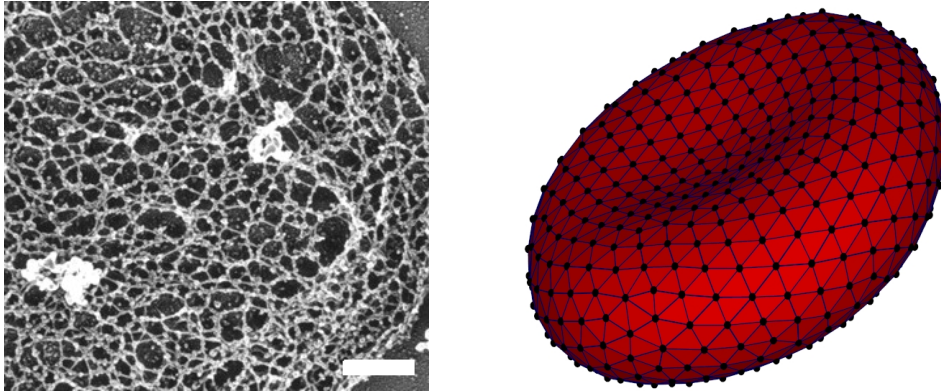


Figure 1.3.: Spectrin network of a RBC. Left: spectrin skeleton of a mouse from Ref. [50] with the bar of $200 \mu\text{m}$; Right: triangular network model from Ref. [26] used for simulations.

of spectrin proteins which makes a RBC more durable. Even though a RBC is highly deformable, it nearly conserves its volume and area. Moreover, due to these three layers a membrane possesses viscoelastic properties [40].

Another major component of blood is a platelet or thrombocyte (Fig. 1.2 right). In adult human body there are about $15 - 40 \times 10^4$ platelets per mm^3 of blood. Platelets are responsible for patching damaged vessels and stopping bleeding. They have a biconvex discoidal lens-shape and are about $3 \mu\text{m}$ in diameter [41]. Platelets are produced in bone marrow and circulate in blood for 7 – 10 days. They also have no nuclei and are much stiffer, than RBC. Similar to RBCs, platelets have an internal cytoskeleton which consists of actin and tubulin polymers.

If the endothelial layer of a vessel is damaged or interrupted, platelets come to this site and patch the hole. Firstly, they adhere to the damaged vessel wall with a help of von Willebrand factor. This is possible through the activation of their receptors and shape change (Fig. 1.2 left). Lastly, they bind to each other and form a plug. After platelets have formed a plug, the healing process is not yet finished and the tissue has to be repaired. This process is an initial part of a complex wound-healing mechanism, causing the bleeding to stop. A low platelet count in blood might cause long bleeding times. A high platelet count or vessel wall irregularities might cause venous and arterial thrombosis.

WBCs (Leucocytes) have a spherical shape and a diameter of $6 - 20 \mu\text{m}$

depending on the type (Fig. 1.2 left). There are about $(4 - 11) \times 10^3$ WBCs per microliter of blood. Distinct from RBCs and platelets, WBCs have a nucleus. Leucocytes are part of the body immune system. They protect the body from infectious diseases and foreign invaders. WBCs can transmigrate through vessel walls to tissue by adhesion on the wall to reach the infection. WBCs are produced in bone marrow and there exist five WBC types with different physical and functional properties.

WBCs help to remove foreign substances e.g. viruses, bacteria, drugs, since they are foreign objects, unknown to the immune system. Malaria parasites bypass this protection by hiding inside the RBC, such that WBCs can not detect them. An increased number of WBC above a certain limit in blood usually indicates an inflammation. There might be also an increased production by bone marrow, a decreased uptake by tissue cells and a decreased attachment to the vessels walls.

More and more artificial particles are produced nowadays for therapeutic or other reasons. They might be of different sizes: from nano- to micro-scales. Scientists try to develop particles which can be easily taken up by body cells, stay long enough in the body, cause less damage, get certain spreading over the body. These nano- and micro-particles, might be of different shapes and structures: spheroid, polymer-like, encapsulated, etc [5].

It is very important to be able to control the distribution of nano- and micro-particles [98] in order to deliver them where they are needed. In many cases adhesion of these particles to target sites is desired. In microvessels, particles should be able to migrate through the walls and avoid WBCs, to bring drugs to targeted cells. This migration process depends on size of the particles so they may not be able to go through the wall or even pass through the capillaries, if their diameter is too large. Also, flow dynamics may not let a drug particle to come close to the vessel wall. Moreover, their adhesion is another aspect, which can reduce the efficiency of particle delivery.

As RBCs make one circle from the heart and back in about 20 sec, extra particles are get expected to have similar circulation times. Different shapes and sizes of nano-particles and micro-particles were investigated for their efficiency. For example, it is difficult for big particles with diameters $D_p > 4 \mu\text{m}$ to pass through capillaries, because they can stuck there [102]. Particles with $D_p \leq 3$

1. Introduction

μm are easily taken up by the immune system in liver, spleen or lungs [17, 47]. Circulation in the body of particles with $150 \text{ nm} < D_p < 200 \text{ nm}$ appeared to be much longer than that of particles which $D_p > 300 \text{ nm}$ or $D_p < 70 \text{ nm}$ [62]. On the other hand, it was shown recently that spherical particles of diameter $D_p \approx 2 \mu\text{m}$ have a higher adhesion rate, than smaller nanoparticles, but the latter are much easier for endocytosis, or cell uptake [74, 75].

Another property, which can affect drug efficiency is the shape of a particle. Spherical particles are worse than discoidal ones in terms of accumulation in organs [17]. Elongated particles are more resistant to the immune system, but have less opportunity to pass in between endothelial cells [10, 74]. Adhesion of different particle shapes has been studied both theoretically [16] and experimentally [42].

These results lead to the idea of compound particles, which could possess the properties of different types of particles. Such a compound particle can be developed by means of biocomputing, where a nano-particle is able to "decide" based on simple logic operators [3, 65] (Fig. 1.4).

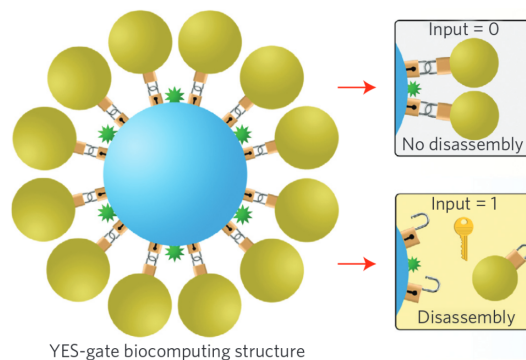


Figure 1.4.: Biocomputing nanoparticle example. Following the input signal, the covering yellow particles disassemble and open the output green receptor. From Ref. [65].

1.2. Physical basis

Blood behavior in microcirculation can not be explained using a continuous fluid model. Soft matter physics investigates substances such as blood, polymer solutions, self-propelled particles (Janus particles, E.coli bacteria), gels, etc.

Characteristic length scales for soft matter are in the range from 10 nm to 10 μm . Interesting behaviors of these materials can not be explained based on atomistic or molecular structure of the materials. For instance, soap bubbles are large in comparison with molecules which form it, and the macroscopic mechanical properties of a foam are derived from interactions between bubbles. As in a soap solution, many of soft matter are one- or multi- component suspensions in a buffer solvent. Interactions with the solvent play an important role, especially in cases where flow is applied.

Hydrodynamics deals with fluids in motion, e.g. water in pipes. Therefore, hydrodynamics laws can be employed to describe the dynamics of fluids. If we use Newton's second law to describe the motion of a viscose fluid, we can derive the Navier-Stokes equation (NSE):

$$\begin{aligned} \rho \left(\frac{\partial \mathbf{v}}{\partial t} + (\mathbf{v} \cdot \nabla) \mathbf{v} \right) &= -\nabla p + \eta \nabla^2 \mathbf{v} + \mathbf{f}_{ext} \\ \nabla \cdot \mathbf{v} &= 0 \end{aligned} \quad (1.1)$$

where \mathbf{v} is the velocity vector, p is the pressure field, η is dynamic viscosity, and \mathbf{f}_{ext} is external force. The NSE is widely applied across the fluid-dynamics field, starting from hydrodynamics of a system with quite high density, and ending with gas flows. In combination with Maxwell's equations they can describe magnetohydrodynamics.

The NSE becomes much simpler, if the fluid inertial forces compared to viscous forces characterized by Reynolds number Re , is insignificant ($Re \ll 1$). Re is a dimensionless number, which is defined as follows:

$$Re = \rho V_{ch} L_{ch} / \eta \quad (1.2)$$

where ρ is the fluid density, V_{ch} and L_{ch} are characteristic flow velocity and length. Flow pattern at a low Re is laminar (Fig. 1.5), i.e. flow layers stay parallel without disruptions between them. In that case NSE takes a simple form:

$$\begin{aligned} \nabla p - \eta \nabla^2 \mathbf{v} &= \mathbf{f}_{ext} \\ \nabla \cdot \mathbf{v} &= 0 \end{aligned} \quad (1.3)$$

1. Introduction

because, if $Re \ll 1$ we can neglect the part $\rho(\mathbf{v} \cdot \nabla)\mathbf{v}$ and the part $\frac{\partial \mathbf{v}}{\partial t}$ is zero because we consider the steady flow. This system is called Stokes equation. Such a flow has an interesting property: solutions are time-reversible, ie time-reversed flow can be described by the same equation, as the direct one.

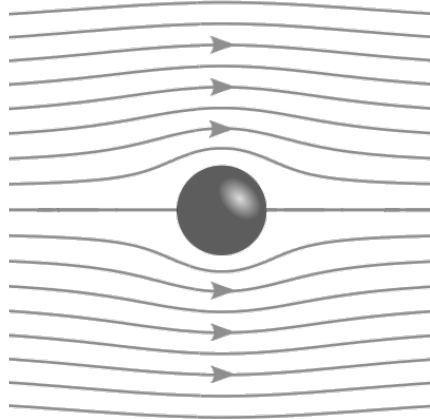


Figure 1.5.: A fixed sphere in laminar flow. Streamlines are parallel and do not cross.

1.3. Simulation methods

The dynamical behavior of these many-body systems is very complicated. Several decades ago scientists would calculate positions and velocities of small number of particles particles by hand on paper. Nowadays simulations play an important role in science and engineering, providing the possibilities to make fast computations and bring new insights to complex systems. One of the first simulation methods was Monte Carlo (MC) simulation. The Monte Carlo method is widely used and based on a repeated random sampling, leading to the final distribution of system states. To conclude, MC method can be used to describe any problem having a probabilistic nature.

Another simulation method is Molecular Dynamics (MD). This method is based on an approach, where particles interact with each other by means of the Newton's second law. With a large number of particles a discretization scheme is needed. Using appropriate discretization, the method repeatedly calculates the positions and velocities according to the equation of motion. Although, MD is

computationally expensive for mesoscopic simulations, it is very popular. Also, the MD method includes thermal fluctuations and hydrodynamic interactions.

If we switch from the Newton's second law to Langevin equation [14] in our simulations, we will obtain Brownian dynamics. The Langevin equation 1.4 is a stochastic differential equation describing for example a random movement of a particle in a fluid. There is an additional term in Langevin equation, that mimics the random kicks, or thermal motion by the molecules of the fluid.

$$m \frac{d^2 \mathbf{x}}{dt^2} = -\lambda \frac{d\mathbf{x}}{dt} + \varepsilon(t) \quad (1.4)$$

where λ represents viscous force which is proportional to the particles velocity, and a noise term $\varepsilon(t)$ is random collisions with the fluid molecules with a Gaussian probability distribution and properties $\langle \varepsilon(t) \rangle = 0$, $\langle \varepsilon(t) \varepsilon(t') \rangle = D \delta(t - t')$, where D is diffusion and $\delta(t)$ is the Dirac delta-function.

Unfortunately, in the Brownian dynamics there are no hydrodynamic interactions. However, through the inclusion of Oseen tensor, the problem can be eliminated. The Oseen tensor is used as a simplified description of hydrodynamic coupling in the fluid. Due to linearity of the Stokes equation for an incompressible Newtonian fluid exists a solution in Green's function, known as the Oseen tensor. If we add to the equations 1.3 that the boundary conditions are vanishing at infinity $|\mathbf{v}|, p \rightarrow 0$ as $\mathbf{r} \rightarrow \infty$, and replace the forcing term by a point force acting at the origin $\mathbf{F} \delta(\mathbf{r})$, the solution for the $\mathbf{v}(r)$ and $p(r)$ are given by:

$$\begin{aligned} \mathbf{v} &= \mathbf{F} \cdot \mathbf{J}(\mathbf{r}) \\ p(\mathbf{r}) &= \frac{\mathbf{F} \cdot \mathbf{r}}{4\pi r^3} \end{aligned} \quad (1.5)$$

where $\mathbf{J} = \frac{1}{8\pi\eta} \left(\frac{\mathbf{E}}{r} + \frac{\mathbf{r}\mathbf{r}}{r^3} \right)$ and \mathbf{E} is unit tensor.

There are two ways to include hydrodynamic interactions into the methods above: on-lattice and off-lattice. In Lattice-Boltzmann Method (LB), instead of solving NSE, the Boltzmann equation is solved on a discrete lattice to simulate fluid flow. Although, solving Boltzmann equations does not include thermal noise, it was explicitly added in new versions of the LB method [44]. One of the shortcomings of the method is that Galilean invariance is not conserved

because of the lattice.

Another simulation technique, Multi-particle collision (MPC) dynamics [44], is an off-lattice method that incorporates both thermal fluctuations and hydrodynamics. In this method, a simulation domain is divided into cells. System evolution consists of streaming and collision steps: in the streaming step particles move in a ballistic way, while in the collision step the center of mass (CM) velocity of every cell is calculated and all relative velocities of cell particles are randomly rotated. The cell's position is updated before the rotation in order to conserve Galilean invariance.

In this thesis, we use the Dissipative Particle Dynamics (DPD) method [22]. In this method, every DPD particle is considered to be a representation of a small fluid cluster rather than single atoms. A DPD particle is a statistical depiction of such a cluster in equilibrium. Every particle interacts with each other in the Newtonian way via pairwise forces: conservative, dissipative and random. Dissipative and random force are chosen such that they fulfill fluctuation-dissipation theorem and act as a thermostat.

As an improvement of the DPD method, Smoothed DPD (SDPD) [21] was introduced by mixing DPD and smoothed particle hydrodynamics SPH [70, 71]. SPH is a method for simulating a fluid flow, that came to fluid simulations from astrophysics. The method works by dividing the fluid into a number of discrete elements. A property to be determined is substituted by a sum of the relevant properties over the particles in the element, or so-called *kernel*. As an advantage of SDPD, equation of state, transport coefficients can be input directly, and the modeled fluid has less compressibility artifacts than that in the DPD method. However, SDPD is computationally more expensive than DPD. The SDPD was recently improved to include angular momentum conservation [73] which can be crucial for modeling multi-phase suspensions.

In addition, there are simulation models, which combine several different methods to capture different scales of a system. For example, to model blood flow in large vessels a continuous approach is sufficient, so there is no need in simulating blood cells explicitly. In the domains, where these large vessels branch into two or more smaller ones, or to investigate blood flow in an aneurysm [31], it might be useful to apply a particle-based method, like DPD or SPDP. In cases where even smaller scale is needed, the model can be

complemented by atom- or molecular-level approaches like MD. In this work, simulations were done using DPD and SDPD methods, and they will be discussed in detail later in Chapter 2.

1.4. Blood cells under flow

It is possible to use continuous approach to model blood flow in vessels down to $200\ \mu\text{m}$ [25]. Blood exhibits a non-Newtonian behavior at small capillaries because RBC size becomes comparable with channel diameter and should be taken into consideration.

The collective flow behavior of RBCs is affected by the motion of single cells. A RBC under different conditions, such as confinement, flow rate, inner-to-outer viscosity difference may move differently. The most common and known dynamics in simple shear flow are tank-treading (TT), tumbling (TB) and swinging or breathing (SW) motions.

A RBC in TT motion reminds of the motion of a tread of a tank, so that the shape and relative position of the cell are not significantly changing, but the membrane of a cell moves around its center of the mass (COM) with a constant angular velocity. The inclination angle of a cell with respect to flow direction stays also constant.

In the TB regime, the cell rotates around its COM almost like a rigid body without motion of the membrane. The rotation velocity also remains quite stable.

The third motion (SW) can be considered as an intermediate regime between TT and TB. The cell or vesicle is in TT motion and oscillates about a certain inclination angle with a stable periodicity [1, 76]. These motions were observed experimentally [1, 54], and in simulations, while TT and TB motions were also described theoretically [55].

In Poiseuille flow, a RBC has a parachute shape, normal biconcave shape, and slipper shape (Fig. 3.5, 3.6) [26, 66, 95]. These shapes have been discovered in experiments as well [106]. There are also different shapes, which might be corresponding to variations of the shapes discussed above.

The motion of a single RBC is interesting, because depending on the type of

1. Introduction

motion it is possible to construct microfluidic devices to separate them from each other based on their intrinsic properties. This is also important for the prediction of flow resistance, and the development of more efficient drug-delivery processes.

Blood as a multicomponent suspension can segregate under flow. Segregation means that different components of the suspension may occupy different positions in flow. For example, RBCs are likely to be found in the center of the channel in Poiseuille flow, but WBCs marginate to the walls (Fig. 1.6). Similar segregation pattern can be observed for platelets in simulations and experiments [72, 105]. Segregation of different particles in flow is considered to depend on differences in size and shape, particle elasticity, collisions with other particles, shear-induced diffusion, and lift force which pushes cells away from the walls [57].

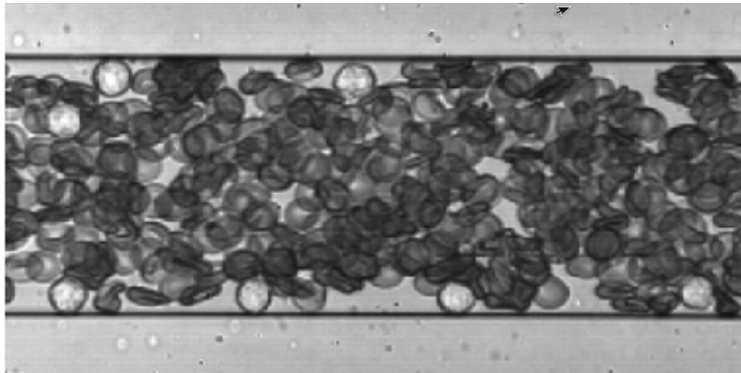


Figure 1.6.: Segregation of WBCs in Poiseuille flow. RBCs are occupying the center of the flow. WBCs are pushed toward the walls. The figure from [101].

If the shear rate is high, then the diffusion constant should be also large. Due to a fast flow velocity, the particles will have more kicks from neighboring particles. This frequency of the collisions will sum up into an effective the diffusion. If one the particles in a pair collision is softer than the other, the resulting displacement for the softer particle will be less, in comparison with the stiffer one. Soft particles can bypass stiff particles and maintain the position in a flow.

1.4.1. Lift force

In addition to the shear-induced diffusion, every non-spherical particle under flow experiences a lift force. The nature of this force is hydrodynamic: TT membrane motion directs the fluid towards the wall, resulting in a cell-wall interaction. Thus, the particle experiences pressure difference and moves away from the wall (Fig. 1.7).

The hydrodynamic lift force depends on vesicle's elasticity, shape, and dynamics. A rigid sphere will not experience this force, because of the reversibility of the Stokes flow: if in a direct shear flow the particle moves away from the wall, then in reversed setup it should move to the wall, but it will still move to the center, because there is no difference between these two setups. As a result of such a symmetry breaking, the rigid sphere does not experience the lift force. A vesicle in TB motion undergoes a smaller lift force, than that in TT motion. The lift force is larger for big vesicles in comparison to small ones [2, 103], depending algebraically on a characteristic radius with a power between 3 and 4 [2, 79, 103]. It has been suggested that the lift force decays as a squared distance from the wall, and proportional to the shear rate $F_l \sim \dot{\gamma}/h^2$ [2, 68].

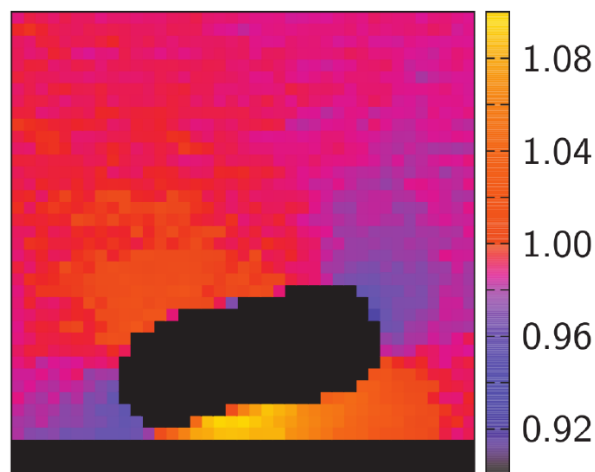


Figure 1.7.: Pressure field around a TT cell in shear flow, given by the color map. The image is taken from Ref. [68].

Even though lift forces act on every non-spherical particle in flow, there are still particles located near the walls. In case of different volume ratios of different particle types, one type can experience a stronger lift force and is

more probable to be found at the channel center.

1.4.2. Attractive interactions

RBC position at the center of a channel during flow makes blood to exhibit a non-Newtonian shear-thinning behavior. At high shear rates blood viscosity is lower, than that at low shear rates, because when RBCs occupy the center, plasma acts as a “lubrication” layer for the central flow, reducing blood viscosity. This effect can be enhanced by aggregation of RBCs, or so-called rouleaux structure (Fig. 1.8). That structure remains a stack of coins and is considered to form due to either depletion interaction because of an effect of different proteins solved in the blood on RBCs, or bridging by some blood proteins. Although, rouleaux is not possible without proteins in plasma. However, at high shear rates the structure get destroyed and aggregation forces are no longer relevant.

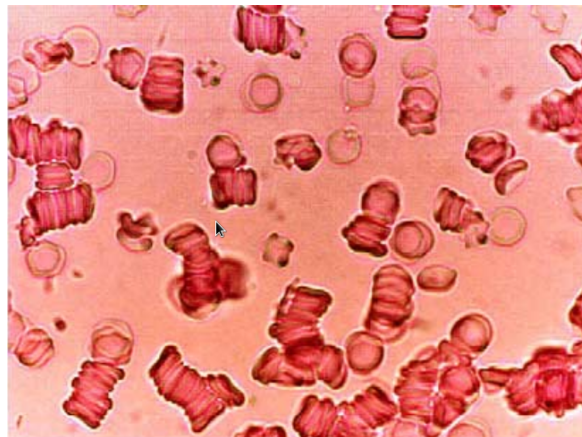


Figure 1.8.: Reuleaux structure of RBCs. At low shear rates RBCs stick to each other and form structures, which remind a stack of coins. These structures can enhance blood shear thinning. The figure is taken from Ref. [78].

1.4.3. Cell-free layer

Cell-free layer (CFL), or plasma “lubrication” layer is another important property of blood flow in capillaries. The thickness of CFL affects whole blood resistance and discharged hematocrit (difference between hematocrits of the

blood going into a channel and an out-going one) in Fahraeus-Lindqvist effect [38]. A particle in a body blood flow has an dilemma: from one side, a particle placed in blood should come closer to the channel center in order to spread as fast as possible around the body, on another side the particle should marginate at the wall to transmigrate through it and get the target tissue.

The CFL is very thin without flow; once a flow is applied, the CFL is getting thicker and reaches a certain value for a fixed flow rate. The CFL layer is thicker for high flow rates, since the lift force pushes particles stronger away from the walls. However, there is a limit of cell packing on the center above which CFL can not develop, because cell-cell interactions counteract the lift force. Thus, the CFL development can be considered as a competition between the lift force and cell-cell interactions.

1.5. The Fokker-Planck equation

To investigate the segregation process from a theoretical point of view, the Fokker-Planck equation is a very useful instrument. The equation describes the time evolution of a probability density function both for classical and quantum systems. Also, it is known as Kolmogorov forward equation, since it was introduced by Andrey Kolmogorov in his paper [56]. In application to particle distribution it is also called Smoluchovski equation.

If we start from the Langevin equation and switch from particle coordinates to a probability distributions and path integral, we will get the Fokker-Planck equation. The equation describes particles distribution through the forces on particles, and their diffusion constant, like in Brownian motion:

$$\frac{\partial}{\partial t} P(x, t) = -\frac{\partial}{\partial x} [\mu(x)P(x, t)] + \frac{\partial^2}{\partial x^2} [D(x)P(x, t)] \quad (1.6)$$

where $P(x, t)$ stays for probability density, $\mu(x)$ is the viscosity of the fluid, and $D(x)$ is the diffusion constant.

In this work we investigate blood flow resistance through straight channels and its dependence on hematocrit, flow rate, RBCs aggregation. Also, we apply

1. Introduction

Fokker-Planck equation to the segregation of a two-component suspension in order to describe the phenomenon using only force and shear-induced diffusion.

2. Fluid model

Hydrodynamic interactions are essential in blood flow simulations. In this chapter the simulation fluid model and boundary conditions used for modeling will be reviewed.

2.1. Dissipative particle dynamics

For our $2D$ simulations we use DPD method. DPD is a mesoscopic simulation method, which is in between the microscopic and continuous modeling methods. Every DPD particle represents a cluster of microscopic particles (Fig. 2.1). In a DPD system N particles interact with each other via three pairwise forces - conservative, dissipative and random. The Newton's second law of motion governs the evolution of particle positions and velocities over time as

$$d\mathbf{r}_i = \mathbf{v}_i dt, \quad d\mathbf{v}_i = \frac{1}{m_i} (\mathbf{F}_i^C + \mathbf{F}_i^D + \mathbf{F}_i^R) dt, \quad (2.1)$$

where \mathbf{F}^C , \mathbf{F}^D , and \mathbf{F}^R are conservative, dissipative, and random forces due to inter-particle interactions, respectively.

The acting force on a particle can be written as:

$$F_i = \sum_j F_{ij} = \sum_j (F_{ij}^C + F_{ij}^D + F_{ij}^R), \quad (2.2)$$

the sum goes over all neighboring particles within a cutoff radius. Conservative force is responsible for fluid compressibility and repels the particles away from each other, and dissipative is responsible for viscosity. Random and dissipative forces make up a thermostat, with a controlled equilibrium temperature.

2. Fluid model

The conservative force between two particles, i and j is usually defined as:

$$F_{ij}^C = \mathbf{e}_{ij} \begin{cases} a_{ij}(1 - r_{ij}/r_c), & \text{if } r_{ij} \leq r_c \\ 0, & \text{if } r_{ij} > r_c \end{cases} \quad (2.3)$$

where $\mathbf{e}_{ij} = \frac{\mathbf{r}_{ij}}{r_{ij}}$ is the unit separation vector directed from one particle to the other, r_c is a cut off radius, r_{ij} is the distance between the particles, and a_{ij} is a repulsion constant.

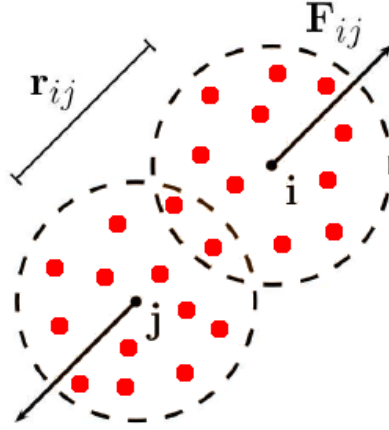


Figure 2.1.: Every small dot corresponds to a microscopic particle (e.g. atom or molecule), dashed circles defines DPD particle. In the DPD method every particle represents a cluster of microscopic particles.

The dissipative force is taken to be

$$F_{ij}^D = -\gamma\omega^D(r_{ij})(\mathbf{v}_{ij} \cdot \mathbf{e}_{ij})\mathbf{e}_{ij}, \quad (2.4)$$

with velocity $\mathbf{v}_{ij} = \mathbf{v}_i - \mathbf{v}_j$, a weight function $\omega_D(r_{ij})$, and the dissipative force coefficient γ .

The random force is calculated as:

$$F_{ij}^R = \sigma\omega_{ij}^R\xi_{ij}dt^{-\frac{1}{2}}\mathbf{e}_{ij}, \quad (2.5)$$

with the weight function ω_{ij}^R , random force coefficient σ , symmetric random number $\xi_{ij} = \xi_{ji}$ and timestep dt . The random number should also have unit

variance and zero mean ($\langle \xi \rangle = 0$). Galilean invariance is achieved because we use only relative variables (\mathbf{v}_{ij} and r_{ij}) in all forces.

In order for the DPD thermostat to maintain equilibrium temperature, the random and dissipative forces should fulfil the fluctuation-dissipation theorem [22]:

$$\omega_{ij}^D = [\omega_{ij}^R]^2, \quad \sigma = \sqrt{2k_B T \gamma} \quad (2.6)$$

Although, the weight function is a free choice, the original DPD approach is:

$$\omega_{ij}^R = \begin{cases} (1 - r_{ij}/r_c)^k, & \text{if } r_{ij} \leq r_c \\ 0, & \text{if } r_{ij} > r_c \end{cases} \quad (2.7)$$

with $k = 1$. Other values of k might be taken in order to increase the viscosity of a fluid.

2.2. Smoothed dissipative particle dynamics

Usually for 3D simulations we use the SDPD method. SDPD [21] is a mesoscopic hydrodynamics method based on two popular approaches: the smoothed particle hydrodynamics [64, 70] and the dissipative particle dynamics [22, 49] methods. In SDPD, a simulation system consists of N point particles with mass m_i , position \mathbf{r}_i , and velocity \mathbf{v}_i . The three pairwise forces on particle i are defined as follows

$$\begin{aligned} \mathbf{F}_i^C &= \sum_j \left(\frac{p_i}{\rho_i^2} + \frac{p_j}{\rho_j^2} \right) w_{ij} \mathbf{r}_{ij}, \\ \mathbf{F}_i^D &= - \sum_j \gamma_{ij} (\mathbf{v}_{ij} + (\mathbf{v}_{ij} \cdot \mathbf{e}_{ij}) \mathbf{e}_{ij}), \\ \mathbf{F}_i^R &= \sum_j \sigma_{ij} \left(dW_{ij}^S + \frac{1}{3} \text{tr}[d\mathbf{W}_{ij}] \right) \cdot \mathbf{e}_{ij}, \end{aligned} \quad (2.8)$$

where $\mathbf{e}_{ij} = \mathbf{r}_{ij}/|\mathbf{r}_{ij}|$ and $\mathbf{v}_{ij} = \mathbf{v}_i - \mathbf{v}_j$. p_i and p_j are particle pressures assumed to follow the equation of state $p = p_0(\rho/\rho_0)^\alpha - b$, where p_0 , ρ_0 , α , and b are selected parameters. Density of particles is calculated locally and determined as $\rho_i = \sum_j W_L(r_{ij})$ with $W_L(r) = \frac{105}{16\pi r_c^3} \left(1 + 3\frac{r}{r_c}\right) \left(1 - \frac{r}{r_c}\right)^3$ being the Lucy function [64], where r_c is the cutoff radius. Furthermore, $\nabla W_L(r) = -\mathbf{r}w(r)$

2. Fluid model

such that $w(r) = \frac{315}{4\pi r_c^5} \left(1 - \frac{r}{r_c}\right)^2$ and $w_{ij} = w(r_{ij})$. The coefficients γ_{ij} and σ_{ij} define the strength of dissipative and random forces and are defined as $\gamma_{ij} = \frac{5\eta_0}{3} \frac{w_{ij}}{\rho_i \rho_j}$ and $\sigma_{ij} = 2\sqrt{k_B T \gamma_{ij}}$, where η_0 is the desired dynamic viscosity of fluid and $k_B T$ is the energy unit. The notation $tr[d\mathbf{W}_{ij}]$ corresponds to the trace of a random matrix of independent Wiener increments $d\mathbf{W}_{ij}$, and dW_{ij}^S is the traceless symmetric part([93]).

2.3. Time evolution

The time evolution of particle position and velocity in a simulation with a timestep dt is determined by Newton's law of motion (Eq. 2.1), which is integrated using the modified version of velocity-Verlet algorithm [4]:

$$\begin{aligned}
 \mathbf{r}_i(t + dt) &= \mathbf{r}_i(t) + dt\mathbf{v}_i(t) + \frac{1}{2}(dt)^2\mathbf{f}_i(t), \\
 \tilde{\mathbf{v}}(t + dt) &= \mathbf{v}_i(t) + \frac{1}{2}dt\mathbf{f}_i(t) \\
 \mathbf{f}_i(t + dt) &= \mathbf{f}_i(\mathbf{r}_i(t + dt), \tilde{\mathbf{v}}_i(t + dt)) \\
 \mathbf{v}_i(t + dt) &= \mathbf{v}_i(t) + \frac{1}{2}dt(\mathbf{f}_i(t) + \mathbf{f}_i(t + dt)).
 \end{aligned} \tag{2.9}$$

2.4. Fluid viscosity

Simulated results need to be verified with physical ones to compare model parameters with real fluid properties. Reversed Poiseuille flow virtual setup was used to calculate the fluid viscosity and then calibrate all parameters Ref. [32]. Here, the computational domain assumes periodic boundary conditions and is divided into two parts, in every of which a fluid is driven in opposite directions. Since there are no walls, potential wall effects are eliminated. Fluid viscosity is calculated via fluid velocity-profile averaging and Poiseuille law.

The Reynold number of typical blood flow is $Re < 0.1$, so we can neglect inertial effects in our system. The highest possible Re saves computational time, because the system will develop faster with a faster characteristic velocity. To examine that we provide additional simulations with different setup parameters

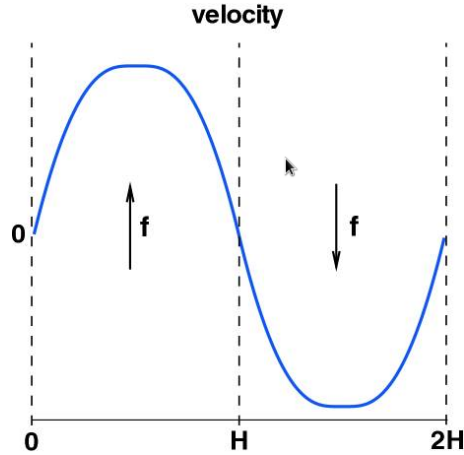


Figure 2.2.: Reverse Poiseuille flow simulation setup for fluid viscosity calculation. Periodic boundary conditions are assumed at every border.

and lower Re . If the results are identical, then we are still in the regime with low enough Re number.

2.5. Boundary conditions

In simulations, where confined flow behavior is investigated, the walls are modeled by frozen fluid particles. These walls are constructed from the snapshot of a simulation with the same particles in a fully periodic box. This is done to simulate the same fluid properties in the wall, save the computational time by not developing frozen particle's coordinates, and to eliminate the density fluctuations at the wall. Typically, the thickness of the walls is about r_c , since they do not increase the computational time. Frozen particles are included into the neighbor list calculation only from one side - their positions are not integrated. The interactions between frozen particles and all other particles are the same as those with the fluid particles.

The walls reflect all moving particles Ref. [31]. A fluid particle with a start position x^k and velocity \mathbf{v}^k which should encounter the wall at x_{BC} moving with a velocity \mathbf{v}_{BC} is considered. If at time t' so that $0 \leq t' < dt$, the fluid particle would encounter the wall, than new coordinate and velocity of the

2. Fluid model

particle shall be calculated in a different way:

$$\begin{aligned}
 t' &= (x^k - x_{BC}) / (v_{BC} - v^k), \\
 \mathbf{r}(t + dt) &= \mathbf{r}(t) + t' \mathbf{v}(t) + (dt - t') \mathbf{v}(t + dt), \\
 \mathbf{v}(t + dt) &= 2\mathbf{v}_{BC}(t) - \mathbf{v}(t).
 \end{aligned} \tag{2.10}$$

This is a bounce-back reflection rule, which is used to provide better no-slip boundary conditions in comparison to specular reflection [97]. Here, both tangential and normal velocities of the particle are reversed. In specular reflections, only the normal velocity component is reversed after the collision and a the higher friction needed for no-slip conditions.

In order to fully satisfy the no-slip boundary conditions, the adaptive shear force is introduced. The shear force acts in tangential direction on the fluid particles closer than r_w to the wall. The force is calculated on the basis of velocity difference between the estimated fluid velocity at the wall and v_{BC} :

$$f_t(\Delta h) = C_k(\Delta v_t) \left(1 - \frac{\Delta h}{r_w}\right)^4, \tag{2.11}$$

where Δh is the distance from the fluid particle to the wall, C_k is adaptive shear force coefficient, which is calculated as $C_{k+1} = C_k + \alpha \Delta v_t$; α_r is a relaxation parameter, which can be calculated adaptively including previous flow behavior, or be a constant.

Adaptive shear force operates several iteration steps and converges to $\Delta v_t = 0$ and $f_t^k = \text{const}$.

Lees-Edwards boundary conditions To investigate the diffusion behavior in unconfined shear flow we used Lees-Edwards boundary conditions [58]. A box without walls is considered so that every particle which escapes the box from the left will appear at the right, and vice-versa; same for bottom and top. With simple shear applied, an escaping particle will change it velocity with changing sides (Fig. 2.3). The particle moving from the bottom to the top will appear at the same place at the bottom of the upper periodic box, e.i shifted to the left upper side of the dotted box. The upper and lower rows of

boxes move in opposite directions with velocity u_x . Because there are no walls, Lees-Edwards condition eliminates the lift force effect, hence it is possible to measure effective diffusion in shear flow.

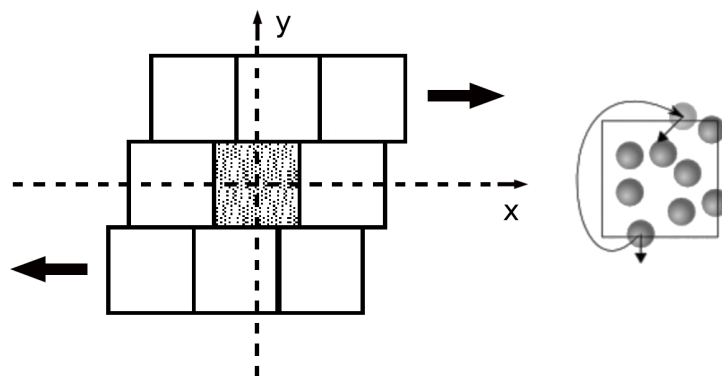


Figure 2.3.: Lees-Edwards boundary conditions. The upper and lower rows of boxes move in opposite directions. The actual simulation box is dotted, while the white ones are for explanation clarity. On the right side figure depicts how the cell will be inserted under the conditions.

3. Blood simulation

Blood consists mainly of plasma and RBCs by volume. Thus, a good approximation for blood flow simulation can include only fluid and RBCs. Blood flow in large channels can be approximated with a continuous model, while in small channels with diameters about $0.5D_{RBC} < D_{ch} < 10D_{RBC}$ we have to model RBCs explicitly.

3.1. Cell model

RBC models are often based on a membrane approach. A RBC is modeled as a closed membrane with elastic and bending potential, area and volume conservation constrains, to mimic elastic and viscous properties of the cell properly. There are two types of RBC models: discrete and continuous Ref. [19, 33, 63, 82]. In a continuous model RBC membrane is described by a set of equations, which are then discretized Ref. [33, 63]. We use model from Ref. [26] for 3D simulations.

3.1.1. 2D RBC model

In 2D, RBCs are modeled as closed bead-spring chains, which incorporate bending rigidity and an area constraint. 2D model of the cells is a closed bead-spring chain (Fig. 3.1). Every vertex pair has spring potential:

$$U_{sp} = \sum_{j \in 1 \dots N_s} \left[\frac{k_B T l_m (3x_j^2 - 2x_j^3)}{4p(1 - x_j)} + \frac{k_p}{l_j} \right], \quad (3.1)$$

where l_j is the length of the j -th spring, l_m is the maximum spring extension, $x_j = l_j/l_m$, p is the persistence length, and k_p is the spring constant. With such spring definition we can define a nonzero equilibrium spring length l_0 . The

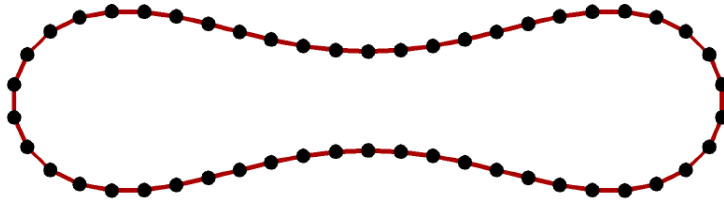


Figure 3.1.: 2D RBC model as a closed beads-spring chain. The chain has bending rigidity and total area conservation.

bending potential of a membrane is modeled as:

$$U_{bend} = \sum_{j \in 1 \dots N_s} k_b [1 - \cos(\theta_j)], \quad (3.2)$$

for two neighboring springs with an angle θ_j between them, and k_b is the bending constant. The cell area constraint is modeled as:

$$U_{area} = k_a \frac{(A - A_0)^2}{2}, \quad (3.3)$$

with the area constant k_a . A denotes instantaneous area, while A_0 is a desired area.

3.1.2. 3D RBC model

As a thrifty approach to simulate a 3D RBCs, the low-dimensional RBC model was introduced by [80]. The model consists of several colloidal particles simulated via DPD particles, connected with worm-like chain to each other combined with bending resistance (Fig. 3.2). The model captures the essential mechanical properties of RBCs and allows to cut the computational costs. Although, the computational costs and the simplicity are essential, with this it is not possible to reproduce a complex RBC-membrane dynamics like TT or wrinkling [108].

In our simulations we used another method to model RBCs - triangulated spring-network model [18, 26, 27, 77]. Each RBC is constructed by a collection of N_v particles linked by $N_s = 3(N_v - 2)$ springs with the potential (3.1). The bending rigidity of a membrane is modeled as in 2D (3.2). Finally, to mimic

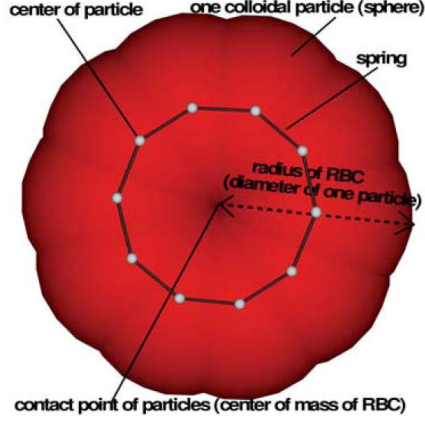


Figure 3.2.: A low-dimensional RBC model constructed from several colloidal particles. Ref [80].

area-incompressibility of the lipid bilayer and incompressibility of the inner cytosol, we use two constraints with the potentials given by

$$\begin{aligned}
 U_{area} &= k_a \frac{(A - A_r)^2}{2A_r} + \sum_j k_d \frac{(A_j - A_j^0)^2}{2A_j^0}, \\
 U_{vol} &= k_v \frac{(V - V_r)^2}{2V_r},
 \end{aligned} \tag{3.4}$$

where k_a , k_d , and k_v are the global area, local area, and volume constraint coefficients, respectively. A and V are the instantaneous RBC area and volume, while A_j is the instantaneous area of an individual triangle in a triangulated network. A_r , A_j^0 , and V_r are the desired total RBC area, area of the j -th face (set according to the initial triangulation), and total RBC volume, respectively.

The RBC model parameters (e.g., p , k_p , k_b) can be related to macroscopic membrane properties (e.g., shear, Young's, and bending moduli) through a linear analysis for a regular hexagonal network [26, 27]. For instance, the membrane shear modulus is given by

$$\mu_0 = \frac{\sqrt{3}k_B T}{4pl_m x_0} \left(\frac{x_0}{2(1-x_0)^3} - \frac{1}{4(1-x_0)^2} + \frac{1}{4} \right) + \frac{3\sqrt{3}k_p}{4l_0^3}, \tag{3.5}$$

where $x_0 = l_0/l_m$. The corresponding area-compression K and Young's Y moduli can be found as $K = 2\mu_0 + k_a + k_d$ and $Y = 4K\mu_0/(K + \mu_0)$. The

3. Blood simulation

bending coefficient k_b in Eq. (3.2) can be expressed in terms of the macroscopic bending rigidity κ of the Helfrich model [46] as $k_b = 2\kappa/\sqrt{3}$. The coefficients k_a , k_d , and k_v can be selected large enough to approximate properly area-incompressibility of the lipid bilayer and incompressibility of the inner cytosol. Thus, the necessary model parameters are calculated directly from desired macroscopic RBC properties. In addition, we also employ a “stress-free” model of a RBC obtained by computational annealing such that equilibrium length l_0^i for each spring is set to the corresponding edge length within initial membrane triangulation [26, 27]. This also implies that $l_m^i = l_0^i \times x_0$ is set individually with $x_0 = 2.2$, see Refs. [26, 27] for more details.

To describe RBC properties, we define an effective RBC diameter as $D_r = \sqrt{A_r/\pi}$. The average effective diameter for a healthy RBC is equal to $D_r = 6.5 \mu\text{m}$ [23]. Table 3.1 outlines RBC parameters for simulations in units of D_r and $k_B T$, and the corresponding average values for a healthy RBC in physical units.

Coupling between RBCs and the fluid flow is done through viscous friction [26] between cell vertices and the surrounding fluid particles. The coupling is implemented via dissipative particle dynamics interactions [22, 49] using dissipative and random forces similar to F^D and F^R from Eq. 2.1. The strength γ of the dissipative force is adjusted to satisfy no-slip boundary conditions at a membrane. Using an approximation of linear shear flow near the membrane, the coefficient γ can be expressed in terms of fluid density n , interaction cutoff radius r'_c , number density of membrane particles n_m , and fluid viscosity η [26]. This formulation results in satisfaction of the no-slip BCs for the linear shear flow over a flat membrane; however, it also serves as an excellent approximation for no-slip at the membrane surface. Note that conservative interactions between fluid and membrane particles are turned off, which implies that the radial distribution function is structureless, i.e. $g(r) = 1$.

3.1.3. Membrane surface triangulation

The shape of a RBC resembles a deflated sphere, and it is one of the way to get the biconcave shape for simulations. Moreover, this shape corresponds to the minimum of bending energy. The shape of a RBC can be described analytically

RBC parameters	scaled units	physical units
N_v	500	
A_r		$133.5 \times 10^{-12} \text{ m}^2$
D_r	$\sqrt{A_r/\pi}$	$6.5 \times 10^{-6} \text{ m}$
V_r	$0.34 D_r^3$	$93 \times 10^{-18} \text{ m}^3$
T		310 K
Y_r	$1.82 \times 10^5 \frac{k_B T}{D_r^2}$	$18.9 \times 10^{-6} \text{ N/m}$
κ_r	$70 k_B T$	$3 \times 10^{-19} \text{ J}$
k_d	$4.2 \times 10^4 \frac{k_B T}{D_r^2}$	$4.3 \times 10^{-6} \text{ N/m}$
k_a	$2.1 \times 10^6 \frac{k_B T}{D_r^2}$	$2.1 \times 10^{-4} \text{ N/m}$
k_v	$1.4 \times 10^7 \frac{k_B T}{D_r^3}$	220 N/m^2

Table 3.1.: RBC characteristics in units of the effective RBC diameter D_r and $k_B T$, and the corresponding average values for a healthy RBC in physical units. N_v is the number of membrane vertices, A_r is the RBC membrane area, V_r is the RBC volume, T is the temperature, Y_r is the membrane Young's modulus, κ_r is the membrane bending rigidity, and k_d , k_a , and k_v are the local area, global area, and volume constraint coefficients, respectively. In all simulations, we have chosen $A_r = 133.5$ and $k_B T = 0.4$, which implies that $D_r = 6.5$.

in Cartesian coordinates as [23, 25]:

$$z = \pm D_0 \sqrt{1 - \frac{x^2 + y^2}{D_0^2}} \left[c_0 + c_1 \frac{x^2 + y^2}{D_0^2} + c_2 \frac{(x^2 + y^2)^2}{D_0^4} \right], \quad (3.6)$$

where D_0 is the cell diameter, $c_0 = 0.1035805$, $c_1 = 1.001279$ and $c_2 = -0.561381$.

To obtain a nearly regular triangulation, point charges on the sphere surface are considered. The electrostatic problem is solved with point charges ‘‘attached’’ to the sphere surface. After the equilibrium is reached, the surface is triangulated.

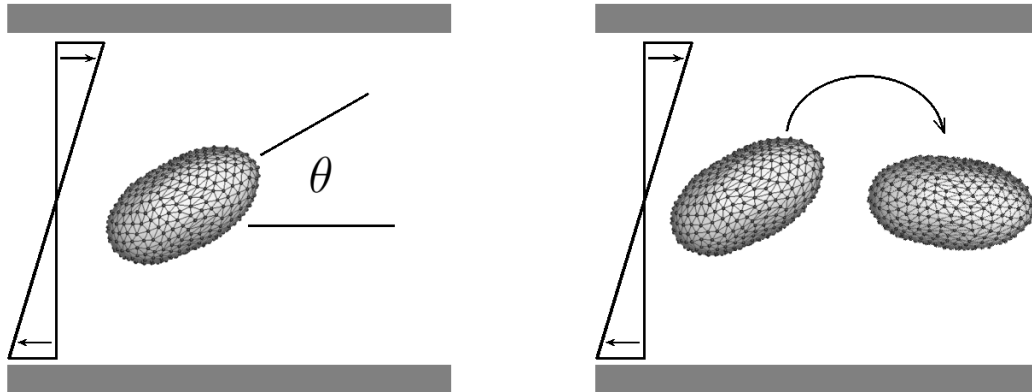


Figure 3.3.: Left: Tank treading motion of a vesicle in a shear flow; Right: Tumbling motion of a vesicle Ref. [73].

3.2. RBC dynamics

RBC dynamics in flow can affect cardiovascular system. Every distinct motion of RBCs results in a different resistance of the system. Thus, the knowledge about these motions can help us to construct better microfluidic devices to separate RBC based on their properties.

3.2.1. Particle dynamics in shear flow

As it was mentioned already, RBC dynamics in shear flow can be tank-treading (*TT*), tumbling (*TB*) or swinging (*SW*) depending on viscosity contrast (λ) between inner and outer fluids, membrane viscosity and shear rate. *TT* dynamics is a motion of a vesicle membrane when it has a constant inclination angle θ with flow direction, while inner fluid and membrane are moving around COM of the cell like a tank tread or treadmill (Fig. 3.3 left).

TB dynamics is a motion of the cell when it rotates as a rigid body around its COM (Fig. 3.3 right). *SW* dynamics is an “intermediate” motion between *TT* and *TB* motions, when the vesicle is in *TT* motion and oscillates around its COM, so that inclination angle θ changes with a certain periodicity.

Flexible particles undergo elongation and torque in shear flow. The former tries to align a vesicle with the inclination angle $\theta = \pi/4$. When the shear stresses between the membrane and inner fluid go over some threshold, the inclination angle decreases and the vesicle starts moving in a *TB* manner. If

the shear stresses are not high enough, it moves in SW way.

In 1982 Keller and Skalak (KS) [55] developed a theory, which predicts TT and TB motion of an ellipsoidal vesicle in flow. KS theory can predict the inclination angle of a vesicle in TT motion. For more details see Appendix A.1.

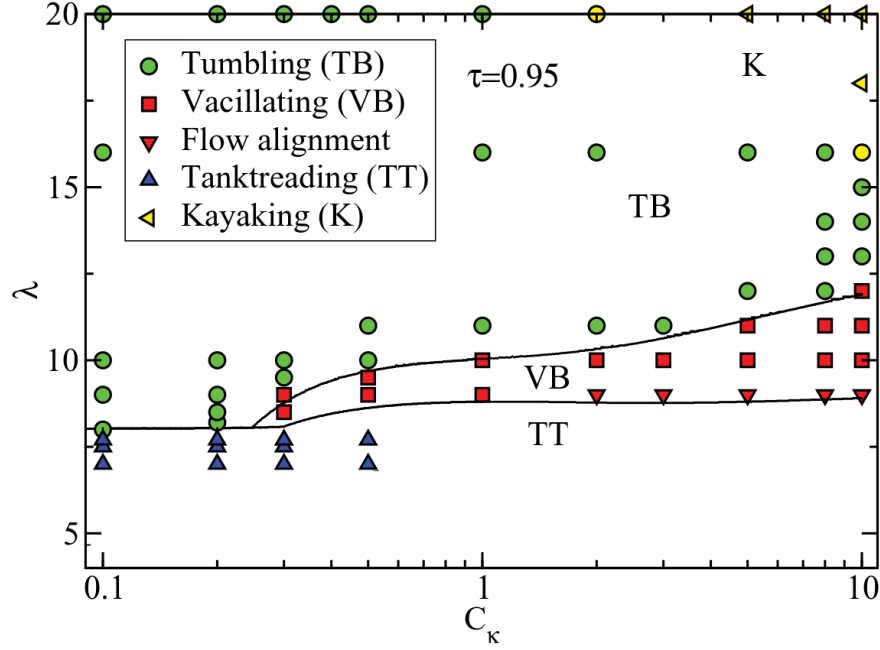


Figure 3.4.: RBC dynamics in flow from [104]. VB here is SW motion. $C_k = \bar{\gamma}\tau$, where τ is the characteristic relaxation time of the vesicle.

An ellipsoidal RBC with $\lambda < 3$ undergoes TB motion at low shear rates. Increase of shear rate changes the motion to TT, with small region between, where the ellipsoidal RBC has an unstable TT-to-TB transition motion. When $\lambda > 3$ stable TT motion is not observed, and RBC undergoes the TB mode. Healthy RBCs have $\lambda > 3$, and TT motion shows SW with a stable frequency and amplitude (Fig. 3.4), but not for physiological values. Here, one can also see "Kayaking" motion, when the main axis of the vesicle describes a cone oriented perpendicular to the plane of shear flow.

Experiments show, that a single RBC subjected to TT for hours, relaxes to its biconcave shape with the same relative positions of beads fixed at the membrane. This indicates the existence of energy barrier for RBC to start TT from TB [36].

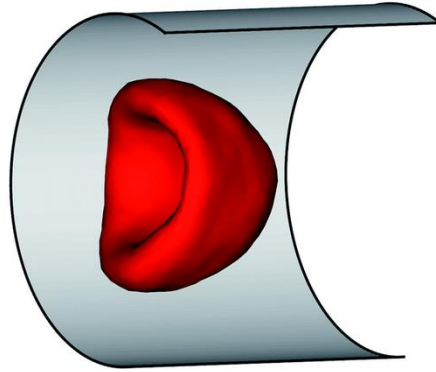


Figure 3.5.: RBC parachute shape in Poiseuille flow with $D = 9\mu m$.

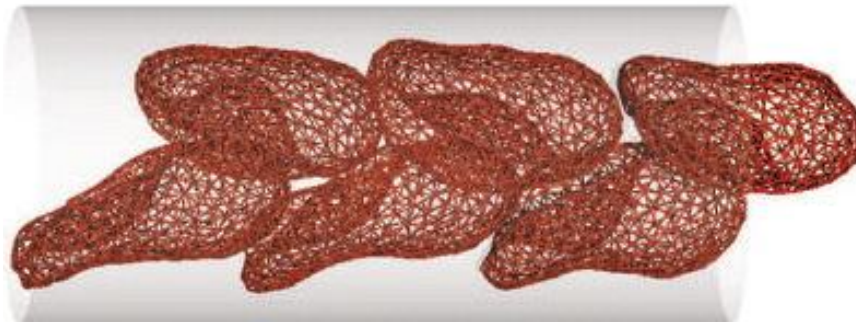


Figure 3.6.: RBC in zigzag-slipper shape from [67].

3.2.2. RBC dynamics in Poiseuille flow

Experiments show, that RBCs can change their biconcave shape to a parachute shape in Poiseuille flow in channels with diameters close to D_{RBC} [24, 107]. This shape is also found numerically [35] (Fig. 3.5).

At low flow velocities, a RBC resembles the biconcave shape and with increasing velocity it transits to parachute-like shape. Transition from the biconcave to parachute shape can be investigated by means of the gyration tensor of a RBC. Since the RBC elongates at the parachute state, the smallest eigen-vectors increases in comparison with that in biconcave shape [67].

Also, there is a zigzag-slipper shape (Fig. 3.6), when every RBC in flow takes so called slipper shape. The slipper shape is inclined with respect to flow stream. At high enough concentrations, they construct a zigzag pattern during flow.

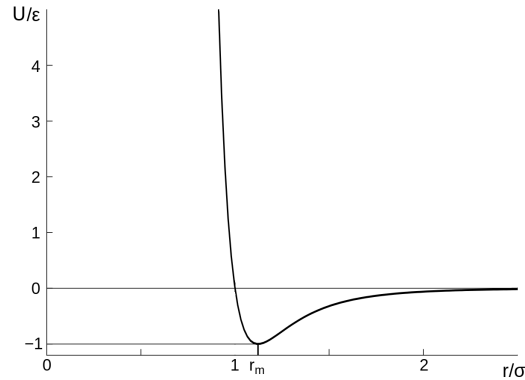


Figure 3.7.: LJ potential as a function of distance

3.3. Blood flow simulations

The rheology of whole blood in a channel is dependent of dynamics of single RBCs. Different dynamics of single RBCs changes the properties of blood. Here, we present a common setup for $2D$ and $3D$, and describe the main properties of the blood flow.

3.3.1. RBC interactions

To eliminate overlapping of RBCs under flow, the Lennard-Jones (LJ) repulsive interactions and bounce-back reflections on the cell membrane have been used. The LJ potential is given by:

$$U_{LJ}(r) = 4\epsilon \left(\left(\frac{\sigma_{LJ}}{r} \right)^{12} - \left(\frac{\sigma_{LJ}}{r} \right)^6 \right) \quad (3.7)$$

with the cut-off at the minimum of the potential, so that $r_{max} = 2^{1/6}\sigma_{LJ}$ (Fig. 3.7).

Bounce-back reflections are applied to every particle on a cell, neighboring with other RBC membranes. Fluid particles are reflected at boundaries and cell membranes, while cell particles are reflected at other cells membranes and solid boundaries. Finally, boundaries are frozen and do not move.

3.3.2. RBC distribution in flow

Typically, straight channels with diameters in the range $0.5D_{RBC} < D_{ch} < 10D_{RBC}$ and lengths of about $5D_{RBC} < L < 20D_{RBC}$ are used in both $2D$ and $3D$ simulations. The length should be taken long enough to prevent RBCs to feel their image through periodical boundary conditions.

The flow in the channel is driven by a volume force, applied to every fluid particle. No-slip boundary conditions and the force lead to the Poiseuille flow with parabolic velocity profile and maximum velocity at the center:

$$V_{max} = \frac{\Delta p D^2}{16L\eta} \quad (3.8)$$

and radial velocity distribution:

$$v(r) = V_0 \left(1 - 4r^2/D^2\right) \quad (3.9)$$

where Δp is the pressure drop and η is dynamic viscosity. The volume force f is connected to the applied pressure drop through $fn = \Delta p/L$, with fluid number density n . For $2D$ the maximum velocity is $V_{max} = \frac{\Delta p D^2}{8L\eta}$. Although, the blood has pulsatile motion within large arteries, in small arterioles, venules and micro-capillaries it becomes nearly steady.

Dimensionless shear rate $\dot{\gamma}^*$ is used to connect simulation results with experimental observations. This parameter is obtained by multiplying the shear rate with a typical RBC membrane relaxation time or from Re number:

$$\begin{aligned} \dot{\gamma}^* &= \bar{\gamma} \tau_{RBC} = \bar{\gamma} \frac{\eta D_r^3}{k_r} \\ \dot{\gamma}^* &= \frac{\bar{\gamma} n D_r^2}{\eta Re} \end{aligned} \quad (3.10)$$

with $\bar{\gamma} = \bar{v}/D$, k_r is membrane bending rigidity and D_r is the RBC diameter.

Under healthy conditions blood velocity for arterioles is in the range $1.0 - 31.7 \text{ mm/s}^{-1}$, and $0.5 - 11 \text{ mm/s}^{-1}$ for venules both with diameters about $20 \text{ }\mu\text{m}$ [9].

Even though, the Poiseuille flow has a parabolic velocity profile, the blood flow profile is different and has a lower maximum velocity and lower local slopes

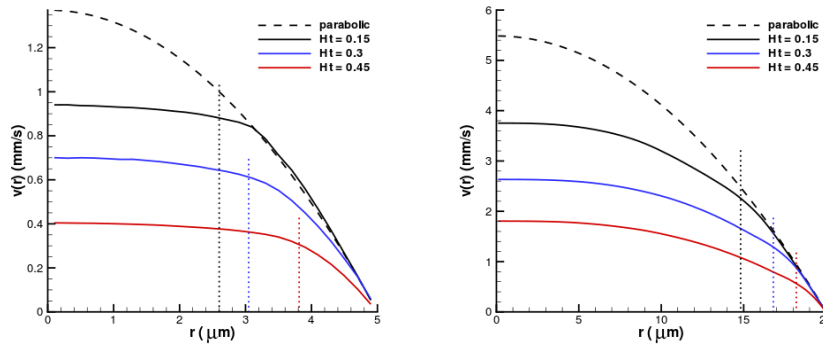


Figure 3.8.: Blood flow profile under different conditions in Poiseuille flow from Ref. [25]. Dashed lines show parabolic Poiseuille profile. Dotted lines depict CFL thickness for different cases.

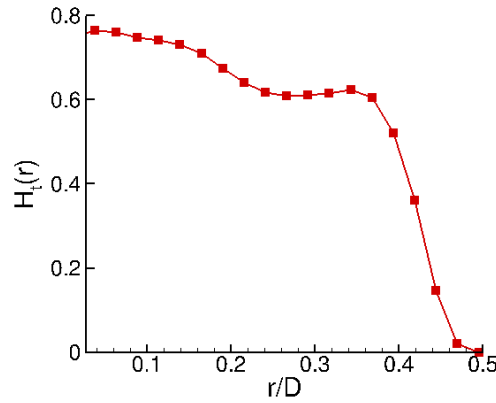


Figure 3.9.: Hematocrit value (H_t) across the channel. Zero r/D corresponds to the channel center. Hematocrit decays to zero close to the walls, so there are no RBCs at the near-wall region.

(Fig. 3.8). Dashed lines correspond to the parabolic flow of the blood plasma without RBCs. RBCs distribution across the channel shows the reason of the blood flow profile (Fig. 3.9).

The number of RBCs close to the wall practically zero, so near-wall hematocrit drops. As a result RBCs the form bulk of flow in the center are moving together away from the walls. Blood plasma plays a “lubricant role”, allowing the RBC core to flow at the center. The central arrangement of RBCs is the reason for the blood flow velocity distribution behavior in the Fig. 3.8.

Fahreus discovered an effect, which is connected with the blood-flow behavior [37]. He performed experiments with blood in glass tubes and noticed that

3. Blood simulation

the discharge hematocrit (H_d) is higher than the hematocrit in the tank which feeds the tube. H_d is the volume fraction of RBCs in blood exiting the tube per unit time. Therefore, RBC-core flow velocity is higher than an average blood velocity. After a number of experiments an empirical expression was suggested by Pries et al. [90] to relate H_t and H_d :

$$\frac{H_t}{H_d} = H_d + (1 - H_d) (1 + 1.7e^{-0.415D} - 0.6e^{-0.011D}) \quad (3.11)$$

where the tube diameter D should be in μm .

The ‘‘lubricant’’ plasma layer void of RBCs is called *RBC free layer* or just *cell free layer (CFL)*. The thickness of the CFL plays an important role in blood flow resistance and volumetric blood-flow rate. CFL also explains another effect, discovered by Fahreus and Lindquist in 1931 [38]. Their experimental results have shown, that apparent blood viscosity increases with increasing channel diameter.

$$\eta_{app} = \frac{\Delta p D^2}{32 \bar{v} L} \quad (3.12)$$

In over words, introducing a relative viscosity $\eta_{rel} = \eta_{app}/\eta_{pl}$ with η_{pl} being the plasma viscosity: the relative viscosity increases with increasing the channel diameter. The blood viscosity depends highly on H_t because of RBC-core of flow: the more RBCs are in the channel, the less plasma layer stays for lubrication. Moreover, RBC inner fluid viscosity under healthy conditions is about 5 times higher than plasma’s.

3.3.3. Cell-free layer

CFL, as mentioned above, is a domain at the near-wall region void of RBCs. Although it is called cell-free, there might be some other cells or particles [72]. Here we use this term explicitly for RBCs. CFL can be found not only in Poiseuille flow, but also in simple shear flow.

CFL strongly depends on channel diameter, because RBCs pack in the center. However, the ‘‘lubricant’’ layer becomes negligible for $D > 200 \mu m$ where the blood flow is very close to the parabolic Poiseuille flow [29]. In *in vivo* results can be different from in *in vitro* and simulated results because of a glycocalyx layer at vessel walls. This is the layer, which coats the vessel wall from inside. It is

estimated to be on the order of $0.4 - 0.5 \mu m$ [15, 109]. Also, glycocalyx covers some bacterial epithelia and other cells.

Moreover, shear rate affects the CFL but not so dramatically as D . There is almost no CFL for $\dot{\gamma}^* < 1$, but as the shear rate increases the CFL thickness grows until a certain value and then levels off.

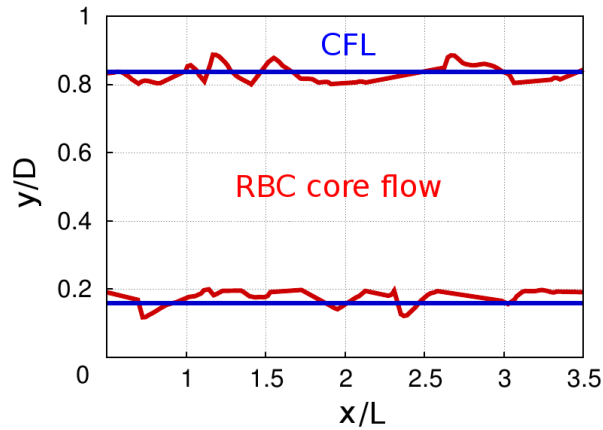


Figure 3.10.: CFL measurement in simulations. The straight line corresponds to an averaged CFL value, the curved lines display the edge of the RBC-core.

The CFL thickness can be measured with a high-speed camera and a microscope in *in vivo* and in *in vitro* once the flow is converged. Calculation of the CFL in simulations is based on the simulation snapshots. The RBC-core flow is projected onto a plane, such that we can see the RBCs part and the plasma part near a wall (Fig. 3.10). The edge of the RBC-core is considered to be CFL. The distance between the edge and the wall is averaged along and around the channel with different angular orientations. In case of large gaps between RBCs in one snapshot, the gap part of the edge is continuously connected, to avoid the overestimation of the CFL.

Microvascular branches and junctions distort RBC distribution across the channel. This may destroy the converged CFL or make it non-symmetric when the RBC-core is closer to one side of the wall [20, 51]. This can increase the flow resistance due to a thinner CFL. However, after some distance (several channel diameters), the CFL will become symmetric again.

3.3.4. RBC interactions. Morse potential

Blood exhibits aggregation behavior, when RBCs form a rouleaux structure, which is similar to a stack of coins (Fig. 1.8). Under low shear rates RBCs are attracted to each other. There exist two hypotheses for RBCs aggregation. One hypothesis assumes that there is proteins in plasma, which may bridge erythrocytes together. Another proposition is based on the idea of depletion interactions.

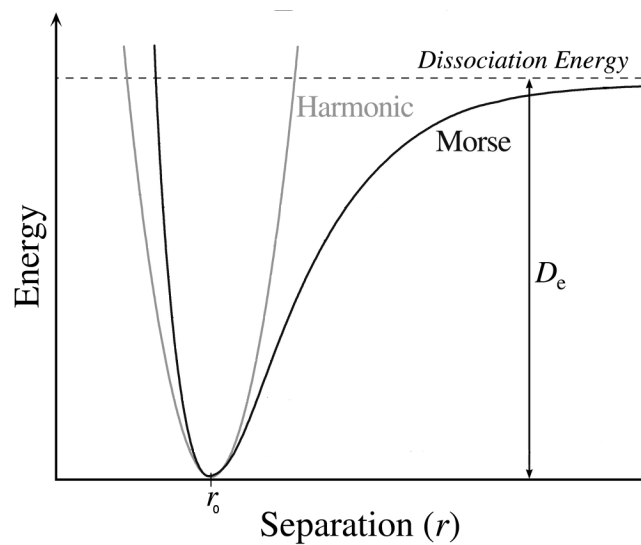


Figure 3.11.: Comparison of Morse and harmonic potentials. D_e is the dissociation energy, r_0 is the equilibrium bond distance.

In our simulations with RBCs aggregation, we use Morse potential. The potential increases faster than LJ. The potential has short-range repulsive and long-range attractive interactions.

These aggregation forces are approximated by the Morse potential $U(r) = D_e[e^{2\beta(r_0-r)} - 2e^{\beta(r_0-r)}]$, where r is the separation distance, r_0 is the zero force distance, D_e is the well depth of the potential, and β characterizes the interaction range. The potential showed quite good agreement with experiments [34].

4. Microvascular blood flow resistance: role of red blood cell migration and dispersion

4.1. Introduction

Flow resistance of a full cardiovascular system is mainly attributed to the resistance of blood flow within microvasculature or microcirculation [61, 81, 87, 100], which is comprised of the smallest vessels (e.g., arterioles, capillaries, venules) with diameters up to about 100 μm . In particular, the the knowledge about bulk blood properties is far from sufficient to predict the behavior of blood and its flow resistance in microcirculation. For instance, experimental measurements [61, 86, 91] of blood flow resistance *in vivo* have shown that it may be several time larger than that in *in vitro* experiments on blood flow in glass tubes [85, 96]. Several potential contributions to an increased blood flow resistance *in vivo* have been suggested. These include vessel irregularities, bifurcations, and junctions, which may affect the distribution of red blood cells (RBCs) in a vessel cross-section [83, 91, 99], the presence of endothelial surface layer (or glycocalyx) [109, 111] at the vessel walls [86, 92], and the length of vessel sections between bifurcations and junctions [81, 88].

The endothelial surface layer resembles a polymeric brush at a vessel wall with an estimated thickness of about 0.5 – 1.5 μm [89, 113]. Its effect on an increased flow resistance can be interpreted as an effective reduction of the vessel diameter due to the glycocalyx, and a large enough thickness of this layer ($\sim 2 \mu\text{m}$) provides a plausible explanation for the discrepancy of experimentally measured blood flow resistances *in vivo* and *in vitro* [86, 92].

However, contribution of the other effects have not been rigorously studied. As an example, RBCs in microvessels migrate away from the walls leading to a layer near a wall void of RBCs [11, 43]. This layer is called cell-free layer (CFL) or RBC-free layer, and its thickness is directly associated with the blood flow resistance [28, 81, 96]. In the microvasculature, blood flow and in particular the distribution of RBCs in a vessel cross-section can be significantly disturbed at bifurcations and junctions resulting in a reduced CFL thickness and an increased flow resistance. After the RBC distribution is distorted at a vessel bifurcation, in the following vessel segment RBCs will migrate toward the vessel center leading to a dynamic development and recovery of the CFL thickness. Thus, the flow resistance in microcirculation is affected by the degree of RBC dispersion at vessel junctions and the length of the CFL recovery after the distortion in comparison to a characteristic length of vessel segments between bifurcations in microvascular networks.

RBC migration and the development of CFL are governed by hydrodynamic interactions of RBCs with channel walls [2, 7, 13] and cell-cell interactions or collisions in flow [45, 57]. The former RBC-wall interaction is usually referred to as a lift force [2, 7, 13, 68], while the latter one is called shear-induced diffusion or shear-induced normal stress [45, 60]. The lift force drives RBCs away from the vessel walls, while the cell-cell interactions lead to an effective dispersion of RBCs. The balance between these two contributions at steady flow results in a converged thickness of the RBC flow core and CFL. Clearly, the CFL development and its final thickness are functions of a number of parameters including hematocrit (volume fraction of RBCs), flow rate, vessel diameter, and aggregation interactions between RBCs.

The main focus of this research is a systematic investigation of CFL development in microvessels for a number of blood flow conditions using mesoscopic simulations [29, 33]. We use the smoothed dissipative particle dynamics method [21] to study the development of blood flow for various flow conditions starting from a fully-dispersed configuration of RBCs. Following the migration of RBCs away from the walls, the CFL thickness is dynamically monitored until it converges to a constant value of a fully-developed flow. The time evolution of CFL thickness appears to be nearly universal with respect to flow rate for physiological hematocrits $H_t \leq 0.45$; this range of hematocrits is also directly

relevant for healthy microcirculatory blood flow [61, 84]. This allows us to define a length l_c for the development of CFL, which is nearly independent of the flow rate and equal to approximately $25D$, with the vessel diameter D . Thus, the effect of RBC dispersion at vessel bifurcations and junctions on the flow resistance may be significant in vessels which are shorter or comparable to the length l_c , while in longer vessel sections it can be practically neglected. Aggregation interactions between RBCs result in a reduction of blood flow resistance, since they aid to maintain a more compact RBC flow core.

Finally, we also develop a simple theoretical model which describes well the final CFL thickness when the flow has converged. The model considers the balance between a lift force on RBCs due to cell-wall hydrodynamic interactions and shear-induced effective pressure due to cell-cell interactions in flow. This model supports the idea that these are the two main mechanisms which govern the final CFL thickness. Similar ideas have also been applied to describe dispersion of RBCs after injection [45]. We hope that our results will help to better understand also the flow behavior of other suspensions of deformable particles such as vesicles, capsules, and cells, and will trigger new investigations in this area.

4.2. Models & Methods

We employ the smoothed dissipative particle dynamics (SDPD) method [21] to model fluid flow. SDPD is a mesoscopic simulation technique, where each SDPD particle corresponds to a small volume of fluid instead of individual atoms or molecules. The RBC membrane is represented by a triangulated network model [18, 26, 27, 77] and coupled to fluid flow using friction forces.

4.2.1. SDPD model

Table 4.1 presents the fluid simulation parameters in units of the fluid particle mass m , the cutoff radius r_c , and the thermal energy $k_B T$. Even though SDPD allows one to directly input desired fluid viscosity η_0 , the measured dynamic viscosity η of SDPD fluid might be slightly different. The assumption that $\eta = \eta_0$ is reliable only if each SDPD particle has a large enough number of

4. Microvascular blood flow resistance: role of red blood cell migration and dispersion

$\frac{p_0 r_c^3}{k_B T}$	$\rho_0 r_c^3$	α	$\frac{b r_c^3}{k_B T}$	$\frac{\eta_0 r_c^2}{\sqrt{m k_B T}}$	$n r_c^3$	$\frac{\eta r_c^2}{\sqrt{m k_B T}}$
675	10.125	7	675	266.8	10.125	284.6

Table 4.1.: SDPD fluid parameters used in simulations. Mass, length, and energy for SDPD fluid are measured in units of the fluid particle mass m , the cutoff radius r_c , and the thermal energy $k_B T$, respectively. p_0 , ρ_0 , b , and α are parameters for the pressure equation, n is the number density of fluid particles, and η_0 and η are the desired and measured dynamic viscosities of the SDPD fluid. In all simulations, we have set $m = 1$, $r_c = 1.5$, and $k_B T = 0.4$.

neighboring particles, which may require large enough r_c and/or density of fluid particles n . Consequently, we advise to always check validity of the approximation directly using a shear flow simulation. For instance, SDPD fluid with the parameters in Table 4.1 yields slightly larger fluid viscosity measured in a shear flow setup than η_0 .

4.2.2. RBC model

For the simulations we used a triangulated spring-network RBC model [18, 26, 27, 77]. Each RBC consists from a collection of 500 particles linked by $N_s = 1494$ springs, with area and volume conservations and dihedral potential.

4.2.3. RBC aggregation model

For blood, the attractive cell-cell interactions are crucial to represent aggregation of RBCs. These forces are approximated by the Morse potential described in Subsection 3.3.4. The Morse potential parameters were chosen as $\beta = 1.5 \mu\text{m}^{-1}$, $r_0 = 0.3 \mu\text{m}$, $D_e = 0.3 k_B T$ and showed quite good correspondence with experiments [34].

4.2.4. Cell-free layer

Cell-free layer (CFL) is a fluid layer close to the channel wall void of RBCs. In Poiseuille flow, CFL forms due to a hydrodynamically-induced lift force on RBCs close to a wall [2, 7, 68] leading to their migration toward the tube center and leaving a near-wall fluid layer free of RBCs. Fluid viscosity in the

CFL region is similar to that of plasma, whose viscosity is considerably lower than the effective viscosity in the tube center populated by RBCs. Thus, a CFL serves as an effective “lubrication” layer for the RBC core to flow and its thickness is directly associated with the resistance of blood flow.

4.2.5. Simulation setup

The simulation setup contains a single periodic cylindrical channel with a diameter $D = 20 \mu\text{m}$ or $40 \mu\text{m}$ and the length of $L = 60 \mu\text{m}$. The channel is filled with fluid particles and suspended RBCs. The average plasma viscosity under healthy conditions is assumed to be $\eta = 0.0012 \text{ Pa} \cdot \text{s}$. For simplicity, the fluid viscosity inside a RBC is set to be the same as that of blood plasma. However, we also provided simulations with viscosity contrast 5, where RBC inner fluid (cytoplasm) has viscosity 5 times higher, than outer fluid (plasma). The flow is driven by a constant force f applied to each solvent particle, which is equivalent to a constant pressure gradient $\Delta P/L = fn$, where ΔP is the pressure drop and n is the number density of solvent particles. To characterize the flow we define an average (or pseudo) shear rate $\bar{\dot{\gamma}}$ as

$$\bar{\dot{\gamma}} = \bar{v}/D, \quad (4.1)$$

where $\bar{v} = Q/A$ is the average flow velocity with a volumetric flow rate Q through a cross-sectional area $A = \pi D^2/4$.

Before the start of flow, RBCs are distributed almost randomly in the tube as shown in Fig.4.1(a). This distribution is achieved by running a simulation without a flow for some time, which allows RBCs to diffuse and reach their equilibrium distribution. After that the flow is started and the development of CFL is measured in time as RBCs migrate away from the wall. For comparison Fig.4.1(b) illustrates the distribution of RBCs for $D = 40 \mu\text{m}$, $H_t = 0.3$, and $\bar{\dot{\gamma}} = 298 \text{ s}^{-1}$ after the blood flow has been fully developed. Clearly, RBCs have migrated toward the channel center yielding a CFL near the wall.

4. Microvascular blood flow resistance: role of red blood cell migration and dispersion

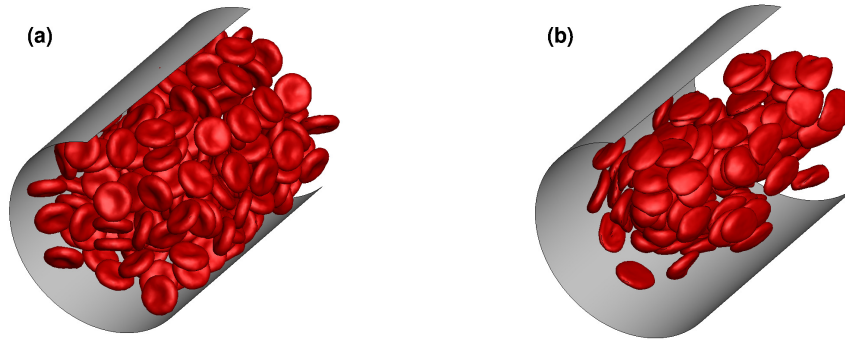


Figure 4.1.: Simulation snapshots for $D = 40 \mu\text{m}$ and $H_t = 0.3$. (a) Before the flow is applied, RBCs are distributed nearly randomly in the tube. (b) After the flow has converged for $\bar{\gamma} = 298 \text{ s}^{-1}$. The CFL region can be clearly seen.

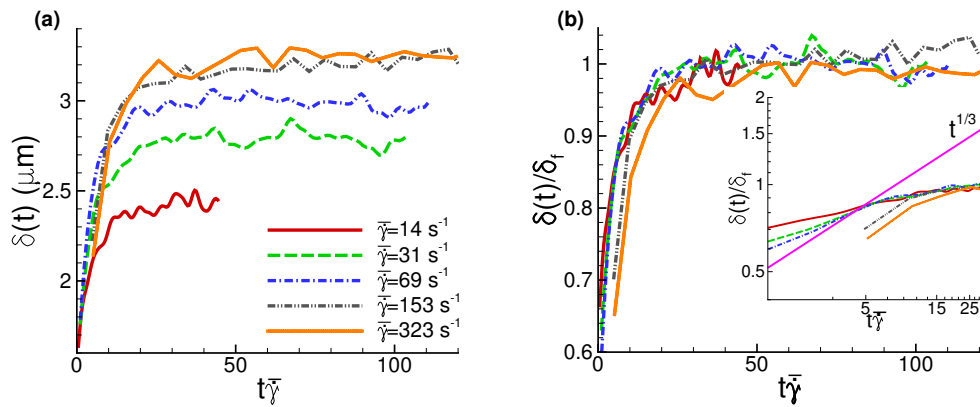


Figure 4.2.: Development of the CFL thickness in time after flow has been started for the case of $H_t = 0.3$ and $D = 20 \mu\text{m}$. The time is normalized by the pseudo-shear rate. (a) The CFL thickness evolution for different pseudo-shear rates. (b) The same set of data as in plot (a) with all curves normalized by the plateau value of the CFL thickness δ_f at large $\bar{\gamma}$. The inset in (b) is a log-log plot illustrating a power-law behavior of the CFL curves at small $t\bar{\gamma}$.

4.3. Results

4.3.1. Cell-free layer evolution

We first investigate the development of the CFL in blood flow. Already in the absence of flow, a non-zero CFL thickness is measured due to the entropic repulsion (e.g., due to hindered rotational motion) between RBCs and the tube wall. In addition, since we consider relatively small vessel diameters, a non-zero wall curvature prevents RBCs from fully conforming with its cylindrical shape, which also results in a non-zero CFL thickness. After the flow is started, RBCs migrate away from the wall, and the development of the CFL is monitored in time. Figure 4.2(a) shows the evolution of the CFL thickness $\delta(t)$ for different driving forces (or pressure gradients) for the case of $H_t = 0.3$ and $D = 20 \mu\text{m}$. The time is normalized by the $\bar{\gamma}$ value of the fully-developed flow. The CFL curves show a rapid increase of the CFL thickness up to about $t\bar{\gamma} \approx 25$ followed by a plateau, which we will also refer to as a final CFL thickness δ_f . The values of δ_f are larger for higher flow rates; however, the growth is clearly limited by excluded-volume interactions between RBCs in the flow core and is expected to approach a constant value for large $\bar{\gamma}$.

Fig. 4.2(b) presents the same CFL curves with their plateau values scaled by δ_f . The scaled CFL curves appear to be similar indicating that the shear rate $\bar{\gamma}$ is the only relevant time scale here. Thus, the development of CFL for $H_t = 0.3$ is mainly governed by shear forces in flow. A similar conclusion can be drawn for low H_t supported by our simulation data for $H_t = 0.15$ (not shown here) and for higher H_t shown in Fig. 4.3. Some discrepancies between the curves in Figs. 4.2(b) and 4.3(b) for different shear rates indicate that there may exist a second relaxation time. The initial fast time scale is governed by $\bar{\gamma}$ and corresponds to RBC migration away from the wall as it was discussed before. The second time scale is related to cell-cell interactions in flow such that RBCs in the core of the flow have to re-arrange and reach a denser flow-induced packing. This time scale is slower than that for RBC migration, and appears to be more noticeable for larger H_t values. This process is also illustrated in Fig. 4.4 by the development of hematocrit profile for $H_t = 0.45$. While the initial shift of the local hematocrit curve away from the wall is rather rapid,

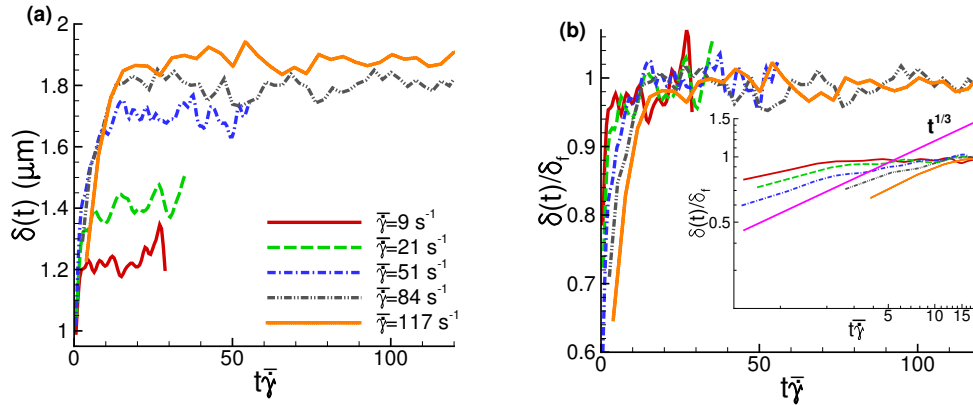


Figure 4.3.: Development of the CFL thickness in time after flow has been started for the case of $H_t = 0.45$ and $D = 20 \mu\text{m}$. The time is normalized by the pseudo-shear rate $\bar{\gamma}$. (a) The CFL thickness evolution for different pseudo-shear rates. (b) The same set of data as in plot (a) with all curves normalized by the plateau value of the CFL thickness δ_f . The inset in (b) is a log-log plot illustrating a power-law behavior of the CFL curves at small $t\bar{\gamma}$.

the further development of local RBC density in the bulk appears to be slower. However, the convergence of the CFL to δ_f is nearly independent of hematocrit ($H_t \leq 0.45$) and occurs within $t\bar{\gamma} \approx 25$.

To verify that the conclusions made so far do not change significantly for a different vessel diameter, we performed a number of simulations for $D = 40 \mu\text{m}$. The corresponding CFL dynamics is shown in Fig. 4.5 for different H_t values. The convergence of CFL thickness is reached by the time $t\bar{\gamma} \approx 25$, in agreement with the simulation data for $D = 20 \mu\text{m}$.

4.3.2. Effect viscosity contrast

RBCs are more likely to show a TB motion than TT , when the inner fluid is more viscous than the outer one. Tumbling RBC as a subject to a weaker lift force, than under tank-treading [68]. As a result, the CFL convergence under flow for a physiological viscosity contrast takes longer, than for RBCs with the viscosity contrast $\lambda = 1$. Results for the case where RBCs have a viscosity contrast $\lambda = 5$ are shown in Fig. 4.6(a).

The CFL becomes thicker in this case. On the other hand, simulations with separated inner and outer fluids of the same viscosity contrast still show thicker

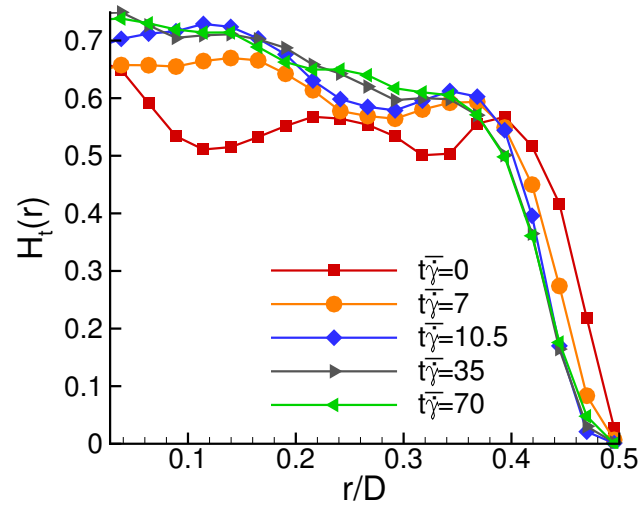


Figure 4.4.: Development of the hematocrit profile in time after flow has been started for the case of $H_t = 0.45$, $D = 20 \mu\text{m}$ and $\bar{\gamma} = 117 \text{ s}^{-1}$. Different lines correspond to different times.

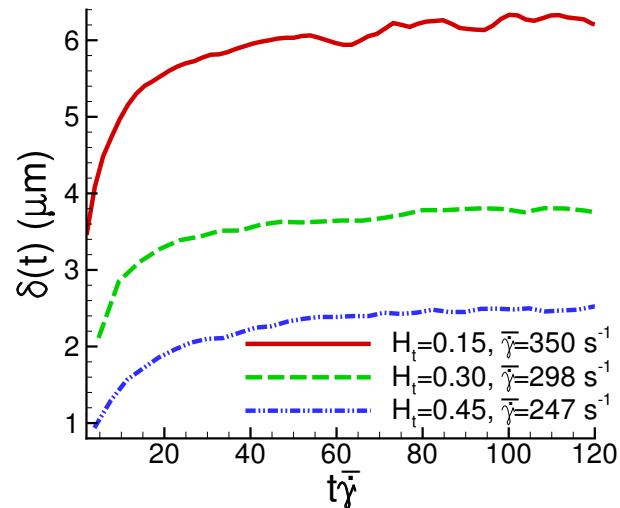


Figure 4.5.: Development of the CFL thickness in time after flow has been started for the case of $D = 40 \mu\text{m}$ and different H_t values. The time is normalized by the pseudo-shear rate $\bar{\gamma}$.

4. Microvascular blood flow resistance: role of red blood cell migration and dispersion

CFL for the TT motion rather than for TB motion. The result has a good physical explanation, because the lift force acts stronger on TT RBC, than TB one.

An another interesting observation is that after a rapid growth of the CFL, RBCs “packing” in the center takes longer than for the system with a viscosity contrast 1.

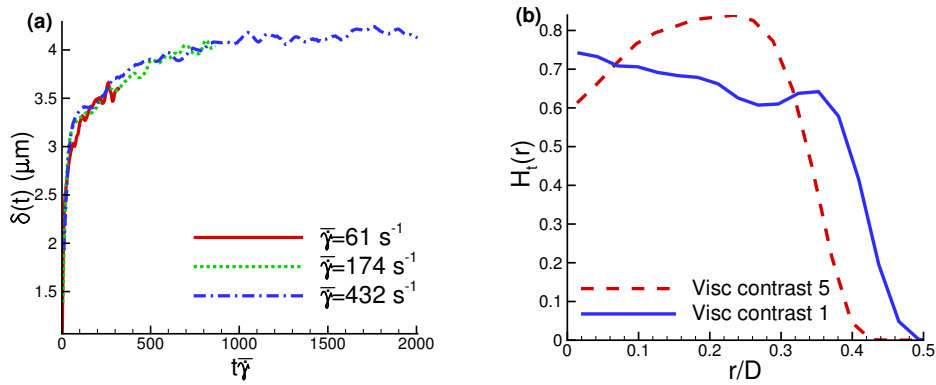


Figure 4.6.: $D = 20 \mu\text{m}$ and $H_t = 0.3$: (a) CFL development over time for the simulations with viscosity contrast. (b) hematocrit distribution across the channel for simulations with and without viscosity contrast.

The hematocrit distribution across the channel looks also differently: Fig.4.6(b). As we can see, RBC are occupying not exactly the center of the channel, but an intermediate area. That arrangement might be, possibly, because the higher RBC viscosity makes them more difficult to squeeze between each other and increases the role of cell-cell interaction.

The comparison of CFL dynamics for permeable and non-permeable vesicles also brings an interesting result (Fig 4.7). The green dash-dot-dot line depicts the dynamics of RBCs with permeable membrane. The CFL here converges much faster, than for blue and red lines, which stay here for non-permeable membranes. Blue line shows the dynamics of RBCs with $\lambda = 5$, red line - $\lambda = 1$. TT RBC Converge first stage of CFL faster, than TB. However, the lines coincide close to the end. That might mean, that at the channel center packing and “bumping” play more role, than lift force.

As a result, RBCs with a viscosity contrast of 5 make relative viscosity of simulated blood lower, and intensify the Fahreus-Linquist effect. A thicker

CFL results in a lower flow resistance. On the other side, the CFL convergence time for a larger viscosity contrast appears to be longer, so that a blood vessel should be long enough to take the advantage of a thicker CFL.

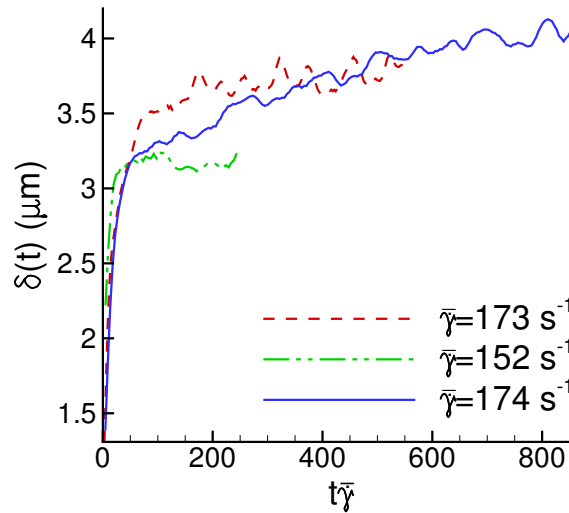


Figure 4.7.: Comparison of CFL dynamics for permeable (green dash-dot-dot line) and non-permeable vesicles (blue solid and red dashed lines). Difference between blue and red lines is different viscosity contrasts: 5 for blue and 1 for red. RBCs with higher viscosity contrast develop CFL slower.

4.3.3. Effect of RBC aggregation

The presence of aggregation interactions between RBCs leads in general to a larger CFL thickness. Figure 4.8 compares the development of CFL thickness for the cases with/without aggregation interactions. Initially, the CFL for the simulations with RBC aggregation seems to develop similarly to the cases without RBC aggregation present. However, attractive interactions between RBCs lead to a larger final CFL thickness δ_f in comparison with that without aggregation. The dynamics of CFL development appears to be not significantly affected by the presence of RBC aggregation such that δ_f plateau is roughly reached at $t\bar{\gamma} \approx 25$, independent of RBC aggregation properties. Note that the strength of RBC aggregation used here corresponds to normal aggregation level in blood under healthy conditions [34], and stronger aggregation interactions

4. Microvascular blood flow resistance: role of red blood cell migration and dispersion

between RBCs, which may be present in some blood diseases and disorders, may alter the conclusions. However, we expect that effective attraction between RBCs should shorten the time for CFL convergence rather than extend it and therefore, the estimated CFL development time should become even faster for stronger RBC aggregation present. Finally, at high enough flow rates ($\bar{\gamma} \gtrsim 50 \text{ s}^{-1}$ for the healthy aggregation level) RBC aggregation should not make a significant contribution to blood flow properties [34], see also Fig. 4.9(a).

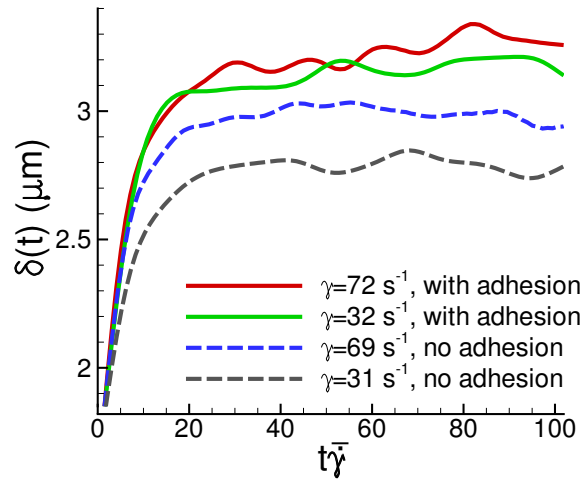


Figure 4.8.: Effect of RBC aggregation. CFL development over time for blood flow with/without RBC aggregation interactions. $D = 20 \text{ } \mu\text{m}$ and $H_t = 0.3$.

4.3.4. Theoretical model for CFL

The importance of CFL thickness is its direct correlation with blood flow resistance. The larger the CFL, the lower the resistance to blood flow will be, which has been found in the Fahraeus-Lindqvist effect [38]. The final CFL thickness δ_f increases with flow rate and channel diameter as illustrated in Fig. 4.9. Also, RBC aggregation enhances the CFL at least at small enough flow rates. The final CFL thickness δ_f is a consequence of the lift force on RBCs driving them away from the wall [2, 7, 68] and cell-cell interactions or collisions in the bulk of flow dispersing the RBCs. Thus, to describe δ_f with respect to different shear rates theoretically, the lift force on RBCs, which compresses the

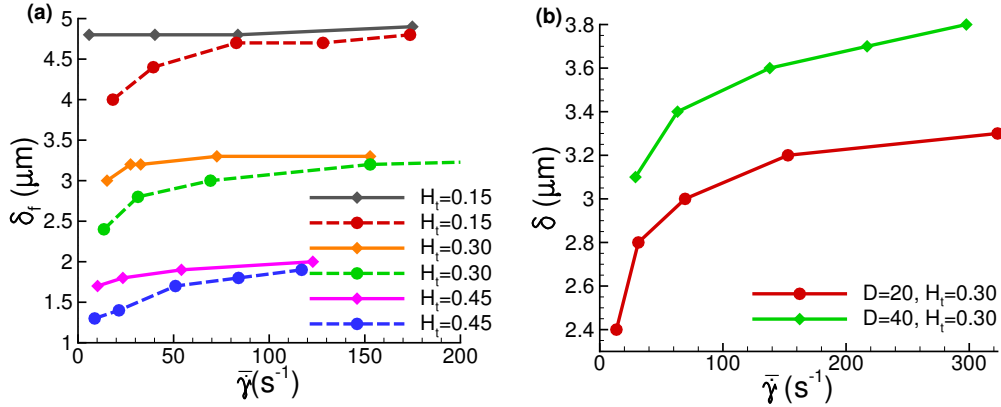


Figure 4.9.: CFL thickness for a converged flow for different flow rates and channel diameters. (a) Final CFL thickness δ_f for $D = 20 \mu\text{m}$. Solid lines correspond to simulations with aggregation interactions between RBCs, while the dashed lines are simulations without RBC aggregation. (b) Final CFL thickness δ_f for $D = 40 \mu\text{m}$.

cell core of the flow, should be balanced by an effective pressure due to collisions in flow. Following the idea based on an effective temperature in Ref. [110], a particle pressure Π in a sheared colloidal suspension can be described as

$$\Pi = n(k_B T + c_s \eta_{eff} \dot{\gamma} V_r) Z, \quad (4.2)$$

where $n = H_t/V_r$ is the RBC number density, c_s is a constant, η_{eff} is an effective suspension viscosity, $\dot{\gamma}$ is the shear rate, and Z is the compressibility. The first term in Eq. (4.2) corresponds to the thermal contribution of pressure, while the second term represents the shear-induced component due to particle interactions or collisions in flow [39, 45, 60]. The compressibility Z for a suspension of spherical colloids has a number of different theoretical approximations, where that by Carnahan & Starling [8] is perhaps the most successful one with

$$Z(\phi) = \frac{1 + \phi + \phi^2 - \phi^3}{(1 - \phi)^\alpha}, \quad (4.3)$$

where ϕ is the particle volume fraction and $\alpha = 3$. For RBCs, the compressibility Z is likely to increase slower with ϕ than that for rigid spheres, so that α is likely to be smaller than 3. However, exact details are not so important here, since our goal is a semi-quantitative approximation of CFL.

4. Microvascular blood flow resistance: role of red blood cell migration and dispersion

The particle pressure inside the flow core is balanced by the surface pressure Π_s , which arises from a hydrodynamic lift force on RBCs and an entropic repulsion of RBCs from the wall due to hindered rotational motion. The entropic repulsion force can be approximated as $F_e = k_B T/h$ (e.g., for a rigid disk), where h is the distance from cell's center-of-mass to the wall. This force is only important at distances smaller than the disk radius and at very low shear rates ($\bar{\gamma} < 1$); for instance, it provides a non-zero CFL thickness in absence of flow. Here, we omit any dependence of F_e on the shear rate (in general, F_e should reduce with increasing shear rate), since its contribution becomes negligible in comparison with the lift force already for $\bar{\gamma} \geq 1$. Thus, the surface pressure can be approximated as

$$\Pi_s = \frac{F_e + F_l}{D_r^2} = \frac{k_B T}{h D_r^2} + \frac{c_l \eta_o \dot{\gamma} D_r^2}{h^2}, \quad (4.4)$$

where F_l is the lift force [13, 45, 68, 103] and c_l is a constant. In general, the lift force would depend on particle properties (e.g., rigidity, viscosity contrast between inner and outer fluids) and its dynamics (e.g., tank-treading or tumbling, inclination angle), so that Eq. (4.4) should be considered as an expression which captures general trends of a lift force on RBCs. The balance between these two pressures ($\Pi_s = \Pi$) allows us to describe semi-quantitatively the CFL thickness for different shear rates. As an approximation in both Eqs. (4.2) and (4.4), we assume $\dot{\gamma} = \bar{\gamma}$ of the tube flow, while η_{eff} in Eq. (4.2) is calculated according to the empirical relations for blood flow in tubes [85]. Also, for the compressibility Z in Eq. (4.3) we assume $\alpha = 2$, since a suspension of RBCs should be more compressible as that of hard spheres. Figure 4.10 presents the simulation data for δ_f against fits of the theoretical model with $c_s = 10^{-4}$ and $c_l = 10^{-3}$. The symbols correspond to simulation data, while the solid lines with corresponding colors are fits by the theoretical model. In spite of the simplicity of the model, the theoretical fits describe the data quite well, especially for a fixed diameter $D = 20 \mu\text{m}$ and different H_t values. The agreement for different diameters and $H_t = 0.3$ is less satisfactory.

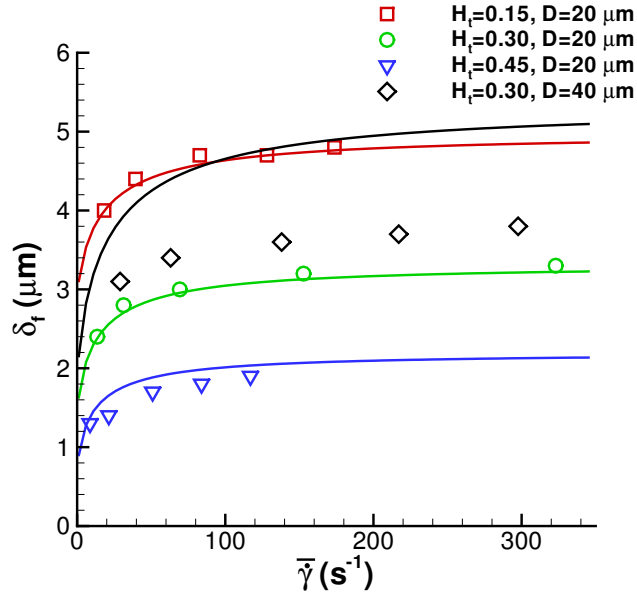


Figure 4.10.: Final CFL thickness for different flow rates, hematocrits, and channel diameters. The symbols correspond to simulation data, while the solid lines with corresponding colors are fits by the theoretical model with $c_s = 10^{-4}$ and $c_l = 10^{-3}$.

4.4. Discussion

Our simulations show that the initial rapid RBC migration away from the wall is nearly independent of the various conditions, such as hematocrit and flow rate, when scaled with the characteristic shear rate. This indicates that initially the shear rate is the only relevant time scale for the RBC migration. An experimental investigation of vesicle migration away from a wall [13] has shown that vesicle displacement Δy follows a power-law behavior $\Delta y \sim t^\beta$. A log-log plot of the CFL development curves shown as an inset in Figs. 4.2 and 4.3 indicates that the initial rapid CFL-thickness increase is close to a power-law behavior with an exponent of about $1/3$, which is consistent with the fact that $F_l \sim 1/h^2$. Thus, the initial migration of RBCs is similar to the migration of single cells. After that the RBC migration slows down and another time scale corresponding to the relaxation of RBC core due to cell-cell interactions becomes relevant. This can be seen better for the case of $H_t = 0.45$ in Fig. 4.3, where cell-cell interactions affect the CFL convergence. However,

4. Microvascular blood flow resistance: role of red blood cell migration and dispersion

for all investigated hematocrits ($H_t \leq 0.45$) the rearrangement process of RBCs in the flow core only weakly affects the time for CFL convergence as shown in Figs. 4.2 and 4.3.

Another important conclusion, which can be drawn from the CFL development results, is that the length of blood-flow convergence to steady state is practically independent of the flow rate. Thus, for physiological hematocrits, including those for normal microvascular blood flow [61, 84], the flow convergence time is equal to about $t_c \approx 25/\bar{\gamma} = 25D/\bar{v}$. Then, the length required for the flow to converge is $l_c \approx \bar{v}t_c = 25D$. For instance, for $D = 20 \mu\text{m}$, $l_c \approx 0.5 \text{ mm}$, independently of the flow rate and H_t .

The estimation of the convergence length for blood flow has direct implications for quantifying this effect on the flow resistance in microcirculation. Microcirculatory blood flow is not always steady, since, for instance, the distribution of RBCs in a vessel cross-section can be significantly distorted at bifurcations leading to a diminished CFL and an increase in the flow resistance. Following the flow development after a dispersion of RBCs, we can estimate an effective increase in resistance. For this purpose, we divide a length L of the channel into a number of slices of thickness Δx . Then, the pressure drop $\Delta P(x_i)$ at every slice i is equal to

$$\Delta P(x_i) = \frac{128Q\eta(x_i)\Delta x}{\pi D^4}, \quad (4.5)$$

where $\eta(x_i)$ is the effective viscosity at a slice i , which is a monotonically decreasing function of x as $x \rightarrow L$, since the CFL develops and its thickness increases. When, the CFL thickness comes to a plateau value, the local effective viscosity would also saturate. On the other hand, $\Delta P = (128Q\eta_{eff}L)/(\pi D^4) = \sum_i \Delta P(x_i)$. Thus, the effective viscosity over the channel length L can be expressed as

$$\eta_{eff} = \frac{1}{L} \sum_i \eta(x_i)\Delta x \approx \frac{1}{L} \int_0^L \eta(x)dx = \bar{\eta}. \quad (4.6)$$

The effective resistance over the channel length L characterized by η_{eff} will mainly depend on L and the initial dispersion of RBCs which would affect $\eta(0)$. The performed simulations corresponds to the worst-case scenario of RBC dispersion, since they are allowed initially to diffuse and fill up the full

channel cross-section. Therefore, the maximum value of $\eta(0)$ can be estimated as the bulk viscosity of blood for a given tube H_t , which is normally several times larger than the plasma viscosity for physiological H_t values. However, the RBC core distortion past vessel bifurcations in blood flow is likely to be less than that assumed initially in simulations and hence, $\eta(0)$ is generally expected to be even smaller in microvasculature. With respect to the vessel length L , the effect of potential RBC dispersion can be practically neglected if $L \gg 25D$; however, it may noticeably increase the flow resistance if L is smaller than or comparable to $25D$, which is an approximate CFL convergence length. Characteristic lengths of microvascular vessels between bifurcations [81] are on the order 0.5 – 1 mm. Thus, the contribution to blood flow resistance due to the potential RBC dispersion at vessel bifurcations and junctions is expected to be rather small for vessels with diameters $D \lesssim 20 \mu\text{m}$, while in vessels with larger diameters this contribution should be significant.

Aggregation interactions between RBCs lead to a reduction of blood flow resistance evidenced by the increased terminal CFL thicknesses in Fig. 4.9(a). The corresponding flow resistances characterized by the relative viscosity are shown in Fig. 4.11. The relative viscosity is defined as $\eta_{rel} = Q_{plasma}/Q_{RBC}$, where Q_{plasma} corresponds to the rate of flow of plasma without RBCs, while Q_{RBC} is the flow rate of blood for the same pressure gradient. Analogously, $\eta_{rel} = \eta_{app}/\eta$, where η_{app} is the apparent blood viscosity in tube flow. The curves in Fig. 4.11 demonstrate that aggregation interactions in blood lead to a decrease in flow resistance, at least at the low flow rates which would be relevant in the venular part of microcirculatory blood flow. It is also likely that the aggregation interactions between RBCs would lead to a lower distortion of RBC flow core at bifurcations further contributing to the reduction of flow resistance.

Finally, the theoretical model for the δ_f thickness confirms that the main mechanisms for CFL formation are the lift force which drives RBCs away from the wall and the shear-induced pressure due to cell-cell interactions in flow which disperses RBCs. Thus, δ_f corresponds to a CFL thickness when these two driving forces balance each other. The value of c_s for RBC suspension is considerably smaller than that estimated for colloidal suspensions ($c_s = 1/9$) in Ref. [110]. This might be due to an alignment of RBCs in flow such that

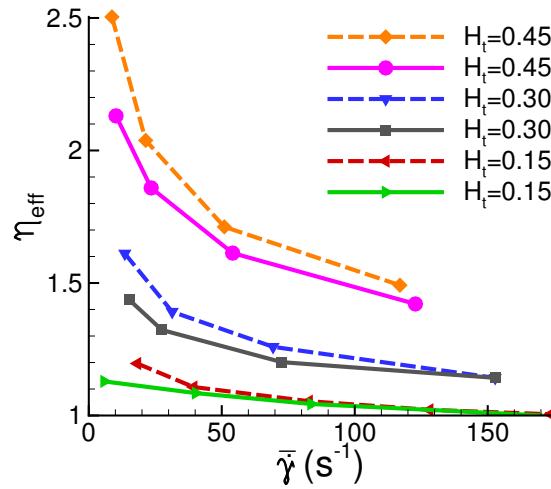


Figure 4.11.: Relative viscosity (the ratio of blood apparent viscosity to plasma viscosity) of blood flow for different H_t values, flow rates, and RBC aggregation. $D = 20 \mu\text{m}$. The data are shown by solid lines for systems without aggregation interactions and by dashed lines for the simulations where RBC aggregation interactions were present.

the effective particle size for inter-cell collisions is much reduced. Another uncertainty comes from the assumption for the function Z whose value might be well overestimated. The value of c_l in this work also appears to be much smaller than that suggested for single vesicles ($c_l \approx 0.1 - 0.2$) in Refs. [68, 103]. A reduction in lift force is likely to happen due to the alignment of RBCs in flow and their increased concentration. However, the ratio of the constants c_s and c_l , which determines the value of δ_f at large $\bar{\gamma}$, is not very far from the above estimations [68, 103, 110]. Due to a number of simplifying assumptions, the discrepancies between the δ_f values and the fits in Fig. 4.10 are not entirely surprising and can be easily alleviated by changing the constants c_s and c_l , which are likely to be sensitive to different RBC dynamics and local concentration. Finally, following these arguments we can often anticipate the changes in CFL thickness and flow resistance. For example, for rigidified RBCs the lift force should be considerably reduced, and therefore, it should result in a smaller CFL thickness. Also, more spherical suspended cells and/or particles than RBCs are also subject to a reduced lift force from the wall.

4.5. Summary

We have investigated the development of CFL in blood flow starting from a fully dispersed cell configuration. RBCs migrate away from the wall due to a lift force which arises from cell-wall hydrodynamic interactions. The convergence of CFL thickness toward a constant δ_f value at steady-state flow appears to be nearly universal if scaled with the average shear rate, and the corresponding power-law behavior is similar to that of a single vesicle migrating away from a wall. Aggregation interactions between RBCs lead to a larger CFL thickness in comparison to the flow where attractive interactions between cells are absent. The final CFL thickness δ_f is well described by a theoretical argument that at steady state a balance between lift forces on RBCs and shear-induced effective pressure due to cell-cell interactions in flow exists. The theoretical model describes quite well the δ_f dependence on shear rate in spite of many simplifying assumptions made.

Our results allow us to estimate the effect of a reduced CFL thickness on blood flow resistance which may occur, for instance, at vessel bifurcations where RBC can get dispersed. The universality of CFL convergence with respect to flow rate results in the estimation for the vessel length l_c required for full CFL development to be approximately $25D$. Thus, in vessels with a length comparable or shorter than $25D$ the effect of RBC dispersion on the flow resistance might be considerable, while in much longer vessels this effect may be neglected. Quantitatively, this effect can be taken into account by averaging the effective fluid viscosity $\eta(x)$ along the vessel length, which is directly associated with the CFL development. Finally, the presented results are not only relevant for blood flow, but also for a flow of suspension of deformable particles such as vesicles, capsules, and cells. Their migration mechanisms are expected to be similar, even though quantitatively the current predictions may be altered, since the lift force and shear-induced pressure depend on the properties and dynamics of specific particles. We hope that the presented results will trigger further investigations of such systems in order to better understand their flow properties.

5. Segregation mechanism of multicomponent suspension under flow

5.1. Introduction

Blood consists of plasma, red blood cells (RBC), platelets and white blood cells (WBC). The cells are suspended in plasma. Under normal conditions, humans have about 45% of RBC by volume, in blood and much less WBCs and platelets. Thus, blood can be considered as a multicomponent suspension, where some types of particles might be in the near-wall region, while others stay at the center.

The near-wall region is interesting from the particle-adhesion standpoint, since particles in that region can interact with the wall, and potentially be transported to tissues through the vessel walls. Otherwise, if particles always occupy the center region, they will be simply carried further by the flow. Thus, the region is interesting for drug delivery, and if we can predict the behavior of different particles in blood flow, we can construct more efficient drug carriers.

Due to differences in shapes, stiffnesses and sizes, particle segregation phenomena in blood under flow can occur. For example, Fig. 5.1 a) shows, that a large particle might be pushed toward the vessel wall by RBCs. In the other example in Fig. (5.1 b)), we see that small particles also end up in the near-wall region. Different shapes and sizes of nano- and micro-carriers have been used to investigate the migration of particles in blood flow numerically [72] and experimentally [17, 47, 102], in order to identify good particle characteristics for drug delivery.

5. Segregation mechanism of multicomponent suspension under flow

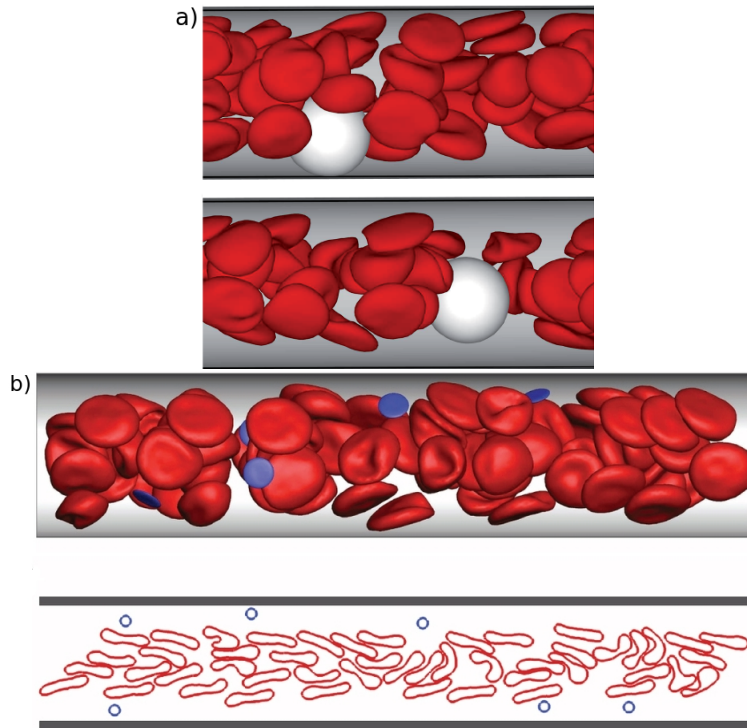


Figure 5.1.: a) Snapshot of the simulation from Ref. [30]. At high hematocrits RBCs are pushing a WBC to the wall, while at low hematocrits a WBC stays in the center. b) Snapshots of the 3D and 2D simulations from Ref. [72]. RBCs are located mainly at the center of the channel, while platelets are pushed to the wall.

Our main target here is a theoretical explanation of the segregation phenomena using Fokker-Planck equation. The equation connects the particle distribution, with a force acting on particles and their diffusion across the channel. Measuring the force, diffusion and distribution of particles, we can verify whether the Fokker-Planck equation properly describes the segregation phenomenon. This result would indicate that particle drift force and its local diffusion are the two main mechanisms for the segregation in flow.

Considering a two-component suspension under Poiseuille flow. Measured any two of the parameters, the third one can be extracted from the Fokker-Planck equation. For example, blood particles distribution across the channel in a converged flow can be measured experimentally. Next, the force profile or diffusion across the channel are needed. It is also not very difficult to measure the force acting on every particle in simulations, because it is calculated every

time-step for equations of motion. To measure the diffusion constant profile, we will need another simulation to eliminate the lift force effect. This can be done with Lees-Edwards boundary conditions [58]. Modeling different hematocrits and flow rates we can measure particle distribution at various conditions, and then use it in the discretized Fokker-Planck equation.

Additionally, we investigate the diffusion of soft particles depending on different hematocrits and shear rates. It is known, that for rigid spheres in simple shear flow the effective diffusion constant can be estimated through a collision frequency in the flow or so-called particle-particle collisions [6, 60]. This estimation gives $D \sim \phi\dot{\gamma}$, which means the more particles in the unit volume ϕ , the more collisions a particle has, the higher diffusion constant is found. And there is a higher probability for a particle to be "kicked" under high shear rates $\dot{\gamma}$.

5.2. Models & Methods

5.2.1. Fokker-Planck equation

The Fokker-Planck (FP) equation describes particle distribution depending on the force acting on particles, and diffusion profile across the channel. Also, it is known as Kolmogorov forward equation, introduced by Andrey Kolmogorov [56]. In application to particle distribution it is called Smoluchovski equation. Any two-component suspension in flow can segregate. In simulations, we can measure all components of the FP equation including the force on a particle, the diffusion profile and the particle distribution profile. Our idea is to plug in the simulation results onto the Fokker-Planck equation.

After the flow in a microchannel has converged, we can consider the system to be in steady state. Therefore, we can neglect the left part of the FP equation. Thus, we verify stationary properties including particle distribution, force profile, and diffusion profile. It is known, that blood viscosity increases with increasing hematocrit. This means, that blood viscosity across the channel is also not constant, because the lift force on RBCs is pushing them away from the wall. As a result, we have a plasma layer in the near wall region and high hematocrit at the channel center.

After obtaining these measurements from simulations, we can numerically solve the equation to verify if the FP equation corroborates the simulation results. For that we have performed 2D DPD simulations with RBCs and other suspended (target) particles in Poiseuille flow.

5.2.2. Fluid model

The model of the fluid flow has been performed using DPD [22] method, as described in Chapter 2.

5.2.3. Model of blood cells

RBCs and target particles are modeled as closed bead-spring chains (Fig. 3.1), which incorporate also bending rigidity and area constraint. Each RBC includes 100 beads while target cells are made from 50 particles. Target cells have diameters of $D_{RBC}/8$, $D_{RBC}/4$ and $D_{RBC}/2$ in different simulations. 2D model of the cells, made from DPD particles is coupled to the background fluid via DPD interaction.

5.3. Results

We will focus on blood flow behavior in microchannels. Figure 5.2 shows a snapshot of the simulation setup of RBCs and target cells in Poiseuille flow. Here, RBCs are more flexible, and have a larger area than target cells. Both deformability and larger size of RBCs lead to a larger lift force in comparison to that on target cells.

Every time-step we collected the force acting on every target particle across the channel from the equations of motion. Measured force profile for the target particles across the channel is shown in figure 5.3(a). We can see, that a particle undergoes strong lift force close to the walls (coordinate 0 and 40). However, other parts of the force profile (coordinates 8 and 33) have the opposite direction. There, target cells are pushed away from the channel center by the RBCs. So, the target cells experience different interactions: one from the lift force and another from RBCs. These interactions result in a distribution profile of the

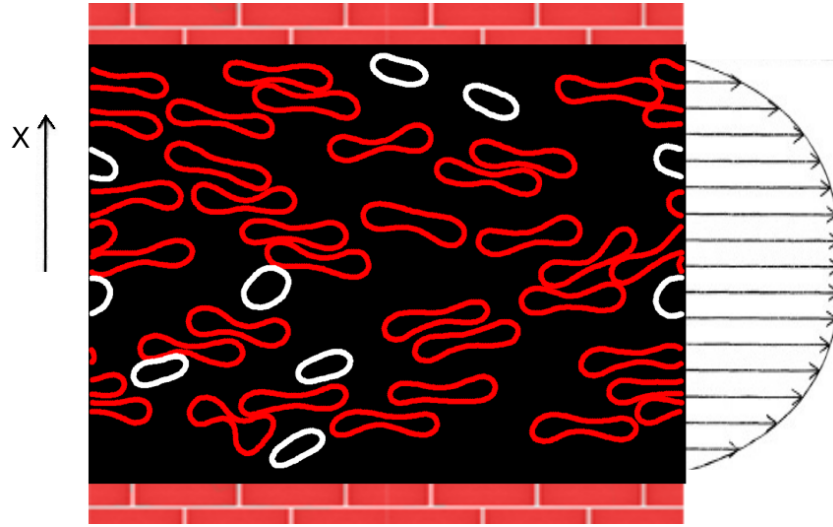


Figure 5.2.: Snapshot of the simulation setup. RBCs and target cells of diameter $D_c = 4 \mu\text{m}$ in the Poiseuille flow.

particles in Poiseuille flow, figure 5.3(b). This plot clearly shows that RBCs are located mainly at the channel center. The target cells are primarily located near the walls, however there is a probability of finding them at the channel center.

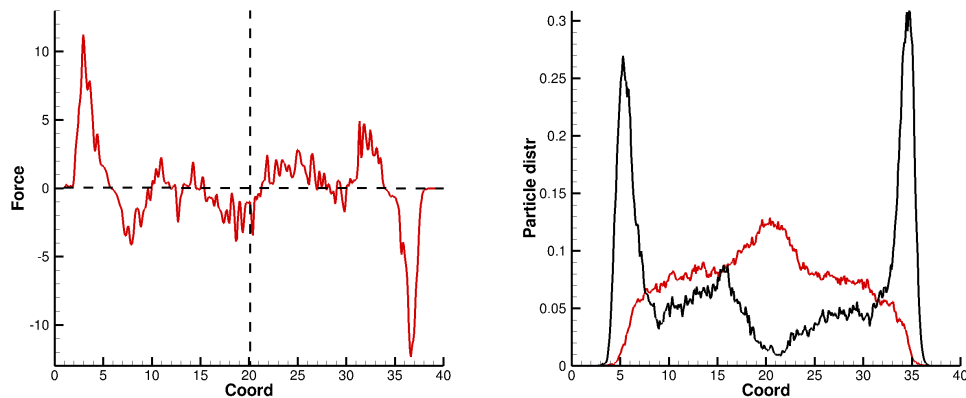


Figure 5.3.: (Left) Acting force on target particles across the channel. (Right) Distribution of the target particles (black line) and RBCs (red line) across the channel.

We have to add that calculated force profile is not correct directly at the walls, because particles are depleted due to a finite size. We know from previous studies [68] that the lift force decays as a power law with a distance from the

5. Segregation mechanism of multicomponent suspension under flow

wall. Therefore, the absolute value of the force for a point-like particle is highest at the wall, without a decay to zero. Confirmation of that we can see in the density distribution in Fig. 5.3(Right) - such that there are no particles very close to the walls.

Now we know the force on and the distribution of target particles, so the only thing missing is the diffusion across the channel. The diffusion constant in X-direction is reconstructed via multiple simulations with a single target particle in RBCs in shear flow (figure 5.4) using Lees-Edwards boundary conditions [58]. These conditions were taken to eliminate the presence of lift force and measure diffusion (no walls - no lift force). By varying shear rates and hematocrit values, we reproduce different shear planes of the Poiseuille flow in the X-direction.

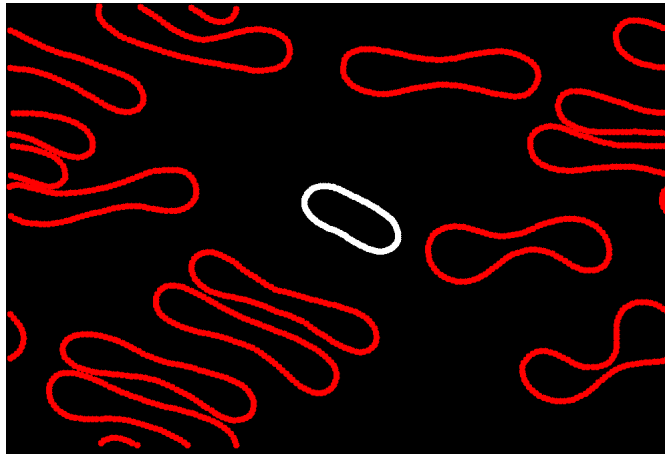


Figure 5.4.: Snapshot of the simulation setup of diffusion measurements. RBCs and a target cell are in simple shear flow.

The resulting plots (Fig. 5.5, 5.6) show, that diffusion grows with increasing hematocrit and shear rate. For low hematocrit values, the diffusion change with shear rate is not very dramatic, as for high hematocrits. This can be explained by the increase of particle collision frequency with other particles in flow. The more collisions per unit time we have, the higher diffusion constant should be. This result is consistent with the previous studies using colloids [6] and with experimental results in Ref. [45]. The latter also shows that diffusion constant decreases with decreasing shear rate and hematocrit, or with frequency of pair interactions $D \sim \dot{\gamma}\phi$, where ϕ is particle concentration. However, at high concentrations the cell-cell interactions are estimated to be more significant

and take the dependence of ϕ^2 instead.

For a two-component suspension in bounded simple shear flow, a detailed theoretical model was developed in Ref. [94] similar to the FP equation. In this study, the resulting differential equation predicts well the segregation development of the two-component suspension which has been also corroborated by boundary-integral simulations.

The main result of this section is shown in figure 5.7. We can see, that the theoretical curve is very close to the simulation one. This result indicates, that segregation of multicomponent suspensions can be described well using the Fokker-Planck equation. However, there experimental confirmation for the segregation is still very difficult. Even though density distribution profile can be measured directly after a flow is converged, diffusion constant and force profiles are not easy to obtain.

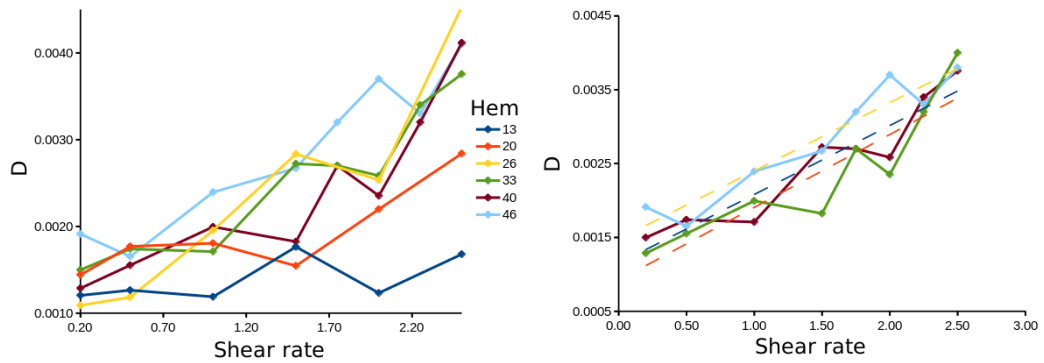


Figure 5.5.: Diffusion constant (D) of a target cell for different hematocrit values (Hem) and the shear rates. The figure on the left displays a linear trendline.

5.4. Summary

We have investigated particle distribution of a two-component suspension at low Re in Poiseuille flow. In Poiseuille flow every flexible nonspherical particle is pushed away from the wall by the lift force. Also, at the channel center we can observe multiparticle collisions (cell-cell) interactions. The lift force and cell-cell interactions are considered as two governing mechanisms in the segregation phenomenon. Moreover, the lift force and cell-cell interactions compete in the flow.

5. Segregation mechanism of multicomponent suspension under flow

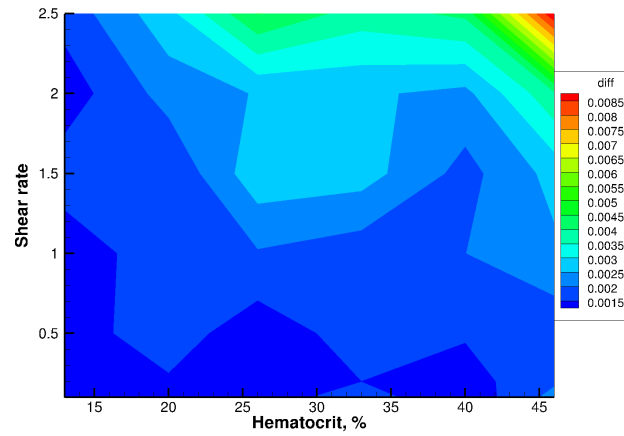


Figure 5.6.: Diffusion constant depending on shear rate and hematocrit value for a target cell.

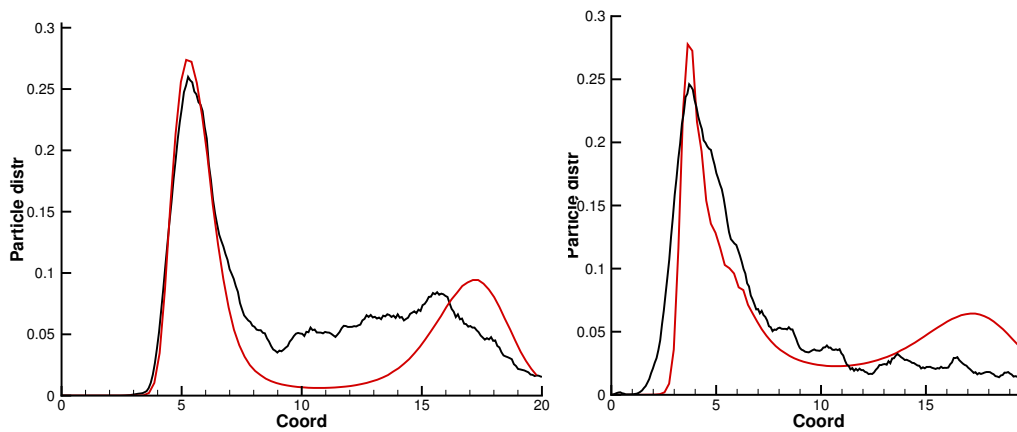


Figure 5.7.: Theoretical (red) and simulation (black) results. On the left target cell has $D_c = 4 \mu m$, on the right $D_c = 1 \mu m$.

The Fokker-Planck equation has been used to verify these two mechanisms. We showed that segregation phenomena of a multicomponent suspension can be described well by Fokker-Planck equation. Thus, if two profiles from probability distribution, diffusion constant, and force across the channel are known, we can obtain the third one. These results are similar to theoretical studies in ref. [94], where the non-canonical diffusion-drift equation leads to two partial differential equations for the distribution of a two-component suspension under simple shear flow.

Additionally, we examined diffusion behavior of target cells suspended in blood. Our results show, that diffusion increases linearly with increasing shear. This outcome is consistent with that for colloids [6]. Also, we found that the diffusion is larger at high hematocrits, which has been shown experimentally [45]. This can be explained by cell-cell interactions within the flow, as $D \sim \dot{\gamma}\phi$ for low concentrations, and $D \sim \dot{\gamma}\phi^2$ for high concentrations, where cell-cell interactions become more important in comparison to the shear rate.

6. Simulation of complex geometries

6.1. Introduction

In order to simulate more realistic vessel geometries in the vasculature, open boundary conditions (BC) are needed. Periodic boundary conditions (PBC) are useful for simulating straight tubes, or periodical structure/vasculature. However, it might become computationally expensive and unrealistic to reproduce a symmetric image of the system, only to be able to use PBC. For example, to measure reliable RBC distribution in a channel after passing a bifurcation, we should make the parent and daughter channels long enough to have the flow converged ($\sim 25D_c$) and then make another setup mimicking the mirror reflection, only to fulfill the PBC (figure 6.1). For this reason, we started to develop so-called “in- and out-flow” boundary conditions (IOBC), in order to simulate complex vascular structures and save computational time.

Such a simulation method can be tested using microscope images or MRI results by a simulation of the blood flow in a small piece of body tissue, e.g. liver. Moreover, it can be combined with a continuum fluid model, in order to construct a multi-level blood-flow simulation, where the arterial blood flow is simulated by the continuous model and the microcirculation by the mesoscale method.

6.2. Outflow boundary conditions

The outflow BCs were introduced in Ref. [59] for the DPD method. Let us consider a tube flow as in figure 6.2. Before the “plane Q” the tube is divided

6. Simulation of complex geometries

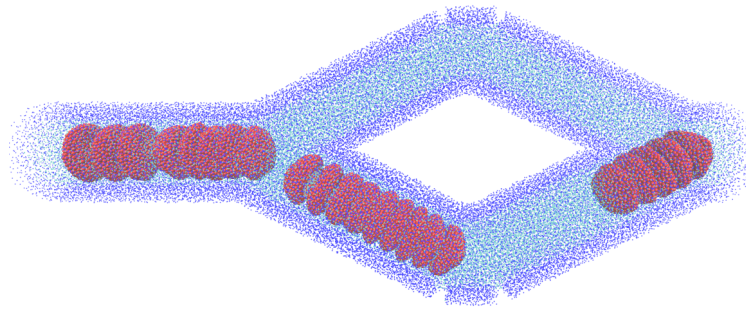


Figure 6.1.: Simulation snapshot of a model of a vascular branching. The fluid with RBCs flows from left to right with PBC.

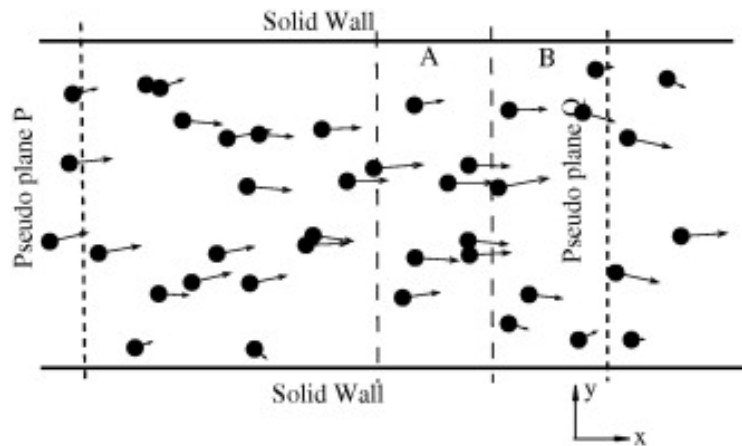


Figure 6.2.: Schematic explanation for in- and outflow boundary condition for a tube flow. From Ref. [59].

into two areas (A and B in the figure), in which velocities of particles are compared. In a fully developed flow, the difference between average particle velocities in both domains must be zero. Thus, we should apply the adaptive force for the several first time-steps to get the fully developed flow. After that, the force is switched off.

The idea for the force is to make flow converge at the outflow surface (“Pseudo-plane Q” in Fig. 6.2), using adaptive forces similar to that from the Section 2.5. The outflow-surface is a plane that closes the end of the simulation tube or microchannel, and particles which cross the plane are deleted. To control the flow rate and minimize velocity differences between the two areas (A and

B in the figure), we apply the adaptive force on the particles near the outflow:

$$\begin{aligned}
 f_{out}^k(h) &= \beta^k(1 - h/r_0)^p + \gamma^k f_{press}(h), \\
 \beta^{k+1} &= \sum_{\sigma=0}^q \beta^{k-\sigma} + \xi(v_A^k - v_B^k), \\
 \gamma^{k+1} &= \gamma^k + K(\phi^k - \phi_0)
 \end{aligned} \tag{6.1}$$

where the first part of the force removes the velocity difference between areas A and B, and the second controls the flow rate at the “plane Q”. Here, k is the iteration number, ξ is the relaxation parameter, and β^k is the adaptive coefficient. Also, h is the distance from a particle to the outflow boundary, and r_0 is the thickness of the domains. r_0 is usually taken to be the cut-off radius in the DPD method. v_A and v_B are average particle velocities in the domains. The parameter p defines the strength of the adaptive force and equal is to $p = 6$. This value is calculated as a best fit for a decay of the dissipative force from a DPD particle on the surrounding particles within the distance r_c . The number of relaxation steps to be considered, q , is calculated as follows:

$$q^{k+1} = \begin{cases} q^k + 1, & \text{if } n^k < n - \delta n \\ q^k, & \text{if } n - \delta n < n^k < n + \delta n \\ q^k - 1, & \text{if } n^k > n + \delta n \end{cases} \tag{6.2}$$

where n^k is the mean number density at k th step and, δn is an accepted density deviation.

The other part of the adaptive force controls the flow rate at the “plane Q”. Here, ϕ^k is the instantaneous outflux and ϕ_0 is desired the outflux value which is calculated depending on the flow parameters.

The force $f_{press}(h)$ mimics the repulsion from the particles on the right side of the “plane Q”, similar to that from a wall made of frozen particles. The $f_{press}(h)$ on a particle i is calculated as an integral of the repulsive DPD force multiplied by the radial distribution function over the semi-sphere around the particle:

$$f_{press} = \int_{V_s} F^C(r)g(r)dV, \quad (6.3)$$

where $g(r)$ is the radial distribution function.

The fluid particles are deleted at the outflow surface to fulfill a volumetric flow rate which is calculated depending on the flow properties. If simulated, RBCs or other particles will be also deleted entirely after the last particle of the membrane crosses the “plane Q”, to avoid problems with calculating the total area, volume etc.

6.3. Inflow boundary conditions

At the pseudo “plane P” in figure 6.2 particles are inserted to mimic the inflow of fluid. The inflow conditions depend on the fluid density and the flow velocity. Thus, the product of the timestep, density, velocity and an area of the plane gives us the number of particles N_A to be inserted:

$$\begin{aligned} N_A^i &= N_A^{i-1} + n\delta t dA v_n, \\ N_A^i &= N_A^i - 1, \text{ if } N_A^i \geq 1. \end{aligned} \quad (6.4)$$

where i is the simulation step, n is the number density of a fluid, and v_n is the local normal velocity for the local area dA at the inflow “plane P”. Velocity of the inserted particles for the tube is calculated according to the parabolic velocity profile:

$$v_n(y) = v_{max} (1.0 - (y/R - 1)^2), \quad (6.5)$$

where v_{max} is the maximum velocity of the Poiseuille flow, and R is the channel radius.

This number of particles is randomly inserted at the area dA of the “plane P” with randomized velocities from Maxwellian distribution around the desired mean value with know a temperature. Because of the thermal fluctuations, particles might go in the wrong direction (to left in the figure), and therefore the “plane P” is reflective from the right side. Such kind of insertion leads to

the local number density fluctuations on the order of 5% because of the softness of DPD interactions.

The same force f_{press} is acting on the fluid particles in the direction from the left to right at of the “plane P”

In this IOBC method, the number of particles is not strictly conserved, since the number of particles inserted is not connected to the number of particles deleted.

6.4. Volumetric driving force

In principle, inserted particles should push the other particles towards the end of the simulation domain because of the incompressibility. However, due to compressibility artifacts in the DPD method, the fluid density is not uniform along the channel. This situation is much better for simulations using the

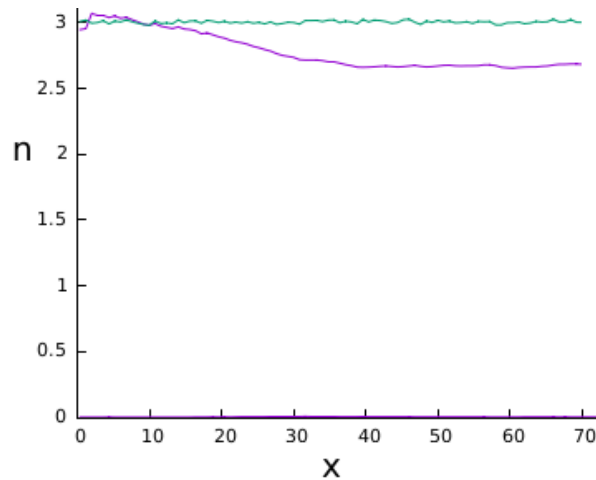


Figure 6.3.: In- and outflow simulations: density profile along the channel. The fluid is driven by the same volume force for DPD (purple line) and SDPD (green line) methods. Channel diameter $D_c = 10 \mu\text{m}$, length $L = 70 \mu\text{m}$.

SDPD method, but it is still better to use a body force which act on every particle in the fluid in addition to particles insertion to a desired flow rate (Fig. 6.3). A fluid with the same number density, viscosity and other parameters but using different simulation methods (DPD and SDPD) was driven by the same volumetric force. The DPD fluid is very compressible making the IOBC

setup more difficult, than the SDPD fluid. If we decrease the volume force for DPD method, we will have better density profile. Also, a higher fluid density might be used to eliminate the compressibility problems, however, this leads to higher computational costs.

In order to provide more natural results in our simulations, we compared pressure and velocity fields for a fluid modeled with the continuous method and the SDPD method. Comparison between a continuous fluid model solver and our particle-based simulations for the SDPD fluid shows that there is no significant difference in the way of driving the fluid: the whole fluid in the general flow direction or depending on the direction of a particular branch of the system. For complex geometries that means easier calculations of the driving force and reliability of the method.

6.5. Inflow of RBCs

Until now only IOBC for fluid particles and outflow of RBCs have been described. At the moment, we are developing BCs which would allow insertion of RBCs into the system at the beginning of the channel. This requires an insertion of RBCs under the conditions of the converged fluid flow. To make the computations cheaper, we should eliminate the long part at the beginning of the channel required for flow convergence.

An interesting approach was developed in Ref. [53]. The main idea is to use a “preseeding periodic domain” with ghost particles which is a short straight channel but is long enough to avoid an interaction of RBCs with their periodic images. This domain is placed just before the beginning of the simulated channel (Fig. 6.4). Once the flow in this generating domain is converged, the ghost particles from the periodic domain after crossing the border are inserted further to the right channel which is connected to a complex vascular structure. Here, we also have the reflection BC from the right side of the insertion plane, so that particles can flow only from left to right. Particles from the main simulation domain do not act on particles in the generating domain, so that the generating domain is completely independent from the main one.

In more detail, ghost particles from the region $A2$ (Fig. 6.4) are inserted into

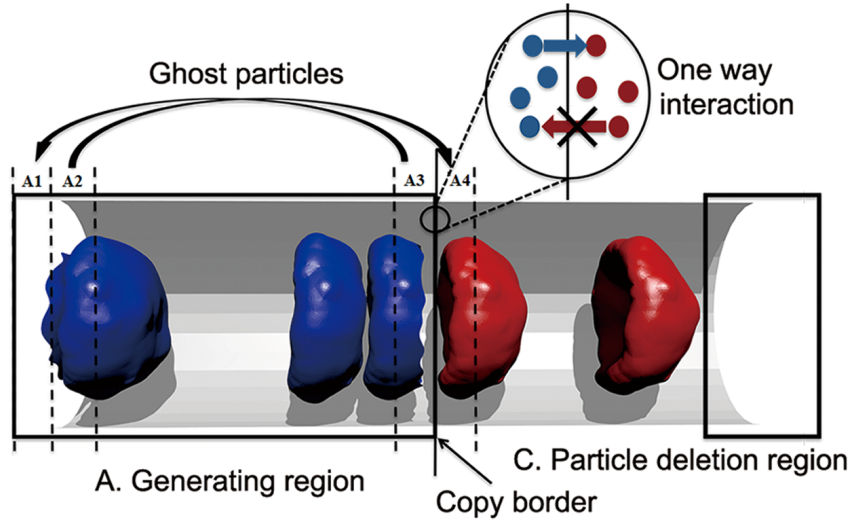


Figure 6.4.: Periodic feeding domain is located on the left of the main simulation domain. Once the flow is converged in the feeding domain, the flow can be transferred to the simulation domain on the right from the feeding part. Ref. [53].

the domain $A4$; particles from the $A3$ are inserted into the $A1$. The thickness of the $A3$ and $A1$ domains is the cut-off radius taken in a simulation. The width of the $A2$ and $A4$ domains is taken to be D_{RBC} to copy the RBC completely from left to right.

The insertion of RBCs is a bit more complex than that for fluid particles because of the global area and volume constraints. We should insert an entire RBC in order to avoid difficult problems with of the RBC topology, when only a part of the RBC crosses the border. Thus, the whole RBC is duplicated into the main domain, after the last particle of the membrane crosses the right border of the domain $A2$. That provides us the natural insertion of RBCs and fluid particles to the simulations domain without any conceptual problems.

6.6. Summary

We described the simulation method, which allows us to simulate complex non-periodic vascular systems. First, the IOBC for fluid particles was presented. In a non-periodic system, the outflow BCs are achieved by applying the adaptive force which consists of two parts. The first part of the force controls the flow rate at the outflow boundary, while the second part eliminates velocity

6. Simulation of complex geometries

difference in the region before the boundary. At the inflow BCs fluid particles are inserted depending on the fluid density and the flow velocity in order to achieve a desired flow rate.

We have also found that for the IOBC the SDPD fluid shows less density fluctuations than a DPD fluid, leading to easier control of viscosity. Even though, the insertion of particles at the inflow BCs should generate fluid flow, the application of the body force to move the whole fluid appears to be a more favorable method for the simulations.

Second, the inflow simulation method for the insertion of RBCs into a system has been described. We set a pre seeding generating domain with ghost particles before the simulation's inflow plane of the system. The generating domain is a straight tube with PBCs. After the flow in the generating domain has converged, the ghost particles are inserted into the main simulation domain. This method allows us to implement a converged flow in the system from the beginning without any additional adaptive forces.

7. Concluding Summary

This thesis is dedicated to several problems concerning blood flow. Blood is a very important body fluid, which has been always of interest to scientists. It shows different behavior at different scales: in large arteries it might be considered as a viscous Newtonian fluid and described using continuous modeling, while at mesoscales the particulate nature of blood becomes important. For example, in capillaries, arterioles and venules blood flow the contribution of blood cells become important. Blood cells are deformable and can be considered as soft matter. Thus, to model blood flow properly the behavior of RBCs has to be considered. At mesoscale RBCs significantly affect the flow, so that theoretical and experimental investigations are needed to bring the answers to complicated question about blood behavior.

Here, RBCs are modeled by a hexagonal bead-spring mesh [26] on $3D$ simulations, coupled to the fluid which represents plasma. In $2D$ RBCs are closed bead-spring chains. The $3D$ model has area and volume constraints, an angular potential between every two connected edges of the mesh and dihedral potential for every two neighboring triangles of the mesh. The $2D$ representation has an area constraint and angular potential. The fluid particles and all beads are simulated by means of SDPD for $3D$ models and using DPD for $2D$ models.

Blood flow is simulated in straight channels with diameters from 10 to 100 μm - just in range, where the soft properties of blood are crucial. The length of the channel is taken long enough in order to eliminate the interaction of RBCs with their periodic images (typically 40 – 80 μm). The RBC volume fraction in simulated flows is 15 – 45% which covers not only physiological hematocrit values, but also brings a more systematic investigation of the flow behavior.

The dimensionless shear rate is taken in the range $\dot{\gamma}^* < 90$ to represent venular flow rates, and $\dot{\gamma}^* > 120$ for arteriolar rate. These shear rates are still

7. Concluding Summary

in low Re regime, so the inertial effects are negligible.

Under flow, hydrodynamic lift force acts on every non-spherical particle. Lift force pushes cells or particles away from the wall, and depends on size, flexibility and shape of a particle. Also, the lift force increases with increasing shear rate. As a result, all RBCs occupy the central region of the flow, and lead to so-called CFL - the region close to the wall void of RBCs. Because blood contains not only RBCs and plasma, but also WBC and platelets, and potentially nano- and micro-particles with drugs, the margination (segregation) phenomenon can be observed. RBCs are more likely to occupy the center, so that other particles are pushed toward the walls. This effect is interesting from drug delivery point of view, because they should get marginated for adhesion and then transmigrate through the vessel walls to the tissue.

In addition, the RBCs' central positioning reduces vascular resistance, because they move with a help of a "lubricating" plasma layer. We have investigated the resistance of blood flow starting from a random RBC configuration and followed by turning on the flow. This setup is chosen to mimic the RBCs distortion at bifurcations in the microcirculation. When a converged blood flow from a feeding vessel encounters bifurcations the RBC distribution is destroyed.

While RBCs are moving in flow, they migrate to the center and the CFL develops. Once the flow is converged and cells do not significantly change their distribution, the CFL thickness also converges and fluctuates around a final value. Converged steady flow is the result of the balance between cell-cell interactions and the lift force. The cell-cell interactions act to disperse the RBCs, while the lift force forces them to get together.

An introduction of the attractive interactions between RBCs to mimic rouleaux formation, results in a thicker CLF for the same simulation setups. Due to these interactions RBCs appear to be already grouped in the center of the flow and aid the lift force to counterbalance the cell-cell collisions.

The dynamics of RBC in flow is similar for different hematocrits and shear rates: a the rapid growth of CFL at the beginning is followed by a smooth convergence to the final plateau value. The initial fast convergence is similar to power law behavior for a single cell moving away from the wall. This shows that the lift force acts at a relatively short distance from the wall, and thus, it does not lead to a very thick CFL in wide channels.

We found, that the vessel length of about $25D$ is enough for flow to converge under physiological hematocrits for RBCs without viscosity contrast. For cases with physiological viscosity contrasts between the inner RBCs fluid and plasma the convergence length should be about 20 times longer. However, this is the question of a further research. It is important to note that this result can be different for altered RBCs, for example more rigid ones in malaria disease, because the lift force for them would be weaker.

The proposed theoretical model for the CFL thickness based on the pressure balance, confirms that the CFL dynamics can be considered as a competition between cell-cell interactions and the lift-force in flow. However, due to the simplifications made, the theoretical model does not cover all range of hematocrits. Moreover, there are no experimental works yet in order to compare the RBC-core-flow convergence.

The central arrangement of RBCs causes margination of other cells present in blood. The segregation of different particles in blood is an interesting topic since the knowledge of segregation behavior for different cells can help in producing better drug carriers, which would marginate in blood flow and result in their efficient adhesion.

In the second part of the thesis, particle distribution in a two-component suspension in Poiseuille flow is investigated. The segregation was simulated in a 2D DPD setup using in $40\ \mu\text{m}$ diameter channel. The segregation behavior arises because different particles in flow undergo different lift forces and shear-induced diffusion. As a result, one type of the particles can be found in the center, while another one is close to the wall.

Segregation in blood is mostly caused by RBCs. Erythrocytes are highly flexible and undergo tank-treading motion which results in a stronger lift force acting on them. As a result, RBCs are more likely to be found in the middle of the channel, while other cells are pushed away towards the walls. However, this behavior may change. For example, at high hematocrits $H_t > 45$, RBCs start preventing WBCs to be near the wall.

The Fokker-Planck equation has been used to verify the theoretical understanding of the phenomenon. If we assume that the equation properly describes the process, then the force on and diffusion of particles should be sufficient physical parameters to describe the segregation in flow. The force profile and

7. Concluding Summary

particle distribution in cross-flow direction have been measured in Poiseuille flow simulations. For the diffusion constant several simulations with Lees-Edwards boundary conditions were performed, to mimic different hematocrits and shear rates across the channel. These boundary conditions help to eliminate the effect of lift force, so that a pure shear-induced diffusion could be measured. After measuring the force and diffusion profiles, the discretized Fokker-Planck equation was solved to compare particle distribution to the segregation results from simulations. Our results show a good agreement between the Fokker-Planck equation and the simulation results.

Measured force profile confirmed that if a flexible particle undergoes a strong lift force near the wall which pushes it to the center, while in the middle the direction of drift force may change due to interaction with RBCs. The lift force is stronger for RBCs, and therefore they occupy the center. Consider the lift force as a gravitational force, acting on particles in space. As a result, heaviest particles will be found at the bottom, ie closer to the center of the channel.

Another interesting outcome from the simulations of diffusion constant is that it increases with increasing shear rate or/and RBC volume fraction. The diffusion-shear dependence is close to a linear one, in agreement with that for colloids [6]. An experimental study [13] shows similar result, connecting the diffusion constant with the volume ratio and shear rate: $D \sim \dot{\gamma}\phi$. Finally, the segregation of a suspension can be described by a balance between cell-cell interaction in flow (ie diffusion), and shear induced lift force.

To conclude, the present study of margination and segregation of soft vesicles and blood components provides insights about the blood flow resistance and its dependence on hematocrit, shear rate, tube diameter, and aggregation interactions. Additionally, the segregation behavior of a two-component suspension in Poiseuille flow has been investigated from theoretical and simulation points of view.

The third part of the work is devoted to in- and outflow boundary conditions (BC) the development of which might make us be able to simulate complex vascular structures without coupling channels to each other in order to fulfill the periodic boundary conditions. We could start or stop the channel wherever we want. The inflow BC is responsible for inserting fluid particles and RBCs into the simulation channel (vasculature). Outflow BC is responsible for proper

deletion of the fluid particles and RBCs conserving physics of the flow. Also, we have found that because of compressibility artifacts of the DPD fluid it is difficult to control the density along the flow. However, the SDPD fluid covers that drawback and keeps the local density around a desired value.

As a concluding remark, this study of the dynamics of soft particles in flow in this thesis presents new insights about the mechanisms of margination of blood cells such as platelets, red blood cells, and drug carriers in blood flow. Thus, a further insight is added to understand complex behavior of blood flow, develop early detection and new methods of the drug carrying for diseases as, for instance, malaria and cancer.

8. Outlook

The results presented in this thesis provide new ideas for further investigations. Here are several conceivable projects which might be followed after the thesis.

First of all, simulations of CFL convergence dynamics with RBCs with viscosity contrast should be investigated more detailed. Since results of the CFL dynamics differ in order of magnitude for a permeable and non-permeable membranes, there is an open question how accurate is the permeable membrane model to be used in investigations.

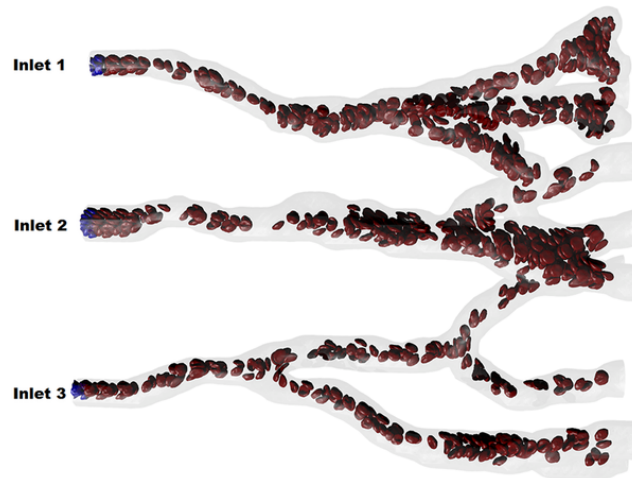


Figure 8.1.: Example of branching a model in microcirculation. The boundary conditions allow to set desired inflow properties from the left, and delete particles from the right. Figure is taken from Ref. [53].

Also, a model of a big system with several bifurcations should bring further understanding of the blood flow. RBC distribution depending on volumetric flow rate, hematocrit, and the cell properties might help to optimize drug delivery, and understand RBC-plasma separation. Moreover, using the boundary conditions like in Ref. [53] a small part of microcirculation in a tissue can

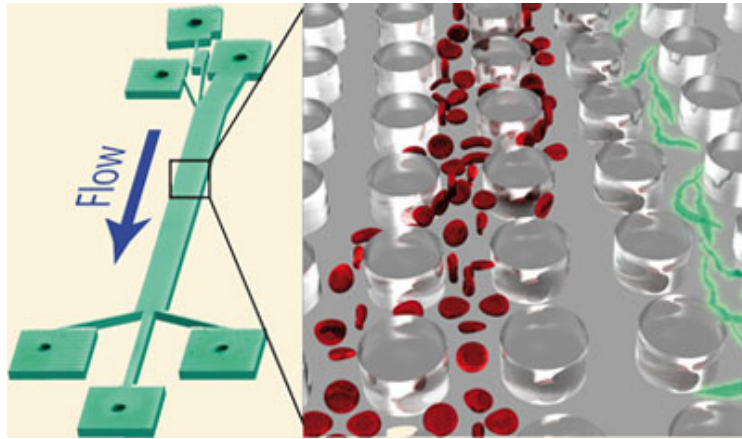


Figure 8.2.: An example of microfluidic device to separate RBCs from parasites. Picture taken from [48].

be simulated (Fig. 8.1) to investigate the role of vessel irregularities, and to identify new laws of blood flow. These laws are very useful to develop so-called $1D$ blood flow model, which is much cheaper computationally than a $3D$ model. Hence, much more complex systems could be simulated to investigate blood circulation. Also, such a development could be then integrated with magnetic resonance imaging results to reconstruct the vascular system of a body tissue.

Another interesting direction is to simulate more realistic blood vessels. In our simulations so far, they were considered to be straight and rigid. This is, of course, a simplification which helps to avoid certain simulation problems. Hence, vessels could be simulated as an elastic tissue with irregularities. Furthermore, vessels are covered by the endothelial surface layer or glycocalyx, whose thickness could be up to $1 \mu\text{m}$. This layer decreases the channel width and has also different properties under different shear rates.

Another interesting direction, can be to model blood flow in sickle-cell disease. In the disease hemoglobin polymerizes and forms strands which can burst the RBC membrane from inside. To model this effect an aggregation model is needed, which would allow the investigations of sRBC behavior in flow. sRBCs are stiffer and have different shape, which will also affect the CFL convergence and blood behavior at bifurcations. Also, bulk rheological properties of blood in sickle-cell disease can be investigated.

In this thesis pulsatile blood flow was not considered, although several studies

suggest that this property exists in microcirculation and increases capillary perfusion [52]. Thus pulsatile blood flow could affect the flow properties of RBCs and other blood component such as WBCs or drug carriers.

A RBC has different size during its lifetime - it is small ($5 - 6 \mu\text{m}$) at the beginning and can be up to $9 \mu\text{m}$ at the end. For microfluidic devices this is a crucial parameter which can be detected (Fig. 8.2). If the cell has a different shape, it might move differently in the device and be sorted out. This can be useful for the separation of old cells from young ones for blood transfusion.

Another step that might be taken, is to simulate the cells more detailed. The presence of different RBC and WBC membrane proteins could make possible to investigate the biocomputing nanoparticle drug delivery or the malaria parasite uptake *in silico*.

Appendices

Appendix A:

Single vesicle flow behavior

A.1: Keller-Skalak theory

Consider a vesicle with fixed ellipsoidal shape: $(r_1/a_1)^2 + (r_2/a_2)^2 + (r_3/a_3)^2 = 1$, where $i \in 1, 2, 3$ are Cartesian axes, and a_i is ellipsoid's radii. The motion of a vesicle is the balance between the energy that comes from flow and its dissipation at the membrane and inner fluid motion. The equation for the balance is:

$$\begin{aligned}\frac{d\theta_i}{dt} &= \frac{1}{2}\dot{\gamma} (B \cos(2\theta_i) - 1), \\ B &= f_0 \left(f_1 + \frac{1}{f_1} \frac{1}{1 + f_2(\lambda - 1)} \right), \\ f_0 &= \frac{2}{a_1/a_2 + a_2/a_1}, \\ f_1 &= \frac{1}{2}(a_1/a_2 - a_2/a_1), \\ f_2 &= \frac{1}{2}g(\alpha_1^2 + \alpha_2^2), \\ g &= \int_0^\infty (\alpha_1^2 + s)^{-3/2} (\alpha_2^2 + s)^{-3/2} (\alpha_3^2 + s)^{-1/2} ds, \\ \alpha_i &= \frac{a_i}{(a_1 a_2 a_3)^{1/3}}.\end{aligned}\tag{A.1}$$

where $\dot{\gamma}$ is the shear rate of the flow, B is the vesicle's parameter, which depends on viscosity contrast and the shape. In TT motion $B > 1$ and inclination angle can be found as: $\theta_i = \frac{1}{2} \arccos(1/B)$. In our simulations we mostly used $\lambda = 1$.

Appendix B:

Simulation of complex geometries

B.1: Domain construction

In order to create particles for a complex geometry simulation, we use boxes with frozen particles obtained from simulations of a desired fluid (without RBCs) with the periodic boundary conditions (PBC) in all directions. Afterwards, these boxes are replicated many times to fit in the entire complex geometry.

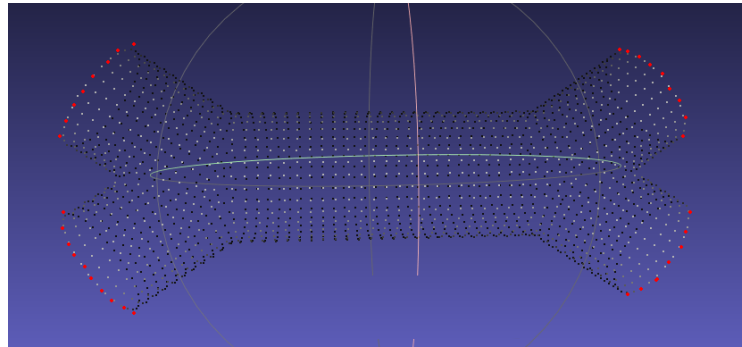


Figure B.1:: Cloud of points to create the surface for complex geometries is defined by a vector and the radius of the desired channel.

Then, we describe every channel of complex geometry with an orientation vector and two radii: one for inner surface which bounds the fluid particles, and outer surface which encloses the wall particles. Based on this definition we develop two clouds of points (Fig. B.1) which will be used later to construct

two surfaces to confine our geometry (Fig. B.2). RBCs might be included into the system during this step, and can be distributed along the vectors.

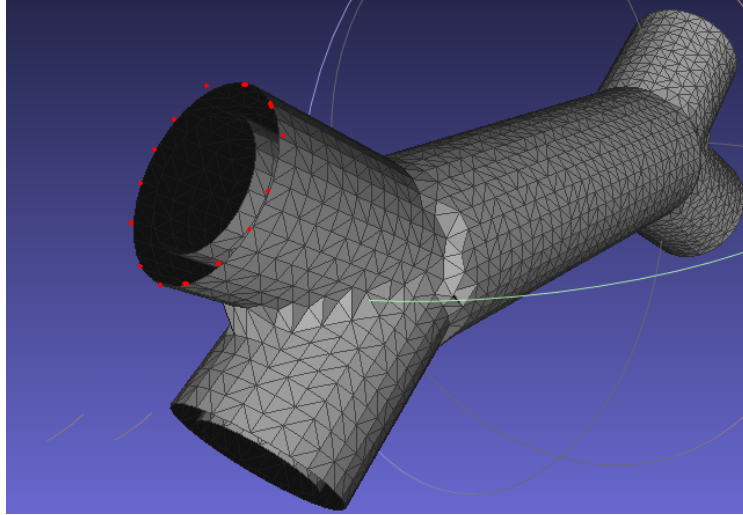


Figure B.2.: Triangulated surfaces for complex geometry simulation. Inner surface defines fluid particles, outer surface defines wall particles.

The next step, is to produce two surfaces, which will define the region for frozen particles using any software such as Meshlab or SolidWorks (Fig. B.2). Frozen particles which are found between inner and outer surfaces will be defined as the wall particles, and those inside the inner surface will be defined as the fluid particles. The developed code constructs a line which goes through a frozen particle in the direction of Z axis. If the line crosses the outer surface twice, then the particle is outside of the surface; if not - it is inside. The same method is used for the inner surface. Afterwards, the particles found only inside the inner surface are set to be fluid particles, and those which are not inside the inner surface, but inside the outer surface - the wall particles.

The same method can be used to determine the plasma fluid inside a RBC or outside, to simulate RBCs with a non-unity viscosity contrast.

B.2: Domain decomposition

Domain decomposition is a very useful instrument to simulate complex geometries on parallel computer architectures. A domain decomposition is used in order

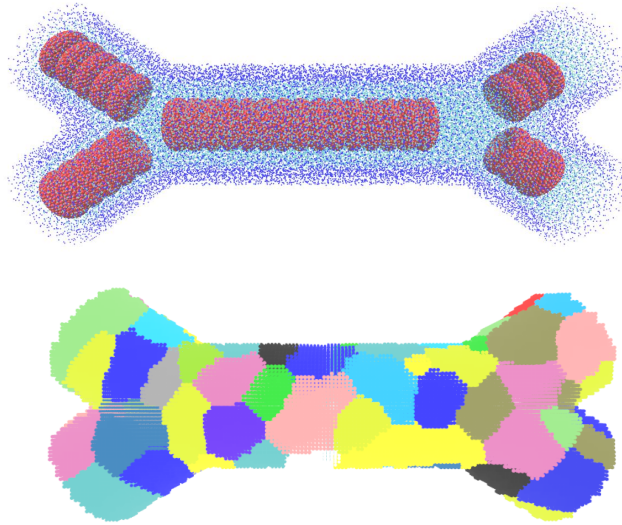


Figure B.3: Simulation setup (upper image) and its domain decomposition (lower image), there are several shades of color which look similar on the paper, but they represent different processors.

to save the computational time via eliminating void regions of the simulation domain from computation. Thus, only the regions with particles will be taken into computation by processors. We assign different spatial domains to different processors in such a way that they can optimally interact with each other. The connection optimization problem might be solved using, for example, METIS software from the University of Minnesota (Ref. <http://glaros.dtc.umn.edu/>).

An example of a domain decomposition is presented in figure B.3. Different colors refer to different processors (there are several shades of color which look similar on the paper, but they represent different processors).

Bibliography

- [1] M. Abkarian, M. Faivre, and A. Viallat. Swinging of red blood cells under shear flow. *Phys. Rev. Lett.*, 98:188302, 2007.
- [2] M. Abkarian, C. Lartigue, and A. Viallat. Tank treading and unbinding of deformable vesicles in shear flow: determination of the lift force. *Phys. Rev. Lett.*, 88:068103, 2002.
- [3] L.M. Adleman. Molecular computation of solutions to combinatorial problems. *Science*, 266(5187):1021–1024, 1994.
- [4] M. P. Allen and D. J. Tildesley. *Computer simulation of liquids*. Clarendon Press, New York, 1991.
- [5] V. V. Shuvaev S. Muro V. R. Muzykantov B.-S. Ding, T. Dziubla. Advanced drug delivery systems that target the vascular endothelium. *Molecular interventions*, 6(2):98, 2006.
- [6] G. Bossis and J.F. Brady. Self-diffusion of brownian particles in concentrated suspensions under shear. *The Journal of chemical physics*, 87(9):5437–5448, 1987.
- [7] I. Cantat and C. Misbah. Lift force and dynamical unbinding of adhering vesicles under shear flow. *Phys. Rev. Lett.*, 83:880–883, 1999.
- [8] N. F. Carnahan and K. E. Starling. Equation of state for nonattracting rigid spheres. *J. Chem. Phys.*, 51:635–636, 1969.
- [9] C.G. Caro. *The Mechanics of the Circulation*. Cambridge University Press, 2012.

Bibliography

- [10] J. A. Champion and S. Mitragotri. Role of target geometry in phagocytosis. *Proc. Natl. Acad. Sci. USA*, 103:4930–4934, 2006.
- [11] G. R. Cokelet and H. L. Goldsmith. Decreased hydrodynamic resistance in the two-phase flow of blood through small vertical tubes at low flow rates. *Circ. Res.*, 68:1–17, 1991.
- [12] The Emerging Risk Factors Collaboration. Diabetes mellitus, fasting blood glucose concentration, and risk of vascular disease: a collaborative meta-analysis of 102 prospective studies. *The Lancet*, 375(9733):2215 – 2222, 2010.
- [13] G. Couplier, B. Kaoui, T. Podgorski, and C. Misbah. Noninertial lateral migration of vesicles in bounded poiseuille flow. *Phys. Fluids*, 20:111702, 2008.
- [14] A. Gythiel D. S. Lemons. Paul langevin’s 1908 paper "on the theory of brownian motion"["sur la théorie du mouvement brownien," *cr acad. sci.(paris)* 146, 530–533 (1908)]. *American Journal of Physics*, 65(11):1079–1081, 1997.
- [15] E. R. Damiano. The effect of the endothelial-cell glycocalyx on the motion of red blood cells through capillaries. *Microvasc. Res.*, 55:77–91, 1998.
- [16] S. Dasgupta, T. Auth, and G. Gompper. Wrapping of ellipsoidal nanoparticles by fluid membranes. *Soft Matter*, 9:5473–5482, 2013.
- [17] P. Decuzzi, B. Godin, T. Tanaka, S.-Y. Lee, C. Chiappini, X. Liu, and M. Ferrari. Size and shape effects in the biodistribution of intravascularly injected particles. *J. Control. Release*, 141:320–327, 2010.
- [18] D. E. Discher, D. H. Boal, and S. K. Boey. Simulations of the erythrocyte cytoskeleton at large deformation. II. Micropipette aspiration. *Biophys. J.*, 75:1584–1597, 1998.
- [19] S. K. Doddi and P. Bagchi. Three-dimensional computational modeling of multiple deformable cells flowing in microvessels. *Phys. Rev. E*, 79:046318, 2009.

-
- [20] V. Doyeux, T. Podgorski, S. Peponas, M. Ismail, and G. Coupier. Spheres in the vicinity of a bifurcation: elucidating the zweifach-fung effect. *Journal of Fluid Mechanics*, 674:359–388, 5 2011.
- [21] P. Español and M. Revenga. Smoothed dissipative particle dynamics. *Phys. Rev. E*, 67:026705, 2003.
- [22] P. Español and P. Warren. Statistical mechanics of dissipative particle dynamics. *Europhys. Lett.*, 30:191–196, 1995.
- [23] E. A. Evans and R. Skalak. *Mechanics and thermodynamics of biomembranes*. CRC Press, Inc., Boca Raton, Florida, 1980.
- [24] M. Faivre. *Red blood cells and vesicles*. PhD thesis, Marseille, France, 2007.
- [25] D. A. Fedosov. *Multiscale modeling of blood flow and soft matter*. PhD thesis, Brown University, USA, 2010.
- [26] D. A. Fedosov, B. Caswell, and G. E. Karniadakis. A multiscale red blood cell model with accurate mechanics, rheology, and dynamics. *Biophys. J.*, 98:2215–2225, 2010.
- [27] D. A. Fedosov, B. Caswell, and G. E. Karniadakis. Systematic coarse-graining of spectrin-level red blood cell models. *Comput. Meth. Appl. Mech. Eng.*, 199:1937–1948, 2010.
- [28] D. A. Fedosov, B. Caswell, A. S. Popel, and G. E. Karniadakis. Blood flow and cell-free layer in microvessels. *Microcirculation*, 17:615–628, 2010.
- [29] D. A. Fedosov, M. Dao, G. E. Karniadakis, and S. Suresh. Computational biorheology of human blood flow in health and disease. *Ann. Biomed. Eng.*, 42:368–387, 2014.
- [30] D. A. Fedosov and G. Gompper. White blood cell margination in microcirculation. *Soft Matter*, 10:2961–2970, 2014.

Bibliography

- [31] D. A. Fedosov and G. E. Karniadakis. Triple-decker: Interfacing atomistic-mesoscopic-continuum flow regimes. *J. Comp. Phys.*, 228:1157–1171, 2009.
- [32] D. A. Fedosov, G. E. Karniadakis, and B. Caswell. Steady shear rheometry of dissipative particle dynamics models of polymer fluids in reverse Poiseuille flow. *J. Chem. Phys.*, 132:144103, 2010.
- [33] D. A. Fedosov, H. Noguchi, and G. Gompper. Multiscale modeling of blood flow: from single cells to blood rheology. *Biomech. Model. Mechanobiol.*, 13:239–258, 2014.
- [34] D. A. Fedosov, W. Pan, B. Caswell, G. Gompper, and G. E. Karniadakis. Predicting human blood viscosity in silico. *Proc. Natl. Acad. Sci. USA*, 108:11772–11777, 2011.
- [35] D. A. Fedosov, M. Peltomäki, and G. Gompper. Deformation and dynamics of red blood cells in flow through cylindrical microchannels. *Soft Matter*, 10:4258–4267, 2014.
- [36] T. M. Fischer. Shape memory of human red blood cells. *Biophys. J.*, 86:3304–3313, 2004.
- [37] R. Fåhræus. The suspension stability of the blood. *Physiol. Rev.*, 9:241–274, 1929.
- [38] R. Fåhræus and T. Lindqvist. The viscosity of the blood in narrow capillary tubes. *Am. J. Phys.*, 96:562–568, 1931.
- [39] M. Frank, D. Anderson, E. R. Weeks, and J. F. Morris. Particle migration in pressure-driven flow of a Brownian suspension. *J. Fluid Mech.*, 493:363–378, 2003.
- [40] Y. C. Fung. *Biomechanics: Mechanical properties of living tissues*. Springer-Verlag, New York, second edition, 1993.
- [41] D. A. Richards G. Pocock, C. D. Richards. *Human physiology*. Oxford university press, 2013.

-
- [42] F. Gentile, C. Chiappini, D. Fine, R. C. Bhavane, M. S. Peluccio, M. M.-C. Cheng, X. Liu, M. Ferrari, and P. Decuzzi. The effect of shape on the margination dynamics of non-neutrally buoyant particles in two-dimensional shear flows. *J. Biomech.*, 41:2312–2318, 2008.
- [43] H. L. Goldsmith, G. R. Cokelet, and P. Gaetgens. Robin Fahraeus: evolution of his concepts in cardiovascular physiology. *Am. J. Physiol.*, 257:H1005–H1015, 1989.
- [44] G. Gompper, T. Ihle, D. M. Kroll, and R. G. Winkler. Multi-particle collision dynamics: a particle-based mesoscale simulation approach to the hydrodynamics of complex fluids. *Adv. Polym. Sci.*, 221:1–87, 2009.
- [45] X. Grandchamp, G. Couplier, A. Srivastav, C. Minetti, and T. Podgorski. Lift and down-gradient shear-induced diffusion in red blood cell suspensions. *Phys. Rev. Lett.*, 110:108101, 2013.
- [46] W. Helfrich. Elastic properties of lipid bilayers: theory and possible experiments. *Z. Naturforschung C*, 28:693–703, 1973.
- [47] M. Herant, V. Heinrich, and M. Dembo. Mechanics of neutrophil phagocytosis: experiments and quantitative models. *J. Cell Sci.*, 119:1903–1913, 2006.
- [48] S. H. Holm, J. P. Beech, M. P. Barrett, and J. O. Tegenfeldt. Separation of parasites from human blood using deterministic lateral displacement. *Lab Chip*, 11:1326–1332, 2011.
- [49] P. J. Hoogerbrugge and J. M. V. A. Koelman. Simulating microscopic hydrodynamic phenomena with dissipative particle dynamics. *Europhys. Lett.*, 19:155–160, 1992.
- [50] N. E. Kim S. K. Larkin L. L. Peters J. Hartwig F. A. Kuypers V. M. Fowler J. D. Moyer, R. B. Nowak. Tropomodulin 1-null mice have a mild spherocytic elliptocytosis with appearance of tropomodulin 3 in red blood cells and disruption of the membrane skeleton. *Blood*, 116(14):2590–2599, 2010.

Bibliography

- [51] E. Kaliviotis S. Balabani J. M. Sherwood, D. Holmes. Spatial distributions of red blood cells significantly alter local haemodynamics. *PLoS ONE*, 9(6):e100473, 06 2014.
- [52] B. P. Griffith Z. J. Wu K. H. Fraser, M. E. Taskin. The use of computational fluid dynamics in the development of ventricular assist devices. *Medical engineering & physics*, 33(3):263–280, 2011.
- [53] H. Lei I. V. Pivkin G. E. Karniadakis K. Lykov, X. Li. Inflow/outflow boundary conditions for particle-based blood flow simulations: Application to arterial bifurcations and trees. *PLoS Comput Biol*, 11(8):e1004410, 08 2015.
- [54] V. Kantsler and V. Steinberg. Transition to tumbling and two regimes of tumbling motion of a vesicle in shear flow. *Phys. Rev. Lett.*, 96:036001, 2006.
- [55] S. R. Keller and R. Skalak. Motion of a tank-treading ellipsoidal particle in a shear flow. *J. Fluid Mech.*, 120:27–47, 1982.
- [56] A.N. Kolmogorov and S.V. Fomin. On analytical methods in the theory of probability. *Math. Ann*, 104:415–458, 1931.
- [57] A. Kumar and M. D. Graham. Mechanism of margination in confined flows of blood and other multicomponent suspensions. *Phys. Rev. Lett.*, 109:108102, 2012.
- [58] A. W. Lees and S. F. Edwards. The computer study of transport processes under extreme conditions. *Journal of Physics C: Solid State Physics*, 5(15):1921, 1972.
- [59] H. Lei, D. A. Fedosov, and G. E. Karniadakis. Time-dependent and outflow boundary conditions for dissipative particle dynamics. *J. Comp. Phys.*, 230:3765–3779, 2011.
- [60] D. Leighton and A. Acrivos. Measurement of shear-induced self-diffusion in concentrated suspensions of spheres. *J. Fluid Mech.*, 177:109–131, 1987.

-
- [61] H. H. Lipowsky, S. Usami, and S. Chien. In vivo measurements of "apparent viscosity" and microvessel hematocrit in the mesentery of the cat. *Microvasc. Res.*, 19:297–319, 1980.
- [62] D. C. Litzinger, A. M. J. Buiting, N. van Rooijen, and L. Huang. Effect of liposome size on the circulation time and intraorgan distribution of amphipathic poly(ethylene glycol)-containing liposomes. *Biochim. Biophys. Acta*, 1190:99–107, 1994.
- [63] Y. Liu and W. K. Liu. Rheology of red blood cell aggregation by computer simulation. *J. Comp. Phys.*, 220:139–154, 2006.
- [64] L. B. Lucy. A numerical approach to the testing the fission hypothesis. *Astronom. J.*, 82:1013–1024, 1977.
- [65] S. M. Deyev P. I. Nikitin M. P. Nikitin, V. O. Shipunova. Biocomputing based on particle disassembly. *Nature nanotechnology*, 9(9):716–722, 2014.
- [66] J. L. McWhirter, H. Noguchi, and G. Gompper. Flow-induced clustering and alignment of vesicles and red blood cells in microcapillaries. *Proc. Natl. Acad. Sci. USA*, 106:6039–6043, 2009.
- [67] J. L. McWhirter, H. Noguchi, and G. Gompper. Ordering and arrangement of deformed red blood cells in flow through microcapillaries. *New J. Phys.*, 14:085026, 2012.
- [68] S. Messlinger, B. Schmidt, H. Noguchi, and G. Gompper. Dynamical regimes and hydrodynamic lift of viscous vesicles under shear. *Phys. Rev. E*, 80:011901, 2009.
- [69] A. D. Michelson, editor. *Platelets*. Academic Press, Berlin, 3rd edition, 2012.
- [70] J. J. Monaghan. Smoothed particle hydrodynamics. *Annu. Rev. Astron. Astrophys.*, 30:543–574, 1992.
- [71] J. J. Monaghan. Smoothed particle hydrodynamics. *Rep. Prog. Phys.*, 68:1703–1759, 2005.

- [72] K. Müller, D. A. Fedosov, and G. Gompper. Margination of micro- and nano-particles in blood flow and its effect on drug delivery. *Sci. Rep.*, 4:4871, 2014.
- [73] K. Müller, D. A. Fedosov, and G. Gompper. Smoothed dissipative particle dynamics with angular momentum conservation. *J. Comp. Phys.*, 281:301–315, 2015.
- [74] S. Muro, C. Garnacho, J. A. Champion, J. Leferovich, C. Gajewski, E. H. Schuchman, S. Mitragotri, and V. R. Muzykantov. Control of endothelial targeting and intracellular delivery of therapeutic enzymes by modulating the size and shape of ICAM-1-targeted carriers. *Mol. Ther.*, 16:1450–1458, 2008.
- [75] K. Namdee, A. J. Thompson, P. Charoenphol, and O. Eniola-Adefeso. Margination propensity of vascular-targeted spheres from blood flow in a microfluidic model of human microvessels. *Langmuir*, 29:2530–2535, 2013.
- [76] H. Noguchi and G. Gompper. Dynamics of fluid vesicles in shear flow: effect of the membrane viscosity and thermal fluctuations. *Phys. Rev. E*, 72:011901, 2005.
- [77] H. Noguchi and G. Gompper. Shape transitions of fluid vesicles and red blood cells in capillary flows. *Proc. Natl. Acad. Sci. USA*, 102:14159–14164, 2005.
- [78] J. K. Armstrong O. K. Baskurt O. Yalcin, H. J. Meiselman. Effect of enhanced red blood cell aggregation on blood flow resistance in an isolated-perfused guinea pig heart preparation. *Biorheology*, 42(6):511, 2005.
- [79] P. Olla. The role of tank-treading motions in the transverse migration of a spheroidal vesicle in a shear flow. *Journal of Physics A: Mathematical and General*, 30(1):317, 1997.
- [80] W. Pan, B. Caswell, and G. E. Karniadakis. A low-dimensional model for the red blood cell. *Soft Matter*, 6:4366–4376, 2010.

-
- [81] A. S. Popel and P. C. Johnson. Microcirculation and hemorheology. *Annu. Rev. Fluid Mech.*, 37:43–69, 2005.
- [82] C. Pozrikidis. Numerical simulation of cell motion in tube flow. *Ann. Biomed. Eng.*, 33:165–178, 2005.
- [83] A. R. Pries, K. Ley, M. Claassen, and P. Gaehtgens. Red cell distribution at microvascular bifurcations. *Microvasc. Res.*, 38:81–101, 1989.
- [84] A. R. Pries, K. Ley, and P. Gaehtgens. Generalization of the Fahraeus principle for microvessel networks. *Am. J. Physiol.*, 251:H1324–H1332, 1986.
- [85] A. R. Pries, D. Neuhaus, and P. Gaehtgens. Blood viscosity in tube flow: dependence on diameter and hematocrit. *Am. J. Physiol.*, 263:H1770–H1778, 1992.
- [86] A. R. Pries and T. W. Secomb. Microvascular blood viscosity in vivo and the endothelial surface layer. *Am. J. Physiol.*, 289:H2657–H2664, 2005.
- [87] A. R. Pries and T. W. Secomb. Blood flow in microvascular networks. In R. F. Tuma, W. N. Duran, and K. Ley, editors, *Handbook of Physiology, The Cardiovascular System, Microcirculation*, pages 3–36. Academic Press, San Diego, 2008.
- [88] A. R. Pries, T. W. Secomb, and P. Gaehtgens. Biophysical aspects of blood flow in the microvasculature. *Cardiovasc. Res.*, 32:654–667, 1996.
- [89] A. R. Pries, T. W. Secomb, and P. Gaehtgens. The endothelial surface layer. *Pflügers Archiv*, 440:653–666, 2000.
- [90] A. R. Pries, T. W. Secomb, P. Gaehtgens, and J. F. Gross. Blood flow in microvascular networks. Experiments and simulation. *Circ. Res.*, 67:826–834, 1990.
- [91] A. R. Pries, T. W. Secomb, T. Gessner, M. B. Sperandio, J. F. Gross, and P. Gaehtgens. Resistance to blood flow in microvessels in vivo. *Circ. Res.*, 75:904–915, 1994.

Bibliography

- [92] A. R. Pries, T. W. Secomb, H. Jacobs, M. Sperandio, K. Osterloh, and P. Gaehtgens. Microvascular blood flow resistance: role of endothelial surface layer. *Am. J. Physiol.*, 273:H2272–H2279, 1997.
- [93] M. Debbah R. Couillet. *Random matrix methods for wireless communications*. Cambridge University Press, 2011.
- [94] M. D. Graham R. G. Henriquez-Rivera, K. Sinha. Margination regimes and drainage transition in confined multicomponent suspensions. *Physical review letters*, 114(18):188101, 2015.
- [95] D. A. Reasor Jr, J. R. Clausen, and C. K. Aidun. Coupling the lattice-Boltzmann and spectrin-link methods for the direct numerical simulation of cellular blood flow. *Int. J. Num. Meth. Fluids*, 68:767–781, 2012.
- [96] W. Reinke, P. Gaehtgens, and P. C. Johnson. Blood viscosity in small tubes: effect of shear rate, aggregation, and sedimentation. *Am. J. Physiol.*, 253:H540–H547, 1987.
- [97] M. Revenga, I. Zúñiga, and P. Español. Boundary conditions in dissipative particle dynamics. *Comput. Phys. Commun.*, 121-122:309–311, 1999.
- [98] W. R. Sanhai, J. H. Sakamoto, R. Canady, and M. Ferrari. Seven challenges for nanomedicine. *Nat. Nanotechnol.*, 3:242–244, 2008.
- [99] T. W. Secomb and R. Hsu. Resistance to blood flow in nonuniform capillaries. *Microcirculation*, 4:421–427, 1997.
- [100] T. W. Secomb and A. R. Pries. The microcirculation: physiology at the mesoscale. *J. Physiol.*, 589:1047–1052, 2011.
- [101] S. S. Shevkoplyas, T. Yoshida, L. L. Munn, and M. W. Bitensky. Biometric autoseparation of leukocytes from whole blood in a microfluidic device. *Anal. Chem.*, 77:933–937, 2005.
- [102] J. D. Slack, M. Kanke, G. H. Simmons, and P. P. DeLuca. Acute hemodynamic effects and blood pool kinetics of polystyrene microspheres following intravenous administration. *J. Pharm. Sci.*, 70:660–664, 1981.

-
- [103] S. Sukumaran and U. Seifert. Influence of shear flow on vesicles near a wall: a numerical study. *Phys. Rev. E*, 64:011916, 2001.
- [104] C. Misbah T. Biben, A. Farutin. Three-dimensional vesicles under shear flow: Numerical study of dynamics and phase diagram. *Phys. Rev. E*, 83:031921, Mar 2011.
- [105] G. J. Tangelder, H. C. Teirlinck, D. W. Slaaf, and R. S. Reneman. Distribution of blood platelets flowing in arterioles. *Am. J. Physiol.*, 248:H318–H323, 1985.
- [106] G. Tomaiuolo, V. Preziosi, M. Simeone, S. Guido, R. Ciancia, V. Martinelli, C. Rinaldi, and B. Rotoli. A methodology to study the deformability of red blood cells flowing in microcapillaries in vitro. *Ann Ist Super Sanita*, 43:186–192, 2007.
- [107] K. Tsukada, E. Sekizuka, C. Oshio, and H. Minamitani. Direct measurement of erythrocyte deformability in diabetes mellitus with a transparent microchannel capillary model and high-speed video camera system. *Microvasc. Res.*, 61:231–239, 2001.
- [108] H. Turlier, D. A. Fedosov, B. Audoly, T. Auth, N. S. Gov, C. Sykes, J.-F. Joanny, G. Gompper, and T. Betz. Equilibrium physics breakdown reveals the active nature of red blood cell flickering. *Nature Physics*, 2016.
- [109] H. Vink and B. R. Duling. Identification of distinct luminal domains for macromolecules, erythrocytes, and leukocytes within mammalian capillaries. *Circ. Res.*, 79:581–589, 1996.
- [110] H. M. Vollebregt, R. G. M. van der Sman, and R. M. Boom. Model for particle migration in bidisperse suspensions by use of effective temperature. *Faraday Discuss.*, 158:89–103, 2012.
- [111] S. Weinbaum, J. M. Tarbell, and E. R. Damiano. The structure and function of the endothelial glycocalyx layer. *Annu. Rev. Biomed. Eng.*, 9:121–167, 2007.

Bibliography

- [112] T. Werder, J. H. Walther, and P. Koumoutsakos. Hybrid atomistic-continuum method for the simulation of dense fluid flows. *J. Comp. Phys.*, 205:373–390, 2005.
- [113] W.-Y. Yen, B. Cai, M. Zeng, J. M. Tarbell, and B. M. Fu. Quantification of the endothelial surface glycocalyx on rat and mouse blood vessels. *Microvasc. Res.*, 83:337–346, 2012.
- [114] T. Young. Hydraulic investigations, subservient to an intended croonian lecture on the motion of the blood. *Philosophical Transactions of the Royal Society of London*, pages 164–186, 1808.

Acknowledgments

No man is an island, and here I would like to acknowledge all the people who helped me during my PhD studies at FZJ.

I am very grateful to my supervisor Professor Gerhard Gompper for giving me the opportunity of doing this work and support during my PhD studies. I am very thankful to him for providing me an almost unlimited supercomputer time at Juelich Supercomputer Center and possibilities to take part in many conferences.

I would like to thank my co-supervisor Dr. Dmitry Fedosov, for his great contribution to my knowledge of the field of blood simulations and help with everyday-problems. He was always open for new discussions and ideas, and helped to develop them.

I am grateful to Professor Michael Lässig for reading through my thesis, for useful feedback and suggestions.

I would like to thank all ICS-2 member for their support and advices they gave me during my study. I want to thank them for interesting scientific discussions and sharing their experience.

I would like to thank ForschungsZentrum Juelich and Cologne University stuff for their help with paperwork and their assistance.

Also, I want to acknowledge support by the International Helmholtz Research School of Biophysics and Soft Matter (IHRS BioSoft) for providing me opportunities to participate in many conferences, workshops, lectures and courses.

And of course, I would like express my deepest appreciation to my family: my parents, my sister, my brother, and certainly to my wife Victoria. Their supported me all these years giving me help every time I needed.

Erklärung zur Dissertation

Ich versichere, dass ich die von mir vorgelegte Dissertation selbständig angefertigt, die benutzten Quellen und Hilfsmittel vollständig angegeben und die Stellen der Arbeit - einschließlich Tabellen, Karten und Abbildungen - , die anderen Werken im Wortlaut oder dem Sinn nach entnommen sind, in jedem Einzelfall als Entlehnung kenntlich gemacht habe; dass diese Dissertation noch keiner anderen Fakultät oder Universität zur Prüfung vorgelegen hat; dass sie - abgesehen von unten abgegebenen Teilpublikationen - noch nicht veröffentlicht worden ist, sowie, dass ich eine solche Veröffentlichung vor Abschluss des Promotionsverfahrens nicht vornehmen werde.

Die Bestimmungen der Promotionsordnung sind mir bekannt. Die von mir vorgelegte Dissertation ist von Prof. Dr. Gerhard Gompper betreut worden.

Jülich, 17 Februar 2016

Dinar Katanov.

LEBENS LAUF

Vorname:	Dinar
Nachname:	Katanov
Geburtstag:	01.01.1987
Geburtsort:	Durtuly, Russland
Staatsbürgerschaft:	Russische Föderation
Oktober 2014 - September 2015	Promotionsstudent Universität zu Köln
Oktober 2012 -	Doktorand im Physik im Forschungszentrum Jülich
2009-2011	Master Student Angewandte Physik und Mathematik Moskauer Institut für Physik und Technologie
2005-2009	Bachelor Student Angewandte Physik und Mathematik Moskauer Institut für Physik und Technologie
2003-2005	Hochschule Durtuly Gymnasium #3